Extended Fluid-Dynamic Modelling for Numerical Solution of Micro-Scale Flows

by

James G. McDonald

A thesis submitted in conformity with the requirements
for the degree of Doctor of Philosophy
Graduate Department of Aerospace Engineering
University of Toronto

Copyright © 2011 by James G. McDonald

Abstract

Extended Fluid-Dynamic Modelling for Numerical Solution of Micro-Scale Flows

James G. M^{c}Donald
Doctor of Philosophy
Graduate Department of Aerospace Engineering
University of Toronto
2011

This study is concerned with the development of extended fluid-dynamic models for the prediction of micro-scale flows. When compared to classical fluid descriptions, such models must remain valid on scales where traditional techniques fail. Also, knowing that solution to these equations will be sought by numerical methods, the nature of the extended models must also be such that they are amenable to solution using computational techniques. Moment closures of kinetic theory offer the promise of satisfying both of these requirements. It is shown that the hyperbolic nature of moment equations imbue them with several numerical advantages including an extra order of spacial accuracy for a given reconstuction when compared to the Navier-Stokes equations and a reduced sensitivity to grid irregularities. In addition to this, the expanded set of parameters governed by the moment closures allow them to accurately model many strong non-equilibrium effects that are typical of micro-scale flows. Unfortunately, traditional moment models have suffered from various closure breakdowns, and robust models that offer a treatment for non-equilibrium viscous heat-conducting gas flows have been elusive. To address these issues, a regularized 10-moment closure is first proposed herein based on the maximum-entropy Gaussian moment closure. This mathematically well-behaved model avoids closure breakdown through a strictly hyperbolic treatment for viscous effects and an elliptic formulation that accounts for non-equilibrium thermal diffusion. Moreover, steps toward the development of fully hyperbolic moment closures for the prediction of non-equilibrium viscous gas flow are made via two novel approaches. A thorough study of each of the proposed techniques is made through numerical solution of many classical flow problems.

Acknowledgements

There are many people whom I wish to thank for their support of my research during the course of my Ph.D. studies. I am especially appreciative of the encouragement and support that my family has always been happy to offer. My wife, Lani Sommers, has always been there for me. She has been eager to help me in any way she could over the years, and has offered an abundance of both love and support. My parents have also been unwavering supporters of everything I have pursued during my life. They too have always been there with love, encouragement, and backing.

I feel lucky to have been able to undertake this research at the University of Toronto Institute for Aerospace Studies. During my time in this department I have been fortunate enough to work with a truly wonderful group of professors and colleagues. My adviser, Professor Clinton Groth, has opened the study of extended fluid mechanics and moment closures to me. He has shared his excitement for the field with me and given me every opportunity to participate in the research community. I am also thankful to the other members of my research committee, Professors James Gottlieb and David Zingg, first for their helpful questions, comments, and suggestions during my annual research review; but also for other interesting discussions I have had with them over the years which made their excitement for research so apparent. I would also like to gratefully acknowledge the efforts of Professors David Levermore and Ue-Li Pen for their involvement during my final oral examination.

My fellow students at the university have also added greatly to my experience during my work. I have really enjoyed my time in Toronto due mainly to the friendships I have formed while here. I am always happy to come to school in the morning because of the people I will see there. Though all of the colleagues I have had over the years have contributed to my overall experience, there are several people who have been especially important. My wife and I have been lucky to form strong friendships with Jason Hicken, Scott Northrup, Lucian Ivan and their families.

I am very grateful to the Natural Science and Engineering Research Council of Canada for their funding of my research through a Canadian Graduate Scholarship. I am also thankful for having received an Ontario Graduate Scholarship in Science and Technology. The support I received from both of these organizations was extremely helpful and much appreciated.

Computational resources for performing all of the calculations reported herein were provided by the SciNet High Performance Computing Consortium at the University of Toronto and Compute/Calcul Canada through funding from the Canada Foundation for Innovation (CFI) and the Province of Ontario, Canada.

James McDonald
October 1, 2010

Contents

List of Figures

List of Symbols

a_i	Acceleration vector
$A_{(i,j)}$	Area of cell (i, j)
c_i	Random-velocity vector
$\mathbf{C}^{(N)}$	Vector of N random velocity weights
E_{rot}	Rotational energy
f, $\mathcal{F}$	Veclocity distribution function
f_i	Flux potential
$\mathbf{F}_i^{(N)}$	Dyad of fluxes for N conserved moments
$\mathcal{G}$	Gaussian distribution function
h_i	Density potential
Kn	Flow Knudsen number
ℓ	Reference length
$\mathcal{M}$	Maxwell-Boltzmann distribution
m	Gas-particle mass
Ma	Flow Mach number
n	number density
n_i	Unit normal
P_{ij}	Anisotropic pressure tensor

Pr	Prandtl number
q_i	Heat-flux vector
Q_{ijk}	Generalized heat-flux tensor
R_{ijkl}	Tensor containing fourth-order random moments
Re	Flow Reynolds number
S	Entropy density
T	Temperature
t	Time
u_i	Bulk-velocity vector
$\mathbf{U}^{(N)}$	Vector of N conserved moments
v_i	Velocity vector
$\mathbf{V}^{(N)}$	Vector of N velocity weights
w_i	Velocity of cell face
$\mathbf{W}^{(N)}$	Vector of N primitive moments
x_i	Position vector
α	Accomodation coefficient
$\boldsymbol{\alpha}^{(N)}$	Vector of N closure coefficients
$\Delta[\ ]$	Collision operator's effect on a moment
κ	Boltzmann's constant
λ	Mean free path
ρ	Mass density
τ	Relaxation time
Θ_{ij}	Anisotropic temperature tensor

"... la viscosité proprement dite et considérée à l'état isolé, pourra nous paraître pratiquement nuisible..."

Jean-Paul Sartre – *L'Être et le Neant*

Chapter 1

Introduction

1.1 Non-Equilibrium Micro-Scale Flows and Moment Closures

Accurate and reliable numerical methods and mathematical descriptions are required for non-equilibrium micro-scale flows, such as those encountered in the complex conduits of micro-electromechanical systems (MEMS) and flows associated with chemical-vapour deposition (CVD) processes commonly encountered in the manufacturing of semiconductor devices [1, 2]. In many instances, Knudsen numbers, Kn, between 0.01 and 10 are possible for these flows, even at or above atmospheric pressure, and thermal non-equilibrium effects can significantly influence momentum and heat transfer. Nevertheless, computationally tractable mathematical descriptions of non-equilibrium or rarefied gaseous flows still remain somewhat elusive. Particle-simulation techniques, such as the direct-simulation Monte Carlo (DSMC) method of Bird [3], and techniques based on the direct discretization of the kinetic equation, such as the approach proposed by Mieussens [4], have been developed for the prediction of general non-equilibrium gaseous flows. However, for near-continuum through to transitional-regime flows, the computational costs incurred by these techniques are considerable. In particular, discrete-velocity methods become increasingly expensive for flows with a wide range of fluid velocities and DSMC methods suffer from similar prohibitive computational expense for flows with low Mach numbers. In these situations, computational expense and storage requirements have limited their widespread usage [5, 6].

Moment closures offer an approach for handling transition-regime flows ($0.01 \leq \mathrm{Kn} \leq 10$)

and seem particularly well-suited for the treatment of non-equilibrium micro-scale flows [7, 8, 9, 10]. For high-speed flows, such as those encountered in hypersonic re-entry to planetary atmospheres, the discontinuous nature (inviscid jumps) provided by moment closures for the predicted internal structure of shocks may be somewhat undesirable [9, 11, 12]; however, for subsonic and possibly even transonic micro-scale flows, moment closures may offer advantages over other approaches. The computational costs associated with the solution of the partial differential equations (PDEs) governing the time evolution of the moments representing macroscopic quantities of interest in three-dimensional physical space is anticipated to be considerably less than those associated with particle-simulation or direct-discretization solution methods, even for relatively high numbers of moments. Moreover, when seeking solutions of the closures via numerical methods, the purely hyperbolic nature of the resulting moment equations makes them particularly appealing. The hyperbolic moment equations involve only first-order derivatives[1] and are therefore very well suited to solution by the class of very successful Godunov-type finite-volume schemes which make use of adaptive mesh refinement (AMR) combined with treatments for embedded and moving boundaries and interfaces [13, 14, 15, 16, 17, 18]. For hyperbolic systems, schemes of this type are robust, insensitive to irregularities in the computational grids, provide accurate resolution of discontinuities, and permit the systematic application of physically realistic boundary conditions. When coupled with AMR, they permit treatment of complex and evolving flow geometries and the resolution of highly disparate length scales while optimizing the usage of computational resources. They also have narrow stencils, making them suitable for implementation on massively parallel computer architectures [14, 15, 16, 17, 18]. Also, the necessity to calculate only first derivatives means that, for a given stencil or reconstruction, numerical schemes for the solution of moment equations can achieve one order higher spacial accuracy as compared to the solution of traditional fluid-dynamic equations such as the Navier-Stokes equations.

Unfortunately, moment closures are not without their limitations. Although the original closure hierarchies due to Grad [7, 19, 20] result in moment equations that are hyperbolic for near-equilibrium flows, these PDEs can suffer from closure breakdown and loss of hyperbolicity, even for relatively small departures from equilibrium conditions, even for physically realizable sets of macroscopic moments. Closure breakdown in this

[1] This is in contrast to other transport equations that have a partially elliptic nature and require the evaluation of second- or even higher-order derivatives.

case refers specifically to the invalidity of the moment closures for initial value problems due to the loss of hyperbolicity. The term is also used herein more generally to refer to the failure or invalidity of closures for reasons ranging from loss of hyperbolicity to non-integrability or realizability of the distribution function. Moment realizability refers here to the existence of a positive semi-definite velocity distribution function corresponding to the set of predicted velocity moments.

More recently, Struchtrup and Torrilhon have proposed regularized variants of the Grad moment closure hierarchy based on a Chapman-Enskog expansion technique applied directly to the moment equations [10, 21, 22, 23]. Although the regularized closures have proved to be quite promising and result in smooth transitions for shocks (a desirable feature for high-speed applications, such as re-entry flows), the resulting transport equations for the moments are of mixed type (*i.e.*, the moment fluxes are functions of the velocity moments and their derivatives) and formal hyperbolicity of the closures is lost. As a consequence, the computational advantages of purely hyperbolic treatments discussed above are also lost and one is faced with dealing with the challenges associated with the discretization of higher-order derivatives of the solution on irregular meshes, for which there can be serious trade-offs between accuracy and positivity (related to the satisfaction of the maximum principal) of the spatial discretization operator [24, 25]. Both accurate and positive discretizations of the Laplacian operator can be difficult to achieve on computational meshes having large variations in the sizes of adjacent cells as can typically occur in AMR techniques. Additionally, the regularization process does not avoid the issues associated with closure breakdown or non-realizability of the predicted moments.

Alternative moment-closure techniques have been proposed based on the assumption that the approximate form for the distribution function corresponds to that of the maximum-entropy distribution [8, 9]. The maximum-entropy distribution is defined to be the distribution that maximizes the physical entropy subject to the constraint that it be consistent with a given finite set of velocity moments. Finite non-negative values for the approximate form of the distribution function can be assured through the judicious selection of closure moments. More importantly, moment closures obtained in this manner have many desirable mathematical properties including hyperbolicity, realizability of moments, and a definable entropy relation [8, 9]. Based on these ideas, Levermore [8] has proposed a hierarchy of maximum-entropy closures. The lowest-order members of this hierarchy are the Maxwellian and Gaussian closures, both of which yield strictly

hyperbolic moment equations and physically realizable moments. Preliminary numerical solutions of the Gaussian closure using Godunov-type finite-volume schemes have been considered by Brown *et al.* [11, 12] and McDonald and Groth [14, 26]. Numerical solution of these closures in a Discontinuous-Galerkin context has also been explored recently by Barth [27]. These early studies clearly illustrate some of the computational advantages of having a strictly hyperbolic and physically realizable treatment (further evidence will be provided herein). Unfortunately, high-order members of Levermore hierarchy (those closures based on super-quadratic velocity weights) do not remain definable for the full range of physically realizable moments. As shown by Junk [28, 29, 30, 31], the entropy maximization problem is not guaranteed to have a solution for all physically realizable velocity moments. This deleterious result is in fact true for any high-order maximum-entropy closures and is particularly devastating as local equilibrium solutions can be shown to lie on the boundary in moment space separating the valid region for the closure, in which the entropy maximization problem can be solved, from the invalid region, in which a solution to the entropy maximization problem cannot be found [29]. Obviously this situation is not tenable for practical computations of non-equilibrium gaseous flows and has prevented the wider application of maximum-entropy-based moment closures.

Recently, Schneider [30, 31] has proposed an approach to dealing with the realizability of maximum-entropy closures. In this approach, regions of non-realizability are handled by relaxing the equality constraint on some of the moment values. A maximum-entropy distribution function can then be found for a subset of the moments of interest. When Schneider's technique is followed, it can be shown that global hyperbolicity and realizability are recovered. Hauck *et al.* [31] have subsequently carried out a thorough mathematical analysis of this alternate approach to modifying maximum-entropy closures. It must be noted that although this technique deals with all regions where the maximum-entropy distribution function is mathematically not realizable, there remain regions arbitrarily close to equilibrium for which the associated closing fluxes become arbitrarily large. This means that issues still remain for any solution procedure which makes use of finite-precision arithmetic as numerical overflow can certainly occur.

Alternately, hyperbolic moment closures that are not based on a maximum-entropy concept have been recently proposed by Torrilhon [32]. These closures are based on a Pearson-IV distribution function. Work in this area remains preliminary; it remains to be seen if the resulting closures are truly globally hyperbolic and the quality of flow solutions produced by the resulting moment equations requires further study.

1.2 Wider Applicability of Moment-Closures

Although the focus here is micro-scale flows, moment closures offer the promise of much wider applicability. Any situation in which gases exist in a rarefied state or local non-equilibrium effects are present can in theory be handled effectively by moment closures. Though not considered in this work, it is possible to create moment closures for non-uniform multi-component mixtures of gases which can interact through particle collisions or other forces, such as electro-magnetism [20, 33, 34, 35]. Moment closures can therefore be used in magneto-electro-hydrodynamic applications such as plasma modelling, hypersonic flows in which ionization occurs, or space weather prediction.

Furthermore, moment-closure applicability is not limited to exotic flow situations. In the course of this work a 10-moment maximum-entropy closure that is mathematically well-behaved and remains globally hyperbolicis is reviewed. This closure can be used as a hyperbolic alternative to the Navier-Stokes equations when heat-transfer is not significant. The 10-moment model offers applicability in all regimes when the adiabatic Navier-Stokes equations are valid as well as an expanded treatment for local non-equilibrium effects by allowing for anisotropic pressures. Such a hyperbolic model offers several advantages over the Navier-Stokes equations and the solution of the resulting equations can be seen as being more natural when using several popular numerical techniques for the solution of conservation laws, such as Godunov-type finite-volume schemes or discontinuous-Galerkin schemes.

1.3 Objectives of the Current Study

The objective of this research is to assess the capabilities of current moment closures for the prediction of micro-scale flows and to consider and develop other novel moment methods so as to expand on this applicability. This work contains the first thorough exploration of flow predictions obtained using maximum-entropy moment closures for a wide range of flow situations. The range of applicability of such closures is assessed and some of their mathematical advantages are demonstrated. With a view of expanding on current moment methods, new sets of moment equation are developed with the aim of finding a method which provides a reliable technique for the treatment of non-equilibrium heat transfer in a moment closure setting. The predictive abilities of each new model is assessed through numerical solution of classical flow problems.

1.4 Scope of the Current Study

This study begins with a review of gaskinetic theory and moment closures. Maximum-entropy moment closures are introduced and some of their mathematical properties are reviewed. Particular attention is given to the Gaussian 10-moment closure, which is a lower-order member of a hierarchy of maximum-entropy closures presented by Levermore [8]. Though this moment closures has been known for some time, this work contains the first thorough assessment of its predictive capabilities for a wide class of canonical flow problems through a range of Knudsen numbers. Its suitability for many micro-scale applications is clearly demonstrated.

Following this demonstration of moment closures predictive capabilities, it is shown that such closures also have several mathematical advantages over other methods. It is shown that the first-order nature of moment equations makes them ideally suited to solution by upwind-based finite-volume schemes and that their numerical solutions are far less sensitive to grid irregularities that are typical of complex geometries or AMR schemes. This is done through their solution using an embedded-boundary method and comparison to similar solutions of the Navier-Stokes equations for classical problems.

The Gaussian closure is attractive as it offers a hyperbolic treatment of viscous gas flow, however it is deficient in that it does not offer any treatment for heat-transfer effects. An extension is therefore shown which adds a treatment for thermal diffusion. This extension is based on a regularization technique that is similar to the technique used by Struchtrup and Torrilhon [10, 21, 22, 23] in their regularization of the Grad closure hierarchy. It is shown that the addition of heat transfer greatly improves flow predictions for many micro-scale and rarefied flows. Unfortunately the nature of the regularization procedure leads to the inclusion of elliptic terms, thus eliminating one of the more attractive features of moment closures.

Finally, an investigation of higher-order members of the maximum-entropy hierarchy is presented. Although these higher-order moment closures offer a treatment for heat-transfer, they suffer from several issues, both practical and theoretical. Several novel solutions to these issues which allow for the use of higher-order maximum-entropy and near-maximum-entropy closures are investigated. The thesis concludes with a summary of achievements and a view to future research.

Chapter 2

Elements of Gaskinetic Theory

2.1 Perspective

In classical fluid mechanics, the microscopic structure of fluids is relatively unimportant. This is due to the fact that the molecular nature of fluids exists on scales which are much smaller than the dimensions that are traditionally of interest[1]. This large separation of scales leads to microscopic fluctuations that "average out" on scales which are much smaller than lengths of interest in many fluid-dynamic situations (macroscopic scales). The smallest scale structure of fluids does not need to be known to properly describe such situations. If the dimensions of molecular processes associated with a fluid becomes larger in comparison to problem length scales of interest, this averaging of particle behaviour may not be possible and the microscopic nature of the fluid becomes important for a description of the flow.

The length scales associated with the molecular effects of a gas can be characterized by defining the mean free path, λ, of fluid molecules. This is the average distance that gas molecules travel between inter-particle collisions. It can be used to classify the regime in which a flow exists through the definition of the flow Knudsen number,

$$\mathrm{Kn} = \frac{\lambda}{\ell}\,, \tag{2.1}$$

which is the ratio of the mean free path to a representative length for the situation, ℓ. This non-dimensional number can then be used to define several flow regimes which characterize the importance of molecular collisions in flow behaviour as follows:

[1]In this work, the term "molecule" will be used to describe multi-atomic molecules as well as free atoms or ions.

$$\begin{aligned} \mathrm{Kn} < 0.01 \quad & \text{continuum regime,} \\ 0.01 \leq \mathrm{Kn} < 10 \quad & \text{transition regime,} \\ 10 \leq \mathrm{Kn} \quad & \text{free-molecular regime.} \end{aligned}$$

For very low Knudsen numbers, typically $\mathrm{Kn} < 0.01$, the scales associated with molecular processes are much smaller than characteristic lengths of the situation and traditional fluid-mechanic techniques are valid; this is known as the continuum regime. When the Knudsen number becomes larger, the details of gas-particle dynamics become paramount in an understanding of the situation. In such free-molecular situations, traditional fluid-mechanics cannot be used to describe gas behaviour; a treatment of gas-particle behaviour is required. For transitional flows, traditional equations are invalid and particle based methods can be prohibitively expensive. This leaves a flow-regime gap for which the moment methods introduced in chapter 1 seem well suited.

2.2 Velocity Distribution Functions

Gaskinetic theory seeks to use classical mechanics and a statistical representation of gas-particle velocity distributions to model gas behaviour. This theory assumes that a gas is comprised of many discrete particles, however, rather than attempting to model the behaviour of each individual particle, probability density functions, $f(x_i, v_i, t)$, are used. These distribution functions exist in a six-dimensional phase space. For example, if a monatomic gas is in local thermodynamic equilibrium, it will have a velocity distribution defined by a single temperature and given by

$$f(x_i, v_i, t) = \left(\frac{\beta(x_i, t)}{\pi} \right)^{(\frac{3}{2})} e^{(-\beta(x_i,t) v_i^2)} \,. \tag{2.2}$$

This is known as a Maxwell-Boltzmann distribution, where v_i is the particle velocity and $\beta(x_i, t) = m \,/\, 2\, \kappa\, T(x_i, t)$. In this relation $\kappa = 1.38054 \times 10^{-23} J/K$ is Boltzmann's constant, m is the particle mass, and $T(x_i, t)$ is the local temperature of the fluid. It can be shown that a gas in any arbitrary situation will be driven towards this distribution function by inter-particle collisions and, once it reaches this state, particle collisions will no longer affect the distribution function [19], hence the name "thermodynamic equilibrium".

By integrating equation 2.2 as follows:

$$\int_{v_{x1}}^{v_{x2}} \mathrm{d}v_x \int_{v_{y1}}^{v_{y2}} \mathrm{d}v_y \int_{v_{z1}}^{v_{z2}} \mathrm{d}v_z f(x_i, v_i, t) \,, \tag{2.3}$$

the fraction of particles at a position, x_i, and time, t, whose velocities are contained within the cube in velocity space defined by $v_{x1} \leq v_x \leq v_{x2}$, $v_{y1} \leq v_y \leq v_{y2}$, and $v_{z1} \leq v_z \leq v_{z2}$ can be found. Often distribution functions are multiplied by the number density, $n(x_i, t)$, of particles; such phase-space functions will be denoted by capital calligraphic letters,

$$\mathcal{F}(x_i, v_i, t) = n(x_i, t) f(x_i, v_i, t)\,. \tag{2.4}$$

By doing this, integrals such as the one above reveal the actual number of particles whose velocities lie within a specified region of velocity space at a given point, x_i, and time, t.

In the general, non-equilibrium case, gases can deviate significantly from the Maxwell-Boltzmann distribution given above. For the remainder of this work, if a distribution function, $\mathcal{F}$, is the equilibrium Maxwell-Boltzmann distribution, it will be denoted by the symbol $\mathcal{M}$.

2.3 Moments of Distribution Functions

In order to determine the macroscopic properties of a gas defined by a particular distribution function, velocity moments must be taken. This involves multiplying the distribution function by an appropriate velocity-dependent weight, $M(v_i)$, and integrating over all velocity space. For example, the mass density, ρ, can be determined by taking the molecular mass, m, of the gas as the weighting function as follows:

$$\rho = \iiint_{\infty} m\mathcal{F}(x_i, v_i, t)\ \mathrm{d}^3 v_i = \langle m\mathcal{F} \rangle\ . \tag{2.5}$$

Here the compact notation $\langle M(v_i)\mathcal{F} \rangle$ is used to denote integration over all velocity space. If the velocity over which the integrations should be taken is not obvious, it will be denoted with a subscript, $\langle M(v_i)\mathcal{F} \rangle_{v_i}$, however, in most cases it will be clear.

Similarly, by taking a component of particle momentum as the weight, the average, or bulk, velocity of the gas in that direction can be found and is given by

$$u_i = \frac{\langle m v_i \mathcal{F} \rangle}{\langle m\mathcal{F} \rangle}\,. \tag{2.6}$$

This is referred to as a first-order velocity moment as the weight is a linear function of particle velocity.

Once the bulk velocity of the fluid is known, it is possible to separate the particle velocity, v_i into two components: the bulk velocity, u_i, and the random velocity, c_i, such

that $v_i = u_i + c_i$. Moments can also be taken using weights dependent on the random component of particle velocity, $M(c_i)$. For example, the second-order random-velocity moment can be defined as

$$P_{ij} = \langle mc_i c_j \mathcal{F} \rangle \ , \tag{2.7}$$

where P_{ij} is the generalized pressure tensor. Due to its inherent symmetry, this tensor has six distinct components. The fluid or deviatoric stress tensor, τ_{ij}, is related to the pressure tensor as follows: $\tau_{ij} = \delta_{ij} p - P_{ij}$, where $p = P_{ii}/3$ is the equilibrium isotropic pressure and $\tau_{kk} = 0$ for a monatomic gas.

Following this method, moments of arbitrarily high order can be taken, however traditional macroscopic properties tend to be equated to relatively low-order moments (third-order or less). As the order of a moment becomes higher, its physical significance becomes less and less obvious.

2.4 The Boltzmann Equation

The time evolution of the velocity distribution function of a gas is described by the Boltzmann equation [10, 19] given by

$$\frac{\partial \mathcal{F}}{\partial t} + v_i \frac{\partial \mathcal{F}}{\partial x_i} + a_i \frac{\partial \mathcal{F}}{\partial v_i} = \frac{\delta \mathcal{F}}{\delta t} \, . \tag{2.8}$$

Here a_i is the particle acceleration due to external forces such as gravity and is taken to be zero in the present work. The term on the right hand side of the equation, $\frac{\delta \mathcal{F}}{\delta t}$, is the collision term. This term represents the effects of intermolecular collisions on the distribution function.

Following the assumptions that only binary collisions of identical particles occur, that such collisions take place on a scale much smaller than the mean free path, that the distribution function can be assumed to be constant over this range, that a single collision does not appreciably change the distribution function, and that particle velocities are independent (this is often referred to as the assumption of molecular chaos); the collision integral can be shown to have the form

$$\frac{\delta \mathcal{F}}{\delta t} = \left\langle \int_0^{2\pi} \int_0^{\pi} (\mathcal{F}' \mathcal{F}^{1\prime} - \mathcal{F} \mathcal{F}^1) g \sigma \sin\chi \ \mathrm{d}\chi \ \mathrm{d}\epsilon \right\rangle_{v_i'} \, . \tag{2.9}$$

Here $\mathcal{F}$ and $\mathcal{F}^1$ are the local distribution function written in terms of two particles with velocities v_i and v_i^1 that are undergoing a collision and $\mathcal{F}'$ and $\mathcal{F}^{1\prime}$ are written in terms

of their velocities after the collision (v_i' and $v_i^{1\prime}$). The particles' relative speed prior to the collision is denoted as $g = |v_i - v_i^1|$, σ is the differential collision cross section, χ is the deflection angle, and ϵ is a solid angle integrated around a particle undergoing collisions. Details regarding the derivation of this integral expression are available in any standard kinetic-theory textbook [10, 19].

2.4.1 Simplified Collision Operators

Even for simple cases, the collision operator can be prohibitively complicated to evaluate for practical engineering applications. Simplified collision models are therefore often adopted. One common approximation is the BGK [36] or relaxation-time model, given by

$$\frac{\delta \mathcal{F}}{\delta t} = -\frac{\mathcal{F}(x_i, v_i, t)}{\tau_{\mathcal{F}}(x_i, t)} + \frac{\mathcal{M}(x_i, v_i, t)}{\tau_{\mathcal{M}}(x_i, t)}\,. \tag{2.10}$$

In this model, particles in non-equilibrium are removed and particles in equilibrium are added exponentially with characteristic times $\tau_{\mathcal{F}}$ and $\tau_{\mathcal{M}}$, respectively. For most situations, these times are taken to be equal, $\tau_{\mathcal{F}} = \tau_0 = \tau$. Making this assumption causes equation 2.10 to reduce to

$$\frac{\delta \mathcal{F}}{\delta t} = -\frac{\mathcal{F}(x_i, v_i, t) - \mathcal{M}(x_i, v_i, t)}{\tau(x_i, t)}\,. \tag{2.11}$$

It can easily be seen that when the non-equilibrium distribution, $\mathcal{F}$, becomes everywhere equal to the equilibrium solution, $\mathcal{M}$, the collision operator will vanish as required.

2.5 The Method of Moments

For most practical applications, the enormous amount of information obtained from the solution of the Boltzmann equation is unnecessary. Numerical schemes which solve the Boltzmann equation require a discretization of the physical spacial domain of the problem as well as a discretization of the infinite domain of velocity space (or at least a region that is large enough to capture all velocities of significance throughout the flow) with sufficient resolution to accurately represent the velocity distribution function of the gas particles for the entire flow domain. The computational expense of such a scheme can be prohibitive.

For many purposes, it is sufficient to obtain solutions for a specified set of macroscopic properties of a gas, as proposed in the original method of moments due to Grad [7]. It

is therefore necessary to derive equations which govern the evolution of a given set of velocity moments.

At this point, it is convenient to define notation to describe moments of interest for a given situation and their corresponding velocity-dependent weights. A column vector containing weights that are expressed as a function of the total particle velocity, v_i, will be represented by the symbol $\mathbf{V}^{(N)}$, where N is the number of entries in the vector. Similarly, a column vector containing weights that are expressed as a function of the random particle velocity, c_i, will be represented by the symbol $\mathbf{C}^{(N)}$. The resulting moment vectors will be defined as

$$\mathbf{U}^{(N)} = \left\langle m\mathbf{V}^{(N)}\mathcal{F} \right\rangle , \tag{2.12}$$

$$\mathbf{W}^{(N)} = \left\langle m\mathbf{C}^{(N)}\mathcal{F} \right\rangle . \tag{2.13}$$

Here, the moments contained in $\mathbf{U}^{(N)}$ will be referred to as the conserved moments, moments contained in $\mathbf{W}^{(N)}$ will be referred to as either the random or primitive moments. It must also be noted that the first-order moments in $\mathbf{W}^{(N)}$ are defined in a special way. This is because all first-order random-velocity moments of any distribution function are zero by definition. Therefore, the bulk velocity, as defined in equation 2.6, will be defined as the random moment in $\mathbf{W}^{(N)}$ which corresponds to a first-order random-velocity weights in $\mathbf{C}^{(N)}$.

2.5.1 Maxwell's Equation of Change

In order to determine the time evolution of the macroscopic quantity associated with a velocity weight, M, as defined earlier, moments of the Boltzmann equation can be taken and written as

$$\frac{\partial}{\partial t}\left\langle mM\mathcal{F}\right\rangle + \frac{\partial}{\partial x_i}\left\langle mv_iM\mathcal{F}\right\rangle + \frac{\partial}{\partial v_i}\left\langle ma_iM\mathcal{F}\right\rangle = \left\langle mM\frac{\delta\mathcal{F}}{\delta t}\right\rangle . \tag{2.14}$$

Again, the acceleration field, a_i, will be taken to be zero. By introducing the notation: $\Delta[M\mathcal{F}] = \left\langle mM\frac{\delta\mathcal{F}}{\delta t}\right\rangle$, equation 2.14 can be rewritten as

$$\frac{\partial}{\partial t}\left\langle mM\mathcal{F}\right\rangle + \frac{\partial}{\partial x_i}\left\langle mv_iM\mathcal{F}\right\rangle = \Delta[M\mathcal{F}] . \tag{2.15}$$

This is Maxwell's equation of change written in conservative form.

If a vector of velocity-dependent weights, $\mathbf{V}^{(N)}$, is used in place of an individual weight. The result will be a coupled set of N moment equations describing the evolution

of the corresponding conserved moments,

$$\frac{\partial}{\partial t}\left\langle m\mathbf{V}^{(N)}\mathcal{F}\right\rangle + \frac{\partial}{\partial x_i}\left\langle mv_i\mathbf{V}^{(N)}\mathcal{F}\right\rangle = \Delta[\mathbf{V}^{(N)}\mathcal{F}]\,, \tag{2.16}$$

or

$$\frac{\partial \mathbf{U}^{(N)}}{\partial t} + \frac{\partial}{\partial x_i}\left\langle mv_i\mathbf{V}^{(N)}\mathcal{F}\right\rangle = \Delta[\mathbf{V}^{(N)}\mathcal{F}]\,. \tag{2.17}$$

At this point it is also convenient to introduce the notation $\mathbf{F}_i^{(N)} = \left\langle mv_i\mathbf{V}^{(N)}\mathcal{F}\right\rangle$ for the flux diad corresponding to the conserved moment vector $\mathbf{U}^{(N)}$. Equation 2.17 can then be rewritten compactly as

$$\frac{\partial \mathbf{U}^{(N)}}{\partial t} + \frac{\partial \mathbf{F}_i^{(N)}}{\partial x_i} = \Delta[\mathbf{V}^{(N)}\mathcal{F}]\,. \tag{2.18}$$

2.5.2 Moments of the Collision Operator

The collision operator applied to the vector of velocity weights, $\mathbf{V}^{(N)}$, is given by

$$\begin{aligned}\Delta[\mathbf{V}^{(N)}\mathcal{F}] &= \left\langle m\mathbf{V}^{(N)}\left\langle\int_0^{2\pi}\int_0^{\pi}(\mathcal{F}'\mathcal{F}^{1\prime}-\mathcal{F}\mathcal{F}^{1})g\sigma\sin\chi\;\mathrm{d}\chi\;\mathrm{d}\epsilon\right\rangle_{v_i'}\right\rangle_{v_i}\\ &= \left\langle\left\langle\int_0^{2\pi}\int_0^{\pi}m\mathbf{V}^{(N)}(\mathcal{F}'\mathcal{F}^{1\prime}-\mathcal{F}\mathcal{F}^{1})g\sigma\sin\chi\;\mathrm{d}\chi\;\mathrm{d}\epsilon\right\rangle_{v_i'}\right\rangle_{v_i}\,. \end{aligned}\tag{2.19}$$

Due to the inherent symmetries of particle collisions with respect to the four velocities v_i, v_i^1, v_i', and $v_i^{1\prime}$; this collision integral can also be written as

$$\Delta[\mathbf{V}^{(N)}\mathcal{F}] = \left\langle\left\langle\int_0^{2\pi}\int_0^{\pi}m\mathbf{V}^{(N)1}(\mathcal{F}'\mathcal{F}^{1\prime}-\mathcal{F}\mathcal{F}^{1})g\sigma\sin\chi\;\mathrm{d}\chi\;\mathrm{d}\epsilon\right\rangle_{v_i'}\right\rangle_{v_i} \tag{2.20}$$

$$= \left\langle\left\langle\int_0^{2\pi}\int_0^{\pi}m\mathbf{V}^{(N)\prime}(\mathcal{F}\mathcal{F}^{1}-\mathcal{F}'\mathcal{F}^{1\prime})g\sigma\sin\chi\;\mathrm{d}\chi\;\mathrm{d}\epsilon\right\rangle_{v_i'}\right\rangle_{v_i} \tag{2.21}$$

$$= \left\langle\left\langle\int_0^{2\pi}\int_0^{\pi}m\mathbf{V}^{(N)1\prime}(\mathcal{F}\mathcal{F}^{1}-\mathcal{F}'\mathcal{F}^{1\prime})g\sigma\sin\chi\;\mathrm{d}\chi\;\mathrm{d}\epsilon\right\rangle_{v_i'}\right\rangle_{v_i}\,. \tag{2.22}$$

Averaging equations 2.19–2.22 produces a form for the collision integral that will prove useful and is given by

$$\Delta[\mathbf{V}^{(N)}\mathcal{F}] = \frac{m}{4}\left\langle\left\langle\int_0^{2\pi}\int_0^{\pi}\left(\mathbf{V}^{(N)}+\mathbf{V}^{(N)1}-\mathbf{V}^{(N)\prime}-\mathbf{V}^{(N)1\prime}\right)(\mathcal{F}'\mathcal{F}^{1\prime}-\mathcal{F}\mathcal{F}^{1})g\sigma\sin\chi\,\mathrm{d}\chi\,\mathrm{d}\epsilon\right\rangle_{v_i'}\right\rangle_{v_i}\,. \tag{2.23}$$

2.6 Entropy

A very interesting property predicted by the Boltzmann equation is found by inserting the velocity-dependent weight

$$M = -\frac{k}{m} \ln \frac{\mathcal{F}}{y} \tag{2.24}$$

into equation 2.18. By defining the variable $S = \left\langle -k \ln \frac{\mathcal{F}}{y} \mathcal{F} \right\rangle$, as well as its flux $\Psi_i = \left\langle -k v_i \ln \frac{\mathcal{F}}{y} \mathcal{F} \right\rangle$, and its production $\Phi = \Delta[-k \ln \frac{\mathcal{F}}{y} \mathcal{F}]$; the following transport equation is produced,

$$\frac{\partial S}{\partial t} + \frac{\partial \Psi_i}{\partial x_i} = \Phi \,. \tag{2.25}$$

In an isolated system, into which the flux of S is zero, the rate of change of S can be explored. In this case, equation 2.25 becomes

$$\frac{\partial S}{\partial t} = \Phi \,. \tag{2.26}$$

An examination of Φ, which results from the insertion of equation 2.24 into equation 2.23, shows that it cannot be negative, as

$$\Phi = \frac{k}{4} \left\langle \left\langle \int_0^{2\pi} \int_0^{\pi} \ln \frac{\mathcal{F}' \mathcal{F}^{1\prime}}{\mathcal{F} \mathcal{F}^1} (\mathcal{F}' \mathcal{F}^{1\prime} - \mathcal{F} \mathcal{F}^1) g \sigma \sin\chi \; \mathrm{d}\chi \; \mathrm{d}\epsilon \right\rangle_{v_i'} \right\rangle_{v_i} \geq 0 \,. \tag{2.27}$$

The non-negativity of this term can be seen as g and σ are always greater than zero, and $\sin\chi$ is non-negative for $0 \leq \chi \leq \pi$. Also, whenever $\ln \frac{\mathcal{F}' \mathcal{F}^{1\prime}}{\mathcal{F} \mathcal{F}^1}$ is negative, $(\mathcal{F}' \mathcal{F}^{1\prime} - \mathcal{F} \mathcal{F}^1)$ will be as well. In fact the variable, S, is an entropy density for the gas[2]. Boltzmann was the first to discover this relationship between macroscopic entropy and the distribution of gas-particle velocities. This mathematical result is known today as Boltzmann's H-theorem [37].

2.6.1 Entropy as Likelihood

One of the many triumphs of gaskinetic theory has been the insight that Boltzmann gave in relating the entropy of a gas to its velocity distribution. In fact, his celebrated H-theorem not only provides this relation in some abstract mathematical sense; it also provides a very physical sense of what entropy actually is and why it should increase.

[2]It should be noted that the entropy defined here is the thermodynamic entropy, which always grows with time. The mathematical entropy has the opposite sign and reduces with time.

A deeper insight into the meaning of entropy can be discovered, first by calculating the total entropy in a volume V [10, 38]:

$$H = \int_V S \ \mathrm{d}^3x_i = \int_V \int_\infty -k \ln \frac{\mathcal{F}}{y} \mathcal{F} \ \mathrm{d}^3v_i \ \mathrm{d}^3x_i \, . \tag{2.28}$$

Remembering the definition of the velocity distribution function, the number of particles in a particular differential volume at a phase-space location of $\hat{x}_i$ and $\hat{v}_i$ can be calculated as

$$N_{\hat{x}_i,\hat{v}_i} = \mathcal{F}(\hat{x}_i, \hat{v}_i) \ \mathrm{d}^3x_i \ \mathrm{d}^3v_i = \mathcal{F}(\hat{x}_i, \hat{v}_i)\mathrm{d}\hat{V} \, , \tag{2.29}$$

where $\mathrm{d}\hat{V}$ is the volume of the phase cell. The total entropy in the volume, V, as defined by equation 2.28, can then be written as a sum over all differential phase volumes as

$$H = -k \sum_{\hat{x}_i,\hat{v}_i} N_{\hat{x}_i,\hat{v}_i} \ln \frac{N_{\hat{x}_i,\hat{v}_i}}{y\mathrm{d}\hat{V}} \, , \tag{2.30}$$

where the sum is over all possible values of $\hat{x}_i$ and $\hat{v}_i$. By making use of the fact that the total number of particles, N, can be calculated as $N = \sum_{\hat{x}_i,\hat{v}_i} N_{\hat{x}_i,\hat{v}_i}$, the expression from H can be re-written as

$$H = -k \sum_{\hat{x}_i,\hat{v}_i} N_{\hat{x}_i,\hat{v}_i} \ln N_{\hat{x}_i,\hat{v}_i} \ + \ kN \ln \left(y\mathrm{d}\hat{V} \right) \, . \tag{2.31}$$

By twice making use of Sterling's approximation that $\ln N! \approx N \ln N - N$ (for large N), the following manipulations can be made:

$$\begin{aligned}
H &= -k \sum_{\hat{x}_i,\hat{v}_i} (\ln \ N_{\hat{x}_i,\hat{v}_i}! + N_{\hat{x}_i,\hat{v}_i}) \ + \ kN \ln \left(y\mathrm{d}\hat{V} \right) \\
&= -k \ \ln \left(\prod_{\hat{x}_i,\hat{v}_i} N_{\hat{x}_i,\hat{v}_i}! \right) \ - \ kN \ + \ kN \ln \left(y\mathrm{d}\hat{V} \right) \\
&= -k \ \ln \left(\prod_{\hat{x}_i,\hat{v}_i} N_{\hat{x}_i,\hat{v}_i}! \right) \ - \ k(N \ln N - \ln N!) \ + \ kN \ln \left(y\mathrm{d}\hat{V} \right) \\
&= k \ \ln \left(\frac{N!}{\prod_{\hat{x}_i,\hat{v}_i} N_{\hat{x}_i,\hat{v}_i}!} \right) \ + \ kN \ln \left(\frac{y\mathrm{d}\hat{V}}{N} \right) \, .
\end{aligned} \tag{2.32}$$

Finally, by choosing the constant $y = \frac{N}{\mathrm{d}\hat{V}}$, equation 2.32 simplifies to

$$H = k \ln W \tag{2.33}$$

where $W = \frac{N!}{\prod_{\hat{x}_i,\hat{v}_i} N_{\hat{x}_i,\hat{v}_i}!}$ is the number of ways to distribute N particles into the phase cells such that the cell at $\hat{x}_i$ and $\hat{v}_i$ contains $N_{\hat{x}_i,\hat{v}_i}$ particles; all such arrangements of

particles are described by the same velocity distribution function. Entropy can therefore be understood to represent the number of possible arrangements of gaseous particles in phase space corresponding to a given distribution function. If all particle arrangements occur with equal frequency, the velocity distribution functions with the highest entropy will therefore be the most likely. It therefore seems that if the distribution function of a gas is needed, but complete information is not known, it is best to chose the distribution function which has the maximum entropy of all those which satisfy the known properties of the gas as this is the most likely distribution for the gaseous particles.

2.7 Moment Closure

Returning to the subject of moment methods, it is clear that, in general, the moment equation shown above (equation 2.18) does not represent a closed system. It can be seen that the time evolution of the moments, $\mathbf{U}^{(N)} = \left\langle m\mathbf{V}^{(N)} \right\rangle$, is dependent on the divergence of the moment fluxes, $\mathbf{F}_i^{(N)} = \left\langle mv_i\mathbf{V}^{(N)}\mathcal{F} \right\rangle$. The latter includes moments of one higher order in terms of the velocity, v_i. Consequently, the time evolution of every moment is dependent on a moment of one higher order in v_i and, in general, an infinite number of moment equations is therefore required to fully describe the evolution of any given macroscopic flow quantity. Solution of this infinite system is entirely equivalent to solving equation 2.8 and no economy in computation has been achieved.

One technique for obtaining a closed system of moment equations (and reduced computational work) is to restrict the distribution function to some assumed form [7]. This form should be a function of a finite number of free coefficients or degrees of freedom. These coefficients can then be determined such that a chosen set of moments of the distribution function (those contained in the vector $\mathbf{U}^{(N)}$) are satisfied, as shown in equation 2.12 or 2.13. The number of chosen moments of interest must equal the number of degrees of freedom in the chosen distribution function. Restricting the distribution function in this manner will ensure that all moments not contained within $\mathbf{U}^{(N)}$ (including those in the flux diad, $\mathbf{F}_i^{(N)}$) become a function of the moments in the solution vector. A closed set of moment equations is therefore the result.

2.7.1 The Grad Closure Hierarchy

Perhaps the most well-known assumed or approximate form for the distribution function is the Grad-type polynomial series expansion, which has the form [7]

$$\mathcal{F}^{(N)} = \mathcal{M}\left[1 + \boldsymbol{\alpha}^{(N)\mathrm{T}}\mathbf{C}^{(N)}\right] , \tag{2.34}$$

where the expansion is performed about the equilibrium solution or Maxwellian distribution function, $\mathcal{M}$. The column vector, $\boldsymbol{\alpha}^{(N)}$, contains the N closure coefficients which are related to low-order moments as described above. The N random-velocity moments of interest satisfy

$$\mathbf{W}^{(N)} = \left\langle m\mathbf{C}^{(N)}\mathcal{F}^{(N)}\right\rangle . \tag{2.35}$$

In the original work of Grad [7], both 13- and 20-moment closures were considered with

$$N = 13\,, \quad \mathbf{C}^{(13)} = [1, c_i, c_ic_j, c_ic^2/2]^{\mathrm{T}}\,, \quad \mathbf{W}^{(13)} = [\rho, u_i, P_{ij}, q_i]^{\mathrm{T}}\,, \tag{2.36}$$

and

$$N = 20\,, \quad \mathbf{C}^{(20)} = [1, c_i, c_ic_j, c_ic_jc_k]^{\mathrm{T}}\,, \quad \mathbf{W}^{(20)} = [\rho, u_i, P_{ij}, Q_{ijk}]^{\mathrm{T}}\,, \tag{2.37}$$

respectively, where q_i and Q_{ijk} are the heat-flux vector and generalized heat-flux tensor. Extensions to many more moments have since been considered by other researchers [9, 10]. It is generally assumed that the inclusion of more moments in a closure leads to a greater possibility that the resulting approximate distribution can more closely approximate general non-equilibrium behaviour.

Although Grad-type expansions result in a closed set of locally hyperbolic transport equations for a finite set of velocity moments, the assumed distribution function can in many cases be non-physical. It is possible for equation 2.34 to yield negative probabilities for some values of the particle velocity; this is particularly true in the tails of the distribution function for large random velocities. More significantly, hyperbolicity of the resulting moment equations can be lost for physically realizable moment values which are relatively near equilibrium. As a consequence, the moment equations become ill-posed for initial-value problems, a property that is obviously highly undesirable and has limited the use of the polynomial-series-expansion technique.

Chapter 3

Maximum-Entropy Moment Closures

Rather than adopting a polynomial, series-expansion technique as originally proposed by Grad [7], an alternate technique for selecting an assumed form for the distribution function is to choose the function which maximizes the entropy while satisfying a given finite set of velocity moments [8, 9]. Following the logic of section 2.6.1, this is akin to selecting the most likely distribution function subject to the constraint that it yield a given finite set of moments. It will be shown that such a choice leads to moment closures which seem to have many very desirable mathematical properties.

3.1 Maximum-Entropy Distribution Function

The first step in the construction of the maximum-entropy moment method is the determination of the distribution function which maximizes the entropy while remaining consistent with the macroscopic moments in the solution vector. This procedure has been well studied, and is detailed in many previous studies and references [8, 9, 39].

It is easiest to derive the form of the entropy-maximizing distribution function by writing its associated velocity weight as

$$M = -\frac{k}{m}\left(\ln\frac{\mathcal{F}}{z} - 1\right). \tag{3.1}$$

This is identical to the function given in equation 2.24 with the relationship between the constants given as $y = ez$. The problem of maximizing the entropy while satisfying N

specified moments, $\mathbf{U}^{(N)}$, corresponding to velocity weights $\mathbf{V}^{(N)}$ is therefore

$$\max_{\mathcal{F}} \left\langle -k \left(\mathcal{F} \ln \frac{\mathcal{F}}{z} - \mathcal{F} \right) \right\rangle \tag{3.2}$$

subject to

$$\mathbf{U}^{(N)} = \left\langle \mathbf{V}^{(N)} \mathcal{F} \right\rangle . \tag{3.3}$$

This constrained maximization can be solved by using the technique of Lagrange multipliers. Introducing a vector of Lagrange multipliers, $\hat{\boldsymbol{\alpha}}^{(N)}$, the maximization problem becomes a search for the critical points of a new function, J, having the form

$$J = \left\langle -k \left(\mathcal{F} \ln \frac{\mathcal{F}}{z} - \mathcal{F} \right) \right\rangle - \hat{\boldsymbol{\alpha}}^{(N)\mathrm{T}} \left(\mathbf{U}^{(N)} - \left\langle \mathbf{V}^{(N)} \mathcal{F} \right\rangle \right) . \tag{3.4}$$

At a critical point, $\frac{\mathrm{d}J}{\mathrm{d}\mathcal{F}} = 0$, or

$$\begin{aligned} \frac{\mathrm{d}J}{\mathrm{d}\mathcal{F}} &= \left\langle -k \ln \frac{\mathcal{F}}{z} \right\rangle - \hat{\boldsymbol{\alpha}}^{(N)\mathrm{T}} \left\langle \mathbf{V}^{(N)} \right\rangle \\ &= \left\langle \ln \mathcal{F} - \boldsymbol{\alpha}^{(N)\mathrm{T}} \mathbf{V}^{(N)} \right\rangle = 0 , \end{aligned} \tag{3.5}$$

where here k and z have been absorbed into the Lagrange multipliers. It is clear that equation 3.5 is satisfied if the distribution function is of the form

$$\mathcal{F}^{(N)} = \exp \left(\boldsymbol{\alpha}^{(N)\mathrm{T}} \mathbf{V}^{(N)} \right) . \tag{3.6}$$

Also, the convexity of the entropy function ensures that this is the only solution [8, 9, 39] (*i.e.*, it is unique). It can now also be seen that the closure coefficients are the Lagrange multipliers from the constrained maximization problem.

The first researcher to apply the idea of entropy maximization to extended fluid dynamics was Dreyer [40]. It has also been explored extensively in the field of rational extended thermodynamics [9]. More recently, Levermore provided a hierarchy of moment closures based on the entropy-maximization principle [8] and showed that the hierarchy possesses many desirable mathematical properties. Levermore requires that the vector of velocity weights have three properties. Firstly, it must contain as a subset the weights which correspond to the Euler equations which govern flows in local equilibrium. That is to say, $\mathbf{V}^{(N)}$ must contain $[1, v_i, v_i v_i]^{\mathrm{T}}$ as a subset. Secondly, Levermore requires that the space of functions contained in $\mathbf{V}^{(N)}$ be invariant under translation and rotation; this ensures that the resulting moment equations will be Galilean invariant. Junk later demonstrated that this rule restricts the velocity weights to be polynomials [29]. The

third restriction that Levermore places on the velocity-weight vector is that the resulting distribution function, equation 3.6, must remain finite even as $v_i \to \infty$. If these three restrictions are satisfied, the resulting closure will posses a positive-valued distribution function, hyperbolic moment equations, realizability of predicted moments, and a definable entropy relation.

In three dimensions, the Levermore hierarchy includes 5-, 10-, 14-, 21-, 26-, and 35-moment closures with

$$N = 5\,, \quad \mathbf{C}^{(5)} = m[1, c_i, c^2/2]^{\mathrm{T}}\,, \quad \mathbf{W}^{(5)} = [\rho, u_i, p]^{\mathrm{T}}\,, \tag{3.7}$$

$$N = 10\,, \quad \mathbf{C}^{(10)} = m[1, c_i, c_i c_j]^{\mathrm{T}}\,, \quad \mathbf{W}^{(10)} = [\rho, u_i, P_{ij}]^{\mathrm{T}}\,, \tag{3.8}$$

$$N = 14\,, \quad \mathbf{C}^{(14)} = m[1, c_i, c_i c_j, c_i c^2/2, c^4/15]^{\mathrm{T}}\,, \quad \mathbf{W}^{(14)} = [\rho, u_i, P_{ij}, q_i, r]^{\mathrm{T}}\,, \tag{3.9}$$

$$N = 21\,, \quad \mathbf{C}^{(21)} = m[1, c_i, c_i c_j, c_i c_j c_k, c^4/15]^{\mathrm{T}}\,, \quad \mathbf{W}^{(21)} = [\rho, u_i, P_{ij}, Q_{ijk}, r]^{\mathrm{T}}\,, \tag{3.10}$$

$$N = 26\,, \quad \mathbf{C}^{(26)} = m[1, c_i, c_i c_j, c_i c_j c_k, c_i c_j c^2]^{\mathrm{T}}\,, \quad \mathbf{W}^{(26)} = [\rho, u_i, P_{ij}, Q_{ijk}, r_{ij}]^{\mathrm{T}}\,, \tag{3.11}$$

$$N = 35\,, \quad \mathbf{C}^{(35)} = m[1, c_i, c_i c_j, c_i c_j c_k, c_i c_j c_k c_l]^{\mathrm{T}}\,, \quad \mathbf{W}^{(35)} = [\rho, u_i, P_{ij}, Q_{ijk}, R_{ijkl}]^{\mathrm{T}}\,, \tag{3.12}$$

where $R_{ijkl} = m < c_i c_j c_k c_l \mathcal{F} >$ is the generalized fourth-order velocity moment tensor, $r_{ij} = R_{ijkk}$, and $r = R_{iikk}/15$. Unlike the series expansions of Grad, which can be viewed as perturbative expansions about the Maxwellian, the exponential form for the distribution function of maximum-entropy moment closures is non-perturbative and strictly positive valued while remaining finite even as $v_i \to \infty$ through the appropriate selection of the vector of velocity weights, $\mathbf{V}^{(N)}$ or $\mathbf{C}^{(N)}$.

Provided that the maximum-entropy distribution of equation 3.6 is definable, Levermore [8] has demonstrated the hyperbolicity of the resulting moment equations. By defining the density and flux potentials, $h(\boldsymbol{\alpha}^{(N)})$ and $f_i(\boldsymbol{\alpha}^{(N)})$, given by

$$h(\boldsymbol{\alpha}^{(N)}) = \left\langle e^{\boldsymbol{\alpha}^{(N)\mathrm{T}} \mathbf{V}^{(N)}} \right\rangle\,, \quad f_i(\boldsymbol{\alpha}^{(N)}) = \left\langle v_i e^{\boldsymbol{\alpha}^{(N)\mathrm{T}} \mathbf{V}^{(N)}} \right\rangle\,, \tag{3.13}$$

the closure moments and moment fluxes can be expressed simply as

$$h_{,\boldsymbol{\alpha}^{(N)}} = \frac{\partial h}{\partial \boldsymbol{\alpha}^{(N)}} = < \mathbf{V}^{(N)} e^{\boldsymbol{\alpha}^{(N)\mathrm{T}} \mathbf{V}^{(N)}} > , \quad f_{i,\boldsymbol{\alpha}^{(N)}} = \frac{\partial f_i}{\partial \boldsymbol{\alpha}^{(N)}} = < v_i \mathbf{V}^{(N)} e^{\boldsymbol{\alpha}^{(N)\mathrm{T}} \mathbf{V}^{(N)}} > \quad (3.14)$$

and the moment equations of equation 2.18 can then be written as

$$\frac{\partial}{\partial t} \left(h_{,\boldsymbol{\alpha}^{(N)}} \right) + \nabla_i \cdot f_{i,\boldsymbol{\alpha}^{(N)}} = < \mathbf{V}^{(N)} \frac{\delta \mathcal{F}}{\delta t} > = \mathbf{R}(\boldsymbol{\alpha}^{(N)}) \,, \quad (3.15)$$

where $\mathbf{R}(\boldsymbol{\alpha}^{(N)}) = < \mathbf{V}^{(N)} \delta \mathcal{F} / \delta t >$ is the source term associated with collisional processes. The terms $h_{,\boldsymbol{\alpha}^{(N)}}$ and $f_{i,\boldsymbol{\alpha}^{(N)}}$ can be differentiated again to give

$$h_{,\boldsymbol{\alpha}^{(N)}\boldsymbol{\alpha}^{(N)}} = < \mathbf{V}^{(N)} \left[\mathbf{V}^{(N)} \right]^{\mathrm{T}} e^{\boldsymbol{\alpha}^{(N)\mathrm{T}} \mathbf{V}^{(N)}} > , \quad (3.16)$$

and

$$f_{i,\boldsymbol{\alpha}^{(N)}\boldsymbol{\alpha}^{(N)}} = < v_i \ \mathbf{V}^{(N)} \left[\mathbf{V}^{(N)} \right]^{\mathrm{T}} e^{\boldsymbol{\alpha}^{(N)\mathrm{T}} \mathbf{V}^{(N)}} > \ . \quad (3.17)$$

The moment equations above can then be re-expressed as

$$h_{,\boldsymbol{\alpha}^{(N)}\boldsymbol{\alpha}^{(N)}} \frac{\partial \boldsymbol{\alpha}^{(N)}}{\partial t} + f_{i,\boldsymbol{\alpha}^{(N)}\boldsymbol{\alpha}^{(N)}} \cdot \nabla_i \boldsymbol{\alpha}^{(N)} = \mathbf{R}(\boldsymbol{\alpha}^{(N)}) \,. \quad (3.18)$$

Equation 3.18 describes the time evolution and transport of the closure coefficients, $\boldsymbol{\alpha}^{(N)}$, for the maximum-entropy distribution. Hyperbolicity of this system is assured by the symmetry of $f_{i,\boldsymbol{\alpha}^{(N)}\boldsymbol{\alpha}^{(N)}}$ and symmetric positive definiteness of $h_{,\boldsymbol{\alpha}^{(N)}\boldsymbol{\alpha}^{(N)}}$. Note that for any weighting coefficients, $\mathbf{w}$,

$$\mathbf{w}^{\mathrm{T}} h_{,\boldsymbol{\alpha}^{(N)}\boldsymbol{\alpha}^{(N)}} \mathbf{w} \ = \ \left\langle \mathbf{w}^{\mathrm{T}} \mathbf{V}^{(N)} \left[\mathbf{V}^{(N)} \right]^{\mathrm{T}} \mathbf{w} \ e^{\boldsymbol{\alpha}^{(N)\mathrm{T}} \mathbf{V}^{(N)}} \right\rangle \ \geq \ 0 \quad (3.19)$$

and hence $h_{,\boldsymbol{\alpha}^{(N)}\boldsymbol{\alpha}^{(N)}}$ is both symmetric and positive definite. The transport equations of equation 3.18 are in the form of a Godunov symmetric hyperbolic system [41] and this form can be shown to be equivalent to the classical Friedrichs-Lax form for hyperbolic systems [8, 42].

As first noted by Godunov [41], symmetric hyperbolic systems of the form given in equation 3.18 can be shown to satisfy an additional scalar entropy balance or dissipation law. Multiplication of equation 3.18 by $\boldsymbol{\alpha}^{(N)\mathrm{T}}$ and subsequent manipulation leads to

$$\frac{\partial}{\partial t} \left(\boldsymbol{\alpha}^{(N)\mathrm{T}} h_{,\boldsymbol{\alpha}^{(N)}} - h \right) + \nabla_i \cdot \left(\boldsymbol{\alpha}^{(N)\mathrm{T}} f_{i,\boldsymbol{\alpha}^{(N)}} - f_i \right) = \boldsymbol{\alpha}^{(N)\mathrm{T}} \mathbf{R}(\boldsymbol{\alpha}^{(N)}) \,. \quad (3.20)$$

Defining the entropy function, $s(\mathbf{U}^{(N)})$, to be Legendre transform of the density potential, $h(\boldsymbol{\alpha}^{(N)})$, given by

$$s(\mathbf{U}^{(N)}) + h(\boldsymbol{\alpha}^{(N)}) = \boldsymbol{\alpha}^{(N)\mathrm{T}} \mathbf{U}^{(N)} = \boldsymbol{\alpha}^{(N)\mathrm{T}} h_{,\boldsymbol{\alpha}^{(N)}} \,, \quad (3.21)$$

and the entropy flux to be Legendre transform of flux potential, $f_i(\boldsymbol{\alpha}^{(N)})$, such that

$$j_i(\mathbf{U}^{(N)}) + f_i(\boldsymbol{\alpha}^{(N)}) = \boldsymbol{\alpha}^{(N)\mathrm{T}} f_{i,\boldsymbol{\alpha}^{(N)}} \,, \tag{3.22}$$

then a dissipative entropy balance equation for $s(\mathbf{U}^{(N)})$ can be obtained from equation 3.20 and written as

$$\frac{\partial s}{\partial t} + \nabla_i \cdot j_i = \boldsymbol{\alpha}^{(N)\mathrm{T}} \mathbf{R}(\boldsymbol{\alpha}^{(N)}) = s_{,\mathbf{U}}^{\mathrm{T}} \mathbf{R}(s_{,\mathbf{U}}) \,, \tag{3.23}$$

where $s_{,\mathbf{U}} = \partial s / \partial \mathbf{U} = \boldsymbol{\alpha}^{(N)}$. In fact, making use to the form of the distribution function given in equation 3.6, equation 3.21 can be rewritten as

$$\begin{aligned} s(\mathbf{U}^{(N)}) &= \boldsymbol{\alpha}^{(N)\mathrm{T}} \mathbf{U}^{(N)} - h(\boldsymbol{\alpha}^{(N)}) \\ &= \left\langle m \boldsymbol{\alpha}^{(N)\mathrm{T}} \mathbf{V}^{(N)} \mathcal{F} \right\rangle - \langle m \mathcal{F} \rangle \\ &= \langle m \mathcal{F} \ln \mathcal{F} \rangle - \langle m \mathcal{F} \rangle \,. \end{aligned} \tag{3.24}$$

The relationship between this entropy and the entropy that is obtained by taking the velocity moment of the distribution function with the weight given in equation 3.1 obviously differ only by the constant $-k/m$ and a possible offset due to the parameter z in equation 3.1.

3.2 Determination of Closure Coefficients

The proof of hyperbolicity and the definition of a dissipative entropy given above are rather elegant and establish a great deal of promise for maximum-entropy moment closures. Nevertheless, the results are predicated on the existence of a maximum-entropy distribution of the form given in equation 3.6, for all physically realizable moments. The distribution function of equation 3.6 is the form that maximizes the physical entropy of the system for a given finite set of N moments, $\mathbf{U}^{(N)}$. This maximization process is equivalent to the minimization of the closure entropy, $s(\mathbf{U}^{(N)})$, defined in equation 3.21 above and often termed the mathematical entropy. Although the maximum-entropy closures could be equally referred to as "minimum-entropy" closures, as they formally correspond to the distribution function having the minimum mathematical entropy for a given set of moments, the more commonly used term "maximum-entropy" is applied herein in reference to the closures' maximization of physical entropy.

Given the values of the moments, $\mathbf{U}^{(N)}$, the entropy, $s(\mathbf{U}^{(N)})$, and closure coefficients, $\boldsymbol{\alpha}^{(N)}$, can be determined via the solution of the minimization problem given by

$$s(\mathbf{U}^{(N)}) = -\min_{\boldsymbol{\alpha}^{(N)}} \left[h(\boldsymbol{\alpha}^{(N)}) - \boldsymbol{\alpha}^{(N)\mathrm{T}} \mathbf{U}^{(N)} \right] . \tag{3.25}$$

When $h(\boldsymbol{\alpha}^{(N)})$ is differentiable, the solution of this minimization problem satisfies

$$\frac{\partial}{\partial \boldsymbol{\alpha}^{(N)}} \left[h(\boldsymbol{\alpha}^{(N)}) - \boldsymbol{\alpha}^{N\mathrm{T}} \mathbf{U}^{(N)} \right] = 0 \tag{3.26}$$

yielding

$$\mathbf{U}^{(N)} = h_{,\boldsymbol{\alpha}^{(N)}} = < \mathbf{V}^{(N)} e^{\boldsymbol{\alpha}^{(N)\mathrm{T}} \mathbf{V}^{(N)}} > . \tag{3.27}$$

The minimization problem above can be used to define a numerical approach for relating $\boldsymbol{\alpha}^{(N)}$ and $\mathbf{U}^{(N)}$ in situations for which explicit analytical expressions relating the coefficients to the predicted moments are not available.

The $N=5$ and $N=10$ lower-order closures of the Levermore hierarchy correspond to the Maxwellian and Gaussian closures. In these cases, closed-form analytical expressions relating the closure coefficients, $\boldsymbol{\alpha}^{(N)}$, to the predicted moments, $\mathbf{U}^{(N)}$, can be found and maximum-entropy distributions can be defined for the full range of physically realizable moments. Strict hyperbolicity of the moment equations is also assured for all realizable moments. For the Maxwellian model, the approximate distribution function is equal to the equilibrium of Maxwellian distribution function, $\mathcal{M}$, defined in equation 2.2 of chapter 2 above (*i.e.*, $\mathcal{F}^{(5)} = \mathcal{M}$) and, for the Gaussian model, the distribution function takes the form

$$\mathcal{F}^{(10)} = \mathcal{G} = \frac{\rho}{m(2\pi)^{3/2}(\det \Theta_{ij})^{1/2}} e^{\left(-\frac{1}{2}\Theta_{ij}^{-1} c_i c_j\right)} , \tag{3.28}$$

where $\Theta_{ij} = P_{ij}/\rho$ is an anisotropic "temperature" tensor. This non-equilibrium distribution possesses a Gaussian-like distribution in each of the principal strain axes. Physically, it corresponds to a non-equilibrium condition with a different temperature in each direction.

One potential stumbling block to practical application arises for all closures in the Levermore hierarchy beyond the Maxwellian and Gaussian systems: a numerical approach is required to relate moments and coefficients of the closure as explicit analytical expressions are not achievable. This can significantly increase the computational costs of carrying out a computation using the high-order maximum-entropy moment closures. However, a much more severe problem also appears for all closures beyond the Maxwellian and Gaussian systems. As stated above, all of the desirable mathematical properties of

the maximum-entropy closures assume that a maximum-entropy distribution function for the selected set of velocity moments always exists; this is not the case. Junk has shown that for any moment system based on moments which correspond to super-quadratic polynomial weight functions there are physically realizable combinations of the macroscopic moments for which a maximum-entropy distribution function is not valid and cannot be found [28, 29, 30, 31]. Moreover, moment states describing local thermodynamic equilibrium always lie on the boundaries separating regions in moment space in which a maximum-entropy distribution function exists and is definable and those regions for which the maximum-entropy distribution cannot be found [29]. The latter correspond to regions in which $h(\boldsymbol{\alpha}^{(N)})$ is no longer differentiable and therefore the solution of the entropy minimization problem given by equation 3.26 does not exist. For this reason, there are near-equilibrium regions in moment space for which the higher-order members of the Levermore maximum-entropy closures will become ill-posed or undefined. This is not a desirable feature for practical computations of non-equilibrium flows and it has prevented the wider application of the maximum-entropy closures from the Levermore hierarchy.

Chapter 4

The Gaussian Moment Closure

In spite of the evident limitations of the higher-order members of Levermore's maximum-entropy hierarchy discussed in chapter 3, the lowest-order non-equilibrium solution, the Gaussian closure, is a physically realizable and hyperbolic moment closure. The Gaussian distribution appears to have been first derived in early work by Maxwell [43] and then re-discovered in subsequent but independent research by both Schlüter [44, 45] and Holway [46, 47, 48, 49]. The potential of this type of closure for efficiently and accurately predicting both continuum and non-equilibrium flows is now demonstrated by considering the application of the Gaussian closure to a number of canonical flow problems. In what follows, an extension of the Gaussian closure for diatomic gases is first described and then numerical results are given for a number of example problems including shock structure, Couette flow, flat-plate boundary layer flow, flow past a circular cylinder, and flow past a NACA0012 micro airfoil.

4.1 Gaussian Closure for Monatomic Gases

The moment equations corresponding to the Gaussian closure can be obtained by using the weights $V^{(10)} = \{1, v_i, v_i v_j\}$ in the entropy maximization process described above. When the resulting distribution function, denoted by $\mathcal{G}$ and given in equation 3.28, is used in Maxwell's equation of change, equation 2.18, the result is a set of ten partial-differential equations describing the transport of the macroscopic quantities ρ, u_i, and P_{ij} which may be expressed as

$$\frac{\partial \rho}{\partial t} + \frac{\partial}{\partial x_k}\left(\rho u_k\right) = 0\,, \tag{4.1}$$

$$\frac{\partial}{\partial t}(\rho u_i) + \frac{\partial}{\partial x_k}(\rho u_i u_k + P_{ik}) = 0\,, \tag{4.2}$$

$$\frac{\partial}{\partial t}\left(P_{ij} + \rho u_i u_j\right) + \frac{\partial}{\partial x_k}\left(\rho u_i u_j u_k + u_i P_{jk} + u_j P_{ik} + u_k P_{ij}\right) = \Delta[v_i v_j \mathcal{F}] \tag{4.3}$$

Note that by construction the third-order random-velocity moments of the Gaussian are zero, $< mc_i c_j c_k \mathcal{G} >= 0$, such that the heat flux vector, $q_i = \frac{1}{2} < mc_i c_j c_j \mathcal{G} >$ also vanishes. This points to a significant limitation of the Gaussian closure: its inability to account for the effects of thermal diffusion (*i.e.*, the transport of translational particle energy by the random particle motion). Note also that when the solution reaches equilibrium and $\mathcal{G} = \mathcal{M}$, the Gaussian moment equations reduce to the Euler equations of equilibrium gas dynamics. Solution of equations 4.1–4.3, subject to appropriate initial and boundary data, provides a complete description of the Gaussian velocity distribution function throughout the flow field of interest.

4.2 An Extension for Diatomic Gases

The above set of moment equations, equations 4.1–4.3, was derived for a monatomic gas with three translational degrees of freedom and no internal (rotational or vibrational) degrees of freedom. This closure is therefore not immediately applicable to diatomic gases. A modification must be made to account for energy that can be present in the extra internal degrees of freedom for a diatomic gas. This can be done following the extension developed previously in an earlier study by Hittinger [50].

Under normal pressures and temperatures, vibrational degrees of freedom are usually not excited. It is therefore sufficient to simply model the translational and rotational degrees of freedom present in diatomic molecules. The energy associated with the translation of the center of mass of a diatomic molecule will be equal to that of a monatomic molecule of equal weight. Therefore, the only addition required to the 10-moment model is a treatment for the energy present in the rotation of the molecules. To do this, a "dumbbell" model of a diatomic molecule will be adopted. This model molecule is free to rotate about three different axes. Rotation about the axis that is co-axial to the line that connects the two atoms is assumed to contain no energy, as the moment of inertia about this axis is negligible.

Rotational energy can be present in the form of rotation about the remaining two axes. This energy will be prescribed using

$$\epsilon_{rotation} = \frac{1}{2} I_\zeta \omega_\zeta^2 + \frac{1}{2} I_\eta \omega_\eta^2 \,, \tag{4.4}$$

where ζ and η are the two axes about which rotational energy may be present. The parameters I_ζ and I_η are the particle's moment of inertia about these two axes.

The distance of each atom from the molecule's center of mass is given by

$$d_1 = \frac{m_2}{m_1 + m_2} d \qquad \text{and} \qquad d_2 = \frac{m_1}{m_1 + m_2} d \,, \tag{4.5}$$

where m_1 and m_2 are the masses of the two atoms and d is the total distance between them. Using these distances, the moments of inertia about each axis can be calculated as

$$I = I_\zeta = I_\eta = m_1 d_1^2 + m_2 d_2^2 = \frac{m_1 m_2}{m_1 + m_2} d^2 = m^* d^2 \,, \tag{4.6}$$

where $m^* = \frac{m_1 m_2}{m_1 + m_2}$. Therefore,

$$\epsilon_{rotation} = \frac{1}{2} m^* d^2 (\omega_\zeta^2 + \omega_\eta^2) \,. \tag{4.7}$$

By assuming that rotational velocities are statistically independent of each other and of the translational velocities, a modified Gaussian distribution for diatomic gases can be written as

$$\mathcal{G}_D(x_i, v_i, \omega_i, t) = \mathcal{G}(x_i, v_i, t) g(x_i, \omega_i, t) = \mathcal{G}(x_i, v_i, t) g_\zeta(x_i, \omega_\zeta, t) g_\eta(x_i, \omega_\eta, t) \,. \tag{4.8}$$

However, due to the symmetry of the diatomic molecule, the angular velocity distribution may be expressed solely as a function of x_i, t and ω, where $\omega^2 = \omega_\zeta^2 + \omega_\eta^2$.

Through a similar derivation of the equilibrium Maxwellian [50], the distribution function for angular velocities can be shown to have the form

$$g(x_i, \omega, t) = g_\zeta(x_i, \omega_\zeta, t) g_\eta(x_i, \omega_\eta, t) = \frac{B(x_i, t)}{\pi} e^{(-B(x_i,t)\omega^2)} \,. \tag{4.9}$$

Making an analogy to the translational degrees of freedom, a rotational temperature can be defined and written as

$$T_{rot}(x_i, t) = \frac{I}{2\kappa B(x_i, t)} \,. \tag{4.10}$$

It follows that

$$g(\omega) = \left(\frac{I}{2\pi\kappa T_{rot}} \right) e^{(\frac{-I}{2\kappa T_{rot}} \omega^2)} = \left(\frac{I}{2\pi\kappa T_{rot}} \right) e^{(-\frac{R}{2}\omega^2)} \,, \tag{4.11}$$

where, using $p = nkT$, a new variable R has been defined:

$$R = \frac{I}{\kappa T_{rot}} = \frac{nI}{p}\left(\frac{T}{T_{rot}}\right) . \tag{4.12}$$

The total velocity distribution for the diatomic gas is therefore given by

$$\mathcal{G}_D(x_i, v_i, \omega, t) = \frac{n^2 I}{(2\pi)^{5/2}(\det\Theta)^{1/2} p}\left(\frac{T}{T_{rot}}\right) e^{(-\frac{1}{2}\Theta_{ij}^{-1}c_i c_j)} e^{(-\frac{1}{2}R\omega^2)} . \tag{4.13}$$

This distribution function is now defined in seven-dimensional space consisting of three position coordinates, three translational velocity components, and an angular velocity dimension. Though the rotational and translational temperatures need not be equal in general, they will become equal only when the gas is in thermodynamic equilibrium. In equilibrium, the particle velocity distribution function for a diatomic gas becomes

$$\mathcal{M}_D(\mathbf{x}, \mathbf{v}, \omega, t) = \frac{nI}{m(2\pi p/\rho)^{5/2}} e^{(-\frac{1}{2}\frac{\rho}{p}[v^2 + \frac{I}{m}\omega^2])} . \tag{4.14}$$

By substituting equation 4.13 into equation 2.18, the following system may be obtained:

$$\frac{\partial \rho}{\partial t} + \frac{\partial}{\partial x_k}(\rho u_k) = 0 , \tag{4.15}$$

$$\frac{\partial}{\partial t}(\rho u_i) + \frac{\partial}{\partial x_k}(\rho u_i u_k + P_{ik}) = 0 , \tag{4.16}$$

$$\frac{\partial}{\partial t}(P_{ij} + \rho u_i u_j) + \frac{\partial}{\partial x_k}(\rho u_i u_j u_k + u_i P_{jk} + u_j P_{ik} + u_k P_{ij}) = \Delta[v_i v_j \mathcal{F}] , \tag{4.17}$$

$$\frac{\partial E_{rot}}{\partial t} + \frac{\partial}{\partial x_k}(u_k E_{rot}) = \Delta\left[\frac{I\omega^2}{2}\right] . \tag{4.18}$$

If it is to be used, the BGK relaxation model, equation 2.11, must now be modified to account for the added degrees of freedom. The relaxation process towards the equilibrium solution, $\mathcal{M}_D$, is now represented by a "two-step" process as follows:

$$\frac{\delta \mathcal{F}}{\delta t} = -\frac{\mathcal{G}_D(x_i, v_i, \omega, t) - \mathcal{F}_D(x_i, v_i, \omega, t)}{\tau_t(x_i, t)} - \frac{\mathcal{F}_D(x_i, v_i, \omega, t) - \mathcal{M}_D(x_i, v_i, \omega, t)}{\tau_r(x_i, t)} . \tag{4.19}$$

In this relaxation-time approximation, the non-equilibrium distribution, $\mathcal{G}_D$, relaxes toward the distribution, $\mathcal{F}_D$, for which the translational degrees of freedom are in equilibrium with each other, but not in equilibrium with the rotational degrees of freedom.

This relaxation will happen on a time scale, τ_t. The gas will then relax from there to an equilibrium distribution, $\mathcal{M}_D$, on a different time scale, τ_r. Approximate expressions are used here to relate the relaxation times to the gas viscosities. They have the following forms [50]:

$$\tau_t = \frac{\mu}{p}\,, \quad \tau_r = \frac{15\mu_B}{4p}\,, \tag{4.20}$$

where μ is the fluid viscosity, μ_B is the bulk viscosity and p is the thermodynamic pressure; empirical relations can be used to determine the related viscosities. Generally, τ_r is larger, but of the same order of magnitude as τ_t.

Using this collision operator, the moment system can be rewritten as

$$\frac{\partial \rho}{\partial t} + \frac{\partial}{\partial x_k}\left(\rho u_k\right) = 0\,, \tag{4.21}$$

$$\frac{\partial}{\partial t}(\rho u_i) + \frac{\partial}{\partial x_k}(\rho u_i u_k + P_{ik}) = 0\,, \tag{4.22}$$

$$\begin{aligned}\frac{\partial}{\partial t}\left(P_{ij} + \rho u_i u_j\right) + \frac{\partial}{\partial x_k}\left(\rho u_i u_j u_k + u_i P_{jk} + u_j P_{ik} + u_k P_{ij}\right) \\ = -\frac{P_{ij} - \frac{1}{3}P_{kk}\delta_{ij}}{\tau_t} - \frac{(\frac{1}{3}P_{kk} - p)\delta_{ij}}{\tau_r}\,,\end{aligned} \tag{4.23}$$

$$\frac{\partial}{\partial t}(E_{rot}) + \frac{\partial}{\partial x_k}(u_k E_{rot}) = -\frac{(E_{rot} - p)}{\tau_r}\,. \tag{4.24}$$

In this system, p is the equilibrium pressure. It is related to the generalized pressure tensor by $P_{ij} = p\delta_{ij} - \tau_{ij}$ and $\frac{1}{3}P_{kk} = p - \frac{1}{3}\tau_{kk}$ where now $\tau_{kk} \neq 0$ for a diatomic gas. Note that it is possible to relate the extra relaxation terms now present in the system by first writing the following conservation equation for the total energy in the system

$$\begin{aligned}\frac{\partial}{\partial t}\left(\frac{1}{2}\rho u^2 + \frac{1}{2}P_{jj} + E_{rot}\right) + \frac{\partial}{\partial x_k}\left(u_k\left[\frac{1}{2}\rho u^2 + \frac{1}{2}P_{jj} + E_{rot}\right] + u_j P_{jk}\right) \\ = -\frac{P_{kk} - 3p}{2\tau_r} - \frac{E_{rot} - p}{\tau_r}\,.\end{aligned} \tag{4.25}$$

As for monatomic gases, the total energy must be conserved, therefore, the relaxation terms must balance. By using the relation $P_{kk} = 3p - \tau_{kk}$, it is a simple matter to show that $\tau_{kk} = 2(E_{rot} - p)$. Using this result it is possible to replace the equilibrium pressure in the system in favour of P_{ij} and E_{rot}. This results in the final form of the governing equations for a diatomic gas given by

$$\frac{\partial \rho}{\partial t} + \frac{\partial}{\partial x_k}\left(\rho u_k\right) = 0\,, \tag{4.26}$$

$$\frac{\partial}{\partial t}(\rho u_i) + \frac{\partial}{\partial x_k}(\rho u_i u_k + P_{ik}) = 0\,, \tag{4.27}$$

$$\frac{\partial}{\partial t}\left(P_{ij} + \rho u_i u_j\right) + \frac{\partial}{\partial x_k}\left(\rho u_i u_j u_k + u_i P_{jk} + u_j P_{ik} + u_k P_{ij}\right) = -\frac{3P_{ij} - P_{kk}\delta_{ij}}{3\tau_t} - \frac{2(P_{kk} - 3E_{rot})}{15\tau_r}\delta_{ij}\,, \tag{4.28}$$

$$\frac{\partial}{\partial t}(E_{rot}) + \frac{\partial}{\partial x_k}(u_k E_{rot}) = -\frac{3E_{rot} - P_{kk}}{5\tau_r}\,. \tag{4.29}$$

In equilibrium, this system of eleven transport equations properly reduces to the Euler equations with one additional equation for the convection of the rotational energy.

4.3 Eigenstructure for Two-Dimensional Flows

For two space dimensions, equations 4.26-4.29 can be rewritten in conservation form as

$$\frac{\partial \mathbf{U}}{\partial t} + \frac{\partial \mathbf{F}_x}{\partial x} + \frac{\partial \mathbf{F}_y}{\partial y} = \mathbf{S}\,, \tag{4.30}$$

where again $\mathbf{U}$ is the vector of conserved variables which can be expressed as

$$\mathbf{U} = \begin{bmatrix} \rho \\ \rho u_x \\ \rho u_y \\ \rho u_x^2 + P_{xx} \\ \rho u_x u_y + P_{xy} \\ \rho u_y^2 + P_{yy} \\ P_{zz} \\ E_{rot} \end{bmatrix}, \tag{4.31}$$

while $\mathbf{F}_x$ and $\mathbf{F}_y$ are x- and y-direction fluxes given by

$$\mathbf{F}_x = \begin{bmatrix} \rho u_x \\ \rho u_x^2 + P_{xx} \\ \rho u_x u_y + P_{xy} \\ \rho u_x^3 + 3u_x P_{xx} \\ \rho u_x^2 u_y + 2u_x P_{xy} + u_y P_{xx} \\ \rho u_x u_y^2 + u_x P_{yy} + 2u_y P_{xy} \\ u_x P_{zz} \\ u_x E_{rot} \end{bmatrix}, \quad \mathbf{F}_y = \begin{bmatrix} \rho u_y \\ \rho u_x u_y + P_{xy} \\ \rho u_y^2 + P_{yy} \\ \rho u_x^2 u_y + 2u_x P_{xy} + u_y P_{xx} \\ \rho u_x u_y^2 + u_x P_{yy} + 2u_y P_{xy} \\ \rho u_y^3 + 3u_y P_{yy} \\ u_y P_{zz} \\ u_y E_{rot} \end{bmatrix}. \tag{4.32}$$

The source vector $\mathbf{S}$ of equation 4.30 has the form:

$$\mathbf{S} = \begin{bmatrix} 0 \\ 0 \\ 0 \\ -\frac{1}{3\tau_t}(2P_{xx} - P_{yy} - P_{zz}) - \frac{2}{15\tau_r}(P_{xx} + P_{yy} + P_{zz} - 3E_{rot}) \\ -\frac{1}{\tau_t}P_{xy} \\ -\frac{1}{3\tau_t}(2P_{yy} - P_{xx} - P_{zz}) - \frac{2}{15\tau_r}(P_{xx} + P_{yy} + P_{zz} - 3E_{rot}) \\ -\frac{1}{3\tau_t}(2P_{zz} - P_{xx} - P_{yy}) - \frac{2}{15\tau_r}(P_{xx} + P_{yy} + P_{zz} - 3E_{rot}) \\ -\frac{1}{5\tau_r}(3E_{rot} - P_{xx} - P_{yy} - P_{zz}) \end{bmatrix}.$$

By making use of the Jacobians $\mathbf{A}_c = \frac{\partial \mathbf{F}_x}{\partial \mathbf{U}}$ and $\mathbf{B}_c = \frac{\partial \mathbf{F}_y}{\partial \mathbf{U}}$, equation 4.30 can also be rewritten as

$$\frac{\partial \mathbf{U}}{\partial t} + \mathbf{A}_c \frac{\partial \mathbf{U}}{\partial x} + \mathbf{B}_c \frac{\partial \mathbf{U}}{\partial y} = \mathbf{S}\,. \tag{4.33}$$

These moment equations can also be written in primitive form [50] with the random velocity moments, $\mathbf{W}$, as the solution vector. The system then has the form

$$\frac{\partial \mathbf{W}}{\partial t} + \mathbf{A}_p \frac{\partial \mathbf{W}}{\partial x} + \mathbf{B}_p \frac{\partial \mathbf{W}}{\partial y} = \mathbf{S}\,, \tag{4.34}$$

with coefficient matrices

$$\mathbf{A}_p = \begin{bmatrix} u_x & \rho & 0 & 0 & 0 & 0 & 0 & 0 \\ 0 & u_x & 0 & \frac{1}{\rho} & 0 & 0 & 0 & 0 \\ 0 & 0 & u_x & 0 & \frac{1}{\rho} & 0 & 0 & 0 \\ 0 & 3P_{xx} & 0 & u_x & 0 & 0 & 0 & 0 \\ 0 & 2P_{xy} & P_{xx} & 0 & u_x & 0 & 0 & 0 \\ 0 & P_{yy} & 2P_{xy} & 0 & 0 & u_x & 0 & 0 \\ 0 & P_{zz} & 0 & 0 & 0 & 0 & u_x & 0 \\ 0 & E_{rot} & 0 & 0 & 0 & 0 & 0 & u_x \end{bmatrix} \tag{4.35}$$

and

$$\mathbf{B}_p = \begin{bmatrix} u_y & 0 & \rho & 0 & 0 & 0 & 0 & 0 \\ 0 & u_y & 0 & 0 & \frac{1}{\rho} & 0 & 0 & 0 \\ 0 & 0 & u_y & 0 & 0 & \frac{1}{\rho} & 0 & 0 \\ 0 & 2P_{xy} & P_{xx} & u_y & 0 & 0 & 0 & 0 \\ 0 & P_{yy} & 2P_{xy} & 0 & u_y & 0 & 0 & 0 \\ 0 & 0 & 3P_{yy} & 0 & 0 & u_y & 0 & 0 \\ 0 & 0 & P_{zz} & 0 & 0 & 0 & u_y & 0 \\ 0 & 0 & E_{rot} & 0 & 0 & 0 & 0 & u_y \end{bmatrix}. \tag{4.36}$$

Many numerical techniques for the solution of hyperbolic systems of equations are based on the solution or approximate solution of many one-dimensional Riemann problems to determine the flux of conserved quantities between computational cells or elements [13, 51, 52, 53]. In order to make use of these approximate flux functions in the numerical solution of equations 4.26–4.29, the eigenstructure of the system must be known. In particular, to make use of the HLLE flux function [51, 52], the eigenvalues of the flux Jacobian, $\mathbf{A}_c = \frac{\partial \mathbf{F}}{\partial \mathbf{U}}$, must be known. Additionally, the right eigenvectors of the flux Jacobian, $\mathbf{A}_c$, and the left eigenvectors of the coefficient matrix, $\mathbf{A}_p$, from the primitive form of the system of the moment equations are needed in order to use Roe's approximate Riemann solver [53]. It is sufficient to determine the eigenstructure of the matrices associated with the x-direction, $\mathbf{A}_c$ and $\mathbf{A}_p$, as it is typical to make a rotation of the frame of reference each time a numerical flux is needed, such that the local normal to a cell or element is aligned with the x direction.

Defining $\rho c_{xx}^2 = P_{xx}$, the eight eigenvalues of $\mathbf{A}_c$ and $\mathbf{A}_p$ are

$$\lambda_{1-8} = \left(u_x - \sqrt{3}c_{xx},\ u_x - c_{xx},\ u_x,\ u_x,\ u_x,\ u_x,\ u_x + c_{xx},\ u_x + \sqrt{3}c_{xx} \right) .$$

These represent the wave speeds of the fundamental solution modes for the model. The corresponding right eigenvectors for the conserved variables are

$$r_{c1} = \begin{bmatrix} 1 \\ u_x - \sqrt{3}c_{xx} \\ u_y - \frac{\sqrt{3}P_{xy}}{c_{xx}\rho} \\ 3c_{xx}^2 - 2\sqrt{3}u_x c_{xx} + {u_x}^2 \\ \frac{u_x \rho u_y c_{xx} - u_x \sqrt{3} P_{xy} - \sqrt{3} c_{xx}^2 \rho u_y + 3 c_{xx} P_{xy}}{c_{xx}\rho} \\ \frac{\rho^2 u_y^2 c_{xx}^2 - 2\sqrt{3} P_{xy} c_{xx} \rho u_y + \rho c_{xx}^2 P_{yy} + 2 P_{xy}^2}{\rho^2 c_{xx}^2} \\ \frac{P_{zz}}{\rho} \\ \frac{E_{rot}}{\rho} \end{bmatrix} , \ r_{c2} = \begin{bmatrix} 0 \\ 0 \\ 1 \\ 0 \\ u_x - c_{xx} \\ 2\left(u_y - \frac{P_{xy}}{c_{xx}\rho}\right) \\ 0 \\ 0 \end{bmatrix} ,$$

$$r_{c3} = \begin{bmatrix} 1 \\ u_x \\ u_y \\ u_x^2 \\ u_x u_y \\ u_y^2 \\ 0 \\ 0 \end{bmatrix}, \; r_{c4} = \begin{bmatrix} 0 \\ 0 \\ 0 \\ 0 \\ 0 \\ 1 \\ 0 \\ 0 \end{bmatrix}, \; r_{c5} = \begin{bmatrix} 0 \\ 0 \\ 0 \\ 0 \\ 0 \\ 0 \\ 1 \\ 0 \end{bmatrix}, \; r_{c6} = \begin{bmatrix} 0 \\ 0 \\ 0 \\ 0 \\ 0 \\ 0 \\ 0 \\ 1 \end{bmatrix},$$

$$r_{c7} = \begin{bmatrix} 0 \\ 0 \\ 1 \\ 0 \\ u_x + c_{xx} \\ 2\left(u_y + \frac{P_{xy}}{c_{xx}\rho}\right) \\ 0 \\ 0 \end{bmatrix}, \; r_{c8} = \begin{bmatrix} 1 \\ u_x + \sqrt{3}c_{xx} \\ u_y + \frac{\sqrt{3}P_{xy}}{c_{xx}\rho} \\ 3c_{xx}^2 + 2\sqrt{3}u_x c_{xx} + {u_x}^2 \\ \frac{u_x \rho u_y c_{xx} + u_x \sqrt{3} P_{xy} + \sqrt{3} c_{xx}^2 \rho u_y + 3 c_{xx} P_{xy}}{c_{xx}\rho} \\ \frac{\rho^2 u_y^2 c_{xx}^2 + 2\sqrt{3} P_{xy} c_{xx} \rho u_y + \rho c_{xx}^2 P_{yy} + 2 P_{xy}^2}{\rho^2 c_{xx}^2} \\ \frac{P_{zz}}{\rho} \\ \frac{E_{rot}}{\rho} \end{bmatrix}.$$

By constructing a matrix $\mathbf{R}_c$ containing the eight right eigenvectors for conserved variables as columns, a matrix $\mathbf{R}_p$ containing the right eigenvectors for primitive variables can be found by the relation $\mathbf{R}_p = \left(\frac{\partial \mathbf{U}}{\partial \mathbf{W}}\right)^{-1} \mathbf{R}_c$. By inverting $\mathbf{R}_p$ it is then possible to determine a matrix of left eigenvectors for primitive variables, $\mathbf{L}_p = \mathbf{R}_p^{-1}$. These left eigenvectors are

$$l_{p1} = \left[0, -\frac{\rho\sqrt{3}}{6c_{xx}}, 0, \frac{1}{6c_{xx}^2}, 0, 0, 0, 0\right],$$

$$l_{p2} = \left[0, -\frac{P_{xy}}{2c_{xx}^2}, \frac{\rho}{2}, \frac{P_{yx}}{2\rho c_{xx}^3}, -\frac{1}{2c_{xx}}, 0, 0, 0\right],$$

$$l_{p3} = \left[1, 0, 0, -\frac{1}{3c_{xx}^2}, 0, 0, 0, 0\right],$$

$$l_{p4} = \left[0, 0, 0, -\frac{\rho c_{xx}^2 P_{yy} - 4P_{xy}^2}{3\rho^2 c_{xx}^4}, -\frac{2P_{xy}}{c_{xx}^2 \rho}, 1, 0, 0\right],$$

$$l_{p5} = \left[0, 0, 0, -\frac{P_{zz}}{3c_{xx}^2 \rho}, 0, 0, 1, 0\right],$$

$$l_{p6} = \left[0, 0, 0, -\frac{E_{rot}}{3c_{xx}^2 \rho}, 0, 0, 0, 1\right],$$

$$l_{p7} = \left[0, -\frac{P_{xy}}{2c_{xx}^2}, \frac{\rho}{2}, -\frac{P_{yx}}{2\rho c_{xx}^3}, \frac{1}{2c_{xx}}, 0, 0, 0\right] ,$$

$$l_{p8} = \left[0, \frac{\rho\sqrt{3}}{6c_{xx}}, 0, \frac{1}{6c_{xx}^2}, 0, 0, 0, 0\right] .$$

The eigenstructure of $\mathbf{B}_c$ and $\mathbf{B}_p$ can be explored in the same manner and is very similar.

A detailed analysis of the nature of the waves associated with the 10-moment model has been done by Brown *et al.* [11, 12] as well as by Hittinger [50]. These authors show that the fundamental wave modes associated with λ_1 and λ_8 are acoustic waves and are truly non-linear and the waves associated with λ_2 and λ_7 are shear waves. Finally, the waves associated with λ_3–λ_6 contain an entropy wave, two transverse pressure waves and a rotational energy wave.

4.3.1 Roe-Average State

For the linearized approximate Riemann solver of Roe, an appropriate average solution state is required satisfying Roe's property U [53]. A suitable Roe-average state can be determined using the assumed-form or corrected-average approach described by Brown [12] and Brown *et al.* [11]. Letting $W_{ij} = \frac{P_{ij}}{\rho}$, values of the primitive variables defining the Roe-average solution state for the Gaussian closure can be shown to be:

$$\hat{\rho} = \sqrt{\rho_L \rho_R}\,, \quad \hat{u}_i = \frac{\sqrt{\rho_R}u_{iR} + \sqrt{\rho_L}u_{iL}}{\sqrt{\rho_R} + \sqrt{\rho_L}}\,, \tag{4.37}$$

$$\hat{W}_{ij} = \frac{\sqrt{\rho_R}W_{ijR} + \sqrt{\rho_L}W_{ijL}}{\sqrt{\rho_R} + \sqrt{\rho_L}} + \frac{1}{3}\frac{\sqrt{\rho_L\rho_R}}{(\sqrt{\rho_R} + \sqrt{\rho_L})^2}\Delta u_i \Delta u_j\,, \tag{4.38}$$

$$\hat{E}_{rot} = \frac{\sqrt{\rho_R}E_{rotR} + \sqrt{\rho_L}E_{rotL}}{\sqrt{\rho_R} + \sqrt{\rho_L}}\,. \tag{4.39}$$

4.4 Solid-Wall Boundary Conditions

Appropriate solid-wall boundary conditions for the Gaussian closure are not immediately obvious. One technique for determining the solution at a wall is to assume that there exists a Knudsen layer next to the solid surface [7] as illustrated in figure 4.1. In this infinitesimally thin layer, the fluid exists as a combination of the distribution function defining incoming particles from the interior flow field and a distribution function defining reflected particles arising from the wall. For example, for a solid wall extending in

Figure 4.1: Knudsen layer at solid-wall.

the x direction with a fluid above it, all the particles with negative y-direction velocities in the Knudsen layer will come from the neighbouring fluid with statistical properties defined by the Gaussian. In order to model the particle interaction with the wall, an accommodation coefficient, $0 \leq \alpha \leq 1$, is then defined. If α is zero (specular reflection), the incoming particles will simply be reflected specularly from the wall back into the Knudsen layer. For $\alpha = 1$ (diffuse reflection), incoming particles are fully accommodated and will therefore come into thermodynamic equilibrium with the wall before being released from the wall and will re-enter the Knudsen layer with the statistical properties of a Maxwell-Boltzmann distribution defined by a wall temperature, T_w. For any intermediate α value, the reflected particles will enter the Knudsen layer as a combination of the two cases. Note that experimental observations suggest that most materials exhibit accommodation coefficients near unity [19]. The resulting distribution function for the Knudsen layer is then given by

$$\mathcal{F}_{\text{Kn}} = \mathcal{F}^{+} + \mathcal{F}^{-}\,, \tag{4.40}$$

where $\mathcal{F}^{+}$ and $\mathcal{F}^{-}$ are given by

$$\mathcal{F}^{-} = \begin{cases} \mathcal{G}_b(v_x, v_y, v_z) & for \quad v_y < 0\,, \\ 0 & for \quad v_y > 0\,, \end{cases}$$

$$\mathcal{F}^{+} = \begin{cases} \alpha\mathcal{M}_w(v_x, v_y, v_z) + (1-\alpha)\mathcal{G}_b(v_x, -v_y, v_z) & for \quad v_y > 0\,, \\ 0 & for \quad v_y < 0\,, \end{cases}$$

and where $\mathcal{G}_b$ is Gaussian distribution at the edge of the Knudsen layer and $\mathcal{M}_w$ is the Maxwellian defining particles which are fully accommodated by the wall. By assuming that the bulk y-direction velocity of the fluid immediately above the wall is zero and by imposing the constraint that the net particle flux through the wall must be zero, it is possible to show that the reflected Maxwellian has the form

$$\mathcal{M}_w(v_x, v_y, v_z) = \sqrt{\frac{nP_{yy}}{kT_w}} \left(\frac{m}{2\pi k T_w}\right)^{\frac{3}{2}} e^{-\left(\frac{m}{2kT_w}\right)\left((v_x - u_{wx})^2 + v_y^2 + v_z^2\right)}\,, \tag{4.41}$$

where all the properties are those of the fluid outside the Knudsen layer with the exception of T_w, which is the temperature of the wall and u_{wx}, which is the x-direction velocity of the wall. A quick inspection of the first term in this distribution function finds that it relates the number density of the reflected Maxwellian to that of the incoming Gaussian distribution such that

$$\frac{n_{Maxwellian}}{n_{Gaussian}} = \sqrt{\frac{mP_{yy}}{\rho k T_w}}\,. \tag{4.42}$$

If it is assumed that the wall temperature is equal to the temperature of the gas normal to the boundary, this ratio will be one, and equation 4.41 simplifies to become

$$\mathcal{M}_w(v_x, v_y, v_z) = n\left(\frac{m}{2\pi k T}\right)^{\frac{3}{2}} e^{-\left(\frac{m}{2kT}\right)\left((v_x-u_{wx})^2+v_y^2+v_z^2\right)}\,, \tag{4.43}$$

where T is now the temperature of the fluid normal to the wall.

Requiring the component of the bulk velocity of the fluid normal to solid walls to be zero is a very natural boundary condition for the Gaussian closure and provides one value for the required boundary data. The eigenvalues of the system, however, suggest that two boundary data are required to ensure that the problem is well-posed. Realizing that in the equilibrium limit, with no accommodation at the wall, the wall shear stress must be zero in order to recover the Euler equations, it seems that a boundary condition for P_{xy} would be most appropriate. In order to find this condition, the appropriate velocity moment of $\mathcal{F}_{\mathrm{Kn}}$ must be evaluated. The bulk velocity of the Knudsen-layer velocity distribution defined by equation 4.40 is also required as an intermediate step, this velocity however is not enforced as a boundary condition. It then follows that the following boundary conditions are appropriate for the Gaussian closure in the case of a solid wall extending in the x-direction:

$$\begin{aligned} u_{y\,\mathrm{Kn}} = 0\,, \quad P_{xy\,\mathrm{Kn}} &= \alpha\left[\frac{P_{xy}}{2} - \sqrt{\frac{\rho P_{yy}}{2\pi}}(u_x - u_{x\,\mathrm{Kn}}) + \sqrt{\frac{\rho_w n_w k T_w}{2\pi}}(u_{wx} - u_{x\,\mathrm{Kn}})\right]\,, \\ u_{x\,\mathrm{Kn}} &= (2-\alpha)\left[\frac{u_x}{2} - \frac{P_{xy}}{\sqrt{2\pi\rho P_{yy}}}\right] + \frac{\alpha}{2}\sqrt{\frac{P_{yy}}{n_w k T_w}}u_{wx} \end{aligned} \tag{4.44}$$

with all properties being those of the incoming Gaussian distribution with the exception of: ρ_w, n_w, u_{wx}, and T_w, which are defined by the Maxwellian reflected from the wall. It can easily be seen that this recovers the proper "no-shear" limit for specular reflection ($\alpha = 0$). If the wall temperature is again assumed to be equal to the fluid's normal temperature, the relations of equation 4.44 can be simplified and take the form:

$$u_{y\,\mathrm{Kn}} = 0\,, \quad P_{xy\,\mathrm{Kn}} = \alpha\left[\frac{P_{xy}}{2} + \sqrt{\frac{\rho P_{yy}}{2\pi}}(u_{wx} - u_x)\right]\,, \tag{4.45}$$

where all properties are those of the fluid, with the exception of u_{wx}, which corresponds to the velocity of the wall. These simplified boundary conditions are no longer a function of the bulk velocity of the fluid in the Knudsen layer, $u_{x\,\mathrm{Kn}}$. The boundary conditions given in equation 4.45 are used for all the mirco-scale flow applications considered in this thesis. Additional analysis of solid-wall boundary conditions for the Gaussian closure is given in the recent paper by Khieu *et al.* [54].

4.5 Numerical Solution of the Gaussian Moment Equations

The application of the Gaussian moment equations to several canonical flow problems has been previously investigated [14, 26]. These studies have found that, for flows where heat transfer does not play a significant role, the 10-moment equations do a very good job of predicting flow behaviour in the continuum and transition regime. The numerical scheme used is summarized here as it forms the base of new advancements which are presented in the subsequent chapters. A selection of numerical results obtained using the Gaussian moment equations is also offered as they serve as comparisons in later chapters. Care was taken to ensure that grid resolution was sufficient for accurate numerical results in each case. For all of the cases considered below, values for the mean free path, λ, used to define the Knudsen number were determined using the expression for hard-sphere collisional processes given by Bird [3] as

$$\lambda = \frac{16\mu}{5(2\pi\rho p)^{\frac{1}{2}}}\,. \tag{4.46}$$

4.5.1 Godunov-Type Finite-Volume Scheme

A parallel higher-order Godunov-type finite-volume scheme has been developed for the solution of the transport equations of the Gaussian closure for two-dimensional planar flows on multi-block quadrilateral meshes. As the relaxation times, τ_t and τ_r, can become very small in the near-equilibrium limit, a point-implicit time marching method is used to integrate the set of ordinary differential equations that result from the spatial discretization of the governing equations and deal with excessive numerical stiffness associated with the source terms. The fully-discrete finite-volume formulation with second-order

semi-implicit time marching applied to cell (i,j) is given by

$$\tilde{\mathbf{U}}^{n+1}_{(i,j)} = \mathbf{U}^{n}_{(i,j)} - \frac{\Delta t}{A_{(i,j)}} \left(\sum_{k} (\mathbf{F}_k \cdot n_k \, \Delta\ell)^{n}_{(i,j,k)} \right) + \Delta t \, \tilde{\mathbf{S}}^{n+1}_{(i,j)} \,, \tag{4.47}$$

$$\begin{aligned} \mathbf{U}^{n+1}_{(i,j)} = \mathbf{U}^{n}_{(i,j)} - \frac{\Delta t}{2A_{(i,j)}} \left(\sum_{k} (\mathbf{F}_k \cdot n_k \, \Delta\ell)^{n}_{(i,j,k)} + \sum_{k} (\tilde{\mathbf{F}}_k \cdot n_k \, \Delta\ell)^{n+1}_{(i,j,k)} \right) \\ + \Delta t \left(\frac{\mathbf{S}^{n}_{(i,j)} + \tilde{\mathbf{S}}^{n+1}_{(i,j)}}{2} \right) , \end{aligned} \tag{4.48}$$

where $\mathbf{U}_{(i,j)}$ is the conserved solution vector for cell (i,j), $\mathbf{F}_k$ is the flux dyad evaluated at the kth quadrature point along the boundary of the cell, $A_{(i,j)}$ is the area of the cell, $\Delta\ell$ and $\mathbf{n}_k$ are the length of the cell face and unit vector normal to the cell face or edge, respectively, and the superscript n is the index for the time step of size Δt. The numerical fluxes at the faces of each cell, $(\mathbf{F}_k \cdot n_k \, \Delta\ell)_{(i,j,k)}$, are determined from the approximate solution of a Riemann problem posed in a direction defined by the normal to the face. The left and right solution states for the Riemann problems are determined via a least-squares piece-wise limited linear solution reconstruction procedure with either the Barth-Jesperson or Venkatakrishnan limiters [55, 56]. This provides a second-order accurate spatial discretization for smooth solutions. In the present algorithm, both Roe and HLLE-type approximate Riemann solvers [52, 53] are used to solve the Riemann problem and evaluate the numerical flux. This time marching formulation allows the maximum time step to be determined by the usual CFL condition rather than being governed by the relaxation time scales, τ_t and τ_r, of the stiff source terms.

4.5.2 Parallel Adaptive Mesh Refinement

Following the approach developed by Sachdev *et al.* [57], the finite-volume scheme described above has been combined and implemented within a parallel block-based AMR solution procedure that enables automatic solution-directed mesh adaptation on body-fitted multi-block quadrilateral meshes and leads to an efficient and scalable parallel solution algorithm on distributed-memory multi-processor architectures. The proposed AMR formulation borrows from previous work by Berger and co-workers [58, 59, 60], Quirk [61, 62], and De Zeeuw and Powell [63] for Cartesian meshes and has similarities with the block-based approaches described by Quirk and Hanebutte [62], Berger and Saltzman [59], and Groth *et al.* [64]. Note that other researchers have considered the

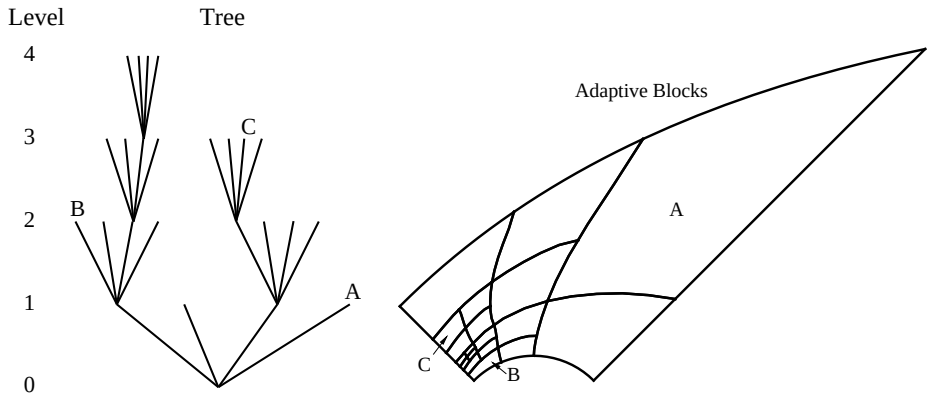

Figure 4.2: Quadtree data structure and block-based refinement for body-fitted mesh showing solution blocks at 4 levels of refinement.

extension of Cartesian mesh adaptation procedures to more arbitrary quadrilateral and hexagonal mesh, for example, Davis and Dannenhoffer [65] and Sun and Takayama [66].

In the AMR scheme, an initial body-fitted multi-block mesh is automatically refined in areas of interest according to several physics-based refinement criteria. This is done by dividing a single "parent" block into four "child" blocks each with the same number of cells as the parent block, thereby doubling the local grid resolution with each refinement. Overlapping ghost-cells are used to pass information from one block to another, making the block boundaries entirely transparent to the solution. The ghost cells are also used for the implementation of boundary conditions. The inter-connectivity of the solution blocks is stored in a tree-like data structure in which new branches are created at each refinement. This "quadtree" data structure allows for the connectivity of the blocks as well as the relative refinement levels to be stored as shown in figure 4.2. Standard multigrid-type restriction and prolongation techniques are used when refining or coarsening blocks and flux corrections must be carried out at interfaces between blocks with different levels of refinement in order to ensure the scheme remains conservative.

The parallel AMR scheme is designed to be easily implemented on large multiprocessor distributed-memory computing facilities. The similarity between blocks of all refinement levels ensures that they each require approximately the same computational effort to update the solution at each time step. Thus, parallel implementation is carried out via domain decomposition where the solution blocks are simply distributed equally among the available processors, with more than one block permitted on each processor.

When equal distibution of blocks is not possible, some processors will have one more block than others and thus more computational work. As the total number of blocks per processor increases, the unbalance caused by this extra block becomes less significant. A Morton ordering space filling curve is used to provide nearest-neighbour ordering of blocks for efficient load balancing [67].

All computations for this study were carried out either on a parallel cluster of four-way Hewlett-Packard ES40, ES45, and Integrity rx4640 servers with a total of 244 Alpha and Itanium 2 processors or a large-scale cluster consisting of 3780 computational nodes each containing two quad-core Intel Xenon 5500 x86-64 processors. Both systems are connected via a low-latency Myrinet network. The implementation was carried out using the C++ programming language and the MPI (message passing interface) library.

Important aspects of the proposed solution algorithm are its high parallel efficiency and scalability. Calculations of the parallel performance and scalability of the algorithm are shown in figure 4.3. The figure depicts the parallel speed-up, S_p, given by

$$S_p = \frac{t_1}{t_p}\,, \tag{4.49}$$

where t_1 is the wall time the computation takes on one processor and t_p is the wall time the computation takes on p processors. The parallel efficiency, E_p, given by

$$E_p = \frac{S_p}{p}\,, \tag{4.50}$$

is also shown. The problem considered is a simple channel-flow problem comprising 80 blocks of 32×64 cells ($163,840$ cell computational mesh). Both S_p and E_p are shown as a function of the number of processors, p. It can be seen that the speed up is linear for up to 80 processors, and even when 80 processors are used, the parallel efficiency remains as high as 96%.

4.5.3 Subsonic Planar Couette Flow

A good first test case to determine the validity of boundary conditions for the Gaussian closure is planar subsonic Couette flow between to oppositely moving infinite plates [68]. This situation is particularly well suited for the Gaussian moment closure as the continuum and free-molecular exact solutions do not have heat transfer. The lack of heat transfer in the moment equations should therefore not lead to errors in either of these situations. It is for this reason that this is a good flow situation to demonstrate the

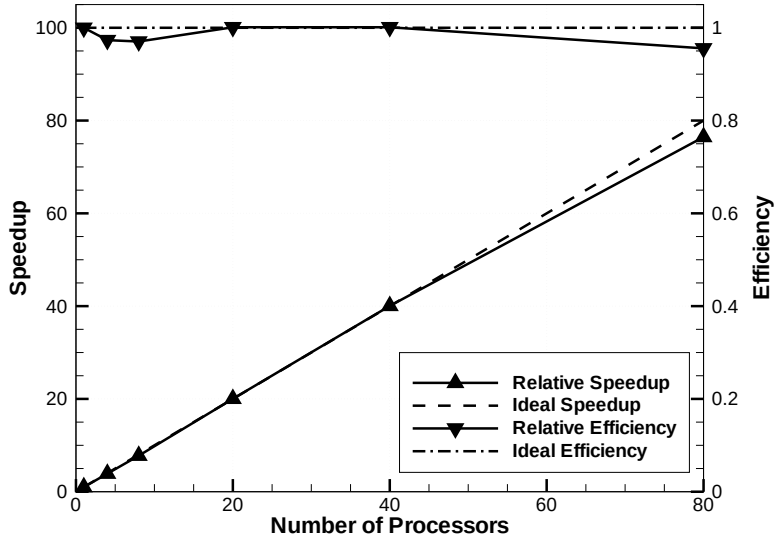

Figure 4.3: Parallel speedup and efficiency for a problem comprising 64 blocks of 32×64 cells.

validity of the boundary treatment across the full range of Knudsen numbers. Figure 4.4 shows both the predicted normalized flow velocity at the wall, u/U, and normalized shear stress, $\frac{\tau_{xy}}{\rho U \sqrt{\frac{2kT}{\pi m}}}$ for the case of Couette flow with two plates moving in opposite directions at velocity U and a fluid at temperature T and density ρ. The fluid in this case is argon at 288K and standard pressure. The two plates move in opposite directions at 30 m/s. The results show that the Gaussian closure is able to reproduce the correct solutions in both the the continuum and free-molecular flow limits and it effectively transitions from the continuum solution to the free-molecular solution in a manner that is in very good agreement with the approximate analytical solution developed by Lees [68].

4.5.4 Flat-Plate Boundary-Layer Flow

After an investigation of Couette flow, a logical step is to consider flat-plate boundary-layer flow. Computed Gaussian solutions for air flow over a finite flat plate with a free-stream Mach number of 0.2 are shown in figure 4.5. The solution for a low-Knudsen-number continuum-flow case ($\mathrm{Kn} = 2 \times 10^{-5}$, $\mathrm{Re} = 1.5 \times 10^{4}$) is shown along with the solution for a higher-Knudsen-number transitional-flow case ($\mathrm{Kn} = 2 \times 10^{-1}$, $\mathrm{Re} = 1.5$). The Gaussian solutions are compared to the classical incompressible boundary-layer flow

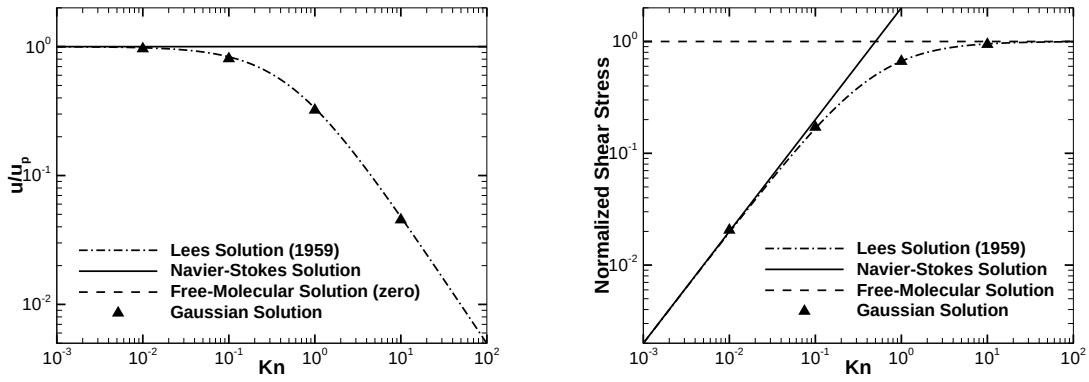

(a) (b)

Figure 4.4: (a) Normalized flow velocity at the wall as a function of Knudsen number. (b) Normalized shear stress as a function of Knudsen number. Both for planar Couette flow between two diffusely reflecting walls.

solution of Blasius [69]. The results for the continuum-flow case clearly demonstrate the ability of the Gaussian closure to reproduce the expected incompressible fluid dynamic solution when collisional process are significant. As expected, the velocity slip at the wall is negligible for the low-Knudsen-number case. Many find it surprising that a purely hyperbolic set of equations can recover a classical result that has traditionally only been modelled by equations with a partially elliptic nature. The results shown here should prove that the hyperbolic Gaussian moment equations clearly recover the correct result in the continuum regime.

Turning to the transition-regime case, the boundary layer now becomes thicker and there is now appreciable slip at the solid boundary; these are both expected characteristics of higher-Knudsen-number flows. The solutions for the flat-plate cases were obtained using a rectangular grid with far-field boundaries a distance ten times the plate length away from the plate. Mesh stretching and adaptive mesh refinement based on the curl of the velocity field were used to cluster cells near the plate. Final mesh resolutions ranged from 42000 to 51000 cells. The symbols on figures 4.5(a) and 4.5(b) correspond to cell-centred values and should give an idea of the resolution used.

Further validation of the Gaussian boundary-layer solutions for the transition regime is sought by comparing the predicted solutions to several Direct Simulation Monte Carlo (DSMC) solutions. Sun and Boyd [70] have carried out a study of the coefficient of

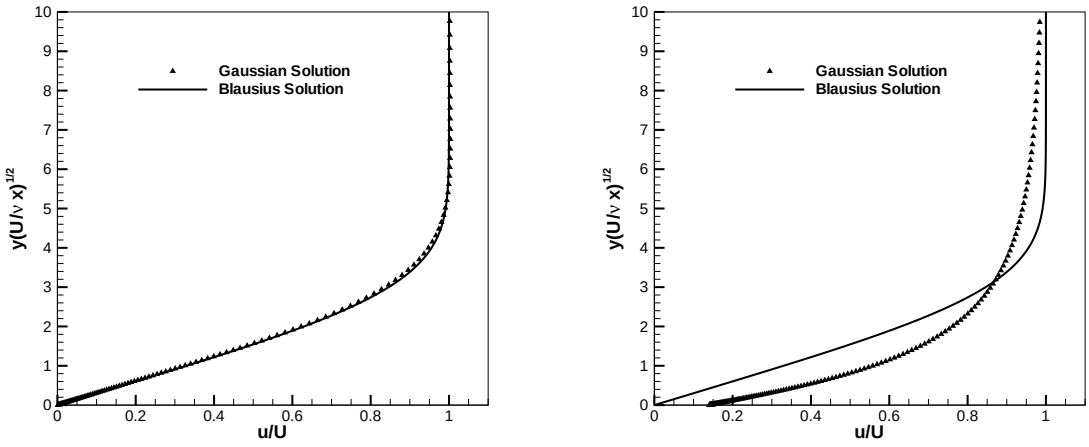

(a) (b)

Figure 4.5: Normalized velocity distribution in the developing boundary layer along a flat plate. (a) Continuum regime; $\mathrm{Kn} = 2 \times 10^{-5}$. (b) Transition regime; $\mathrm{Kn} = 2 \times 10^{-1}$.

drag for a finite flat plate in low-speed rarefied flows. Their results were obtained using DSMC and the Information Preservation method (IP). The IP method is a modified DSMC method that is intended to be more computationally efficient for low-speed flows. Figure 4.6 shows a comparison of the coefficient of drag predicted by both the direct-simulation methods mentioned above and the Gaussian closure. The Blasius [69] and triple-deck [71, 72] solutions for continuum flow ($\mathrm{Kn} \ll 1$) and the analytical result for free-molecular flow [19] ($\mathrm{Kn} \gg 1$) are also shown. Note that the non-equilibrium drag for the transition is significantly higher than predicted by the Blasius solution, this is due to the fact that the Blasius solution is only an approximate solution for incompressible flow over an infinite flat plate while the current situation, which was chosen to make comparison with the DSMC data possible, is a compressible flow over a finite plate with leading- and trailing-edge effects. The triple-deck solution does offer a treatment for trailing-edge effects and it can be observed that in the continuum regime, low Knudsen numbers, agreement with the Gaussian solution is good. Good agreement is observed between all the numerical methods for most of the range of Knudsen numbers. It does, however, appear that the Gaussian model begins to over-predict the drag for a Knudsen numbers greater than approximately unity.

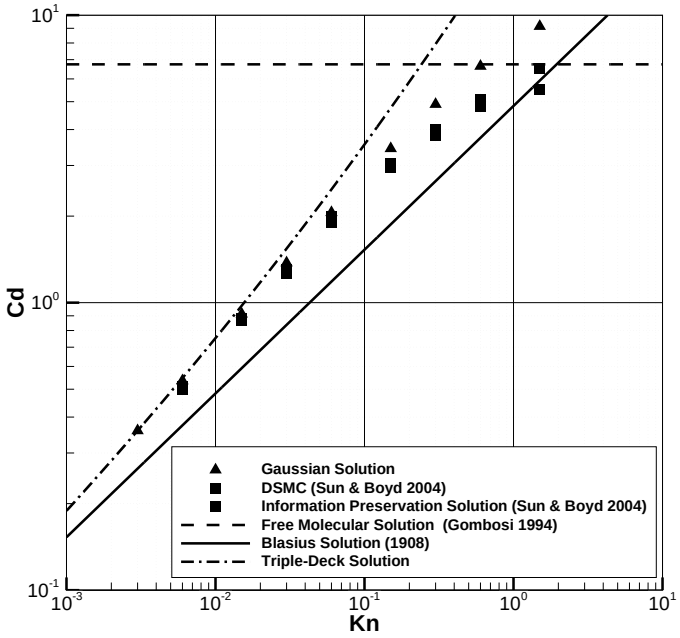

Figure 4.6: Flat-plate drag coefficients at Ma = 0.2 for various Knudsen numbers computed using the Gaussian closure and two DSMC-based methods.

4.5.5 Shock-wave Structure

As gases transition through shock waves, highly non-equilibrium states are produced. This makes shock-structure calculations good test cases for extended fluid-dynamics techniques. The structure of a one-dimensional planar shock for the Gaussian closure has been considered in several other previous works [11, 12, 73]. Unlike the Euler equations, the Gaussian model does not predict a discontinuity for low-Mach-number shocks. Instead the shock structure is fully dispersed with a smooth transition because the fastest wave speed in the Gaussian model is faster than the acoustic waves of the Euler equations. An internal discontinuity does, however, form at the upstream end of the shock resulting in a partially dispersed structure when the fluid speed becomes faster than the fastest leftward moving wave predicted by the system. This wave moves with velocity $u - \sqrt{3P_{xx}/\rho}$. The discontinuity, therefore, becomes apparent when $u > \sqrt{3P_{xx}/\rho}$. For monatomic gases, the Mach number is given by $\mathrm{Ma} = u/\sqrt{5p/3\rho}$ and therefore the discontinuity appears when

$$\mathrm{Ma} = \frac{\sqrt{3P_{xx}/\rho}}{\sqrt{5p/3\rho}} = \sqrt{9/5} \approx 1.34\,,$$

assuming $P_{xx} = p$ upstream of the shock. For diatomic gases, the Mach number is given by $\mathrm{Ma} = u/\sqrt{7p/5\rho}$ and the discontinuity will begin when

$$\mathrm{Ma} = \frac{\sqrt{3P_{xx}/\rho}}{\sqrt{7p/5\rho}} = \sqrt{15/7} \approx 1.46\,.$$

After the discontinuity, there is a region of smooth compression and relaxation where the flow properties relax to their equilibrium values.

For the shock structure calculations presented here, a one-dimensional grid comprising one thousand equally spaced cells was employed. Fixed boundary conditions were used. Normalized density solutions for shocks with Mach numbers of 1.2, 1.5, and 2.0 are presented in figure 4.7 for argon at standard atmospheric pressure and density. Here the density is normalized by the relation

$$\rho^\star = \frac{\rho - \rho_u}{\rho_d - \rho_u}\,,$$

where ρ_u and ρ_d are the upstream and downstream densities respectively. It can be seen that, as expected, for low Mach numbers the fluid undergoes a smooth compression, whereas for higher Mach numbers, the fluid undergoes a compression that is initially discontinuous followed by a smooth relaxation region. The presence of these discontinuous sub-shocks may be undesirable, especially for high-speed flow computations when internal shock structure is important. Later in this work, in chapter 6, a regularization procedure is presented that leads to transport equations that do not predict these sub-shocks. However, hyperbolicity is sacrificed in this technique.

4.5.6 Subsonic Flow Past a Circular Cylinder

There is a reasonable amount of data and theory available in the literature for subsonic steady flow past a circular cylinder. In particular the coefficient of drag, C_d, is available for continuum, transitional, and free-molecular flow regimes. Figure 4.8 shows a comparison of experimental data collected by Coudeville *et al.* [74] with an approximate solution developed by Patterson [75], and solutions from the Gaussian closure for flow past a cylinder at two different speed ratios, S. The speed ratio is the ratio of the bulk speed to the most probable random speed of a particle, it differs from the Mach number by only a constant. The solution due to Patterson is only valid in the region where the Reynolds number is less than 0.5 and where the Knudsen number can be regarded as small (*i.e.*, less than unity). As shown in the figure, this is a very limited range of

validity. The comparisons of figure 4.8 show that the Gaussian solutions are in very good agreement with the experimental results for the continuum regime and the transition regime. However, as the free-molecular regime is approached (Kn $>$ 1), the numerical predictions of the drag coefficient provided by the Gaussian closure is over-estimated. Gaussian solutions for these cases were obtained on a body-fitted grid of $10,000$ cells.

A comparison of the flow structure for subsonic flows past a cylinder with a speed ratio $S = 0.027$ at two different Knudsen numbers is depicted in figure 4.9. Results for $\mathrm{Kn} = 1 \times 10^{-3}$ and $\mathrm{Kn} = 1$ are given. The figures shows that there are marked differences in flow structure of the predicted continuum and non-equilibrium flow solutions. At a Knudsen number of 1×10^{-3}, the flow is clearly separated and there is a significant region of recirculation downstream of the cylinder. This predicted flow structure is in agreement with experimental observations for flows in this regime. For a Knudsen number of unity, the flow remains attached and there is a greater symmetry between the upstream and downstream solutions. Moreover, the flow is perturbed out to much larger relative distances from the cylinder (*i.e.*, out to larger values of r/d where r is the distance from the centre of the cylinder and d is the cylinder diameter) in the non-equilibrium case.

4.5.7 Transonic Flow Past a NACA0012 Micro Airfoil

Lastly, the application of the Gaussian closure to the prediction of transonic steady flow around a NACA0012 micro airfoil at zero angle of attack is now considered. The free-stream values of the flow Mach number, temperature, and density are 0.8, 257 K, and 1.161×10^{-4} Kg/m^3, respectively, and the chord length of the airfoil is 0.04 m. These conditions correspond to a Knudsen number of 0.017 and Reynolds number of 73. Comparisons are made to previous results obtained using a DSMC-based scheme by Sun and Boyd [6] and experimental results obtained by Allegre, Raffin and Lengrand [76]. Normalized density contours are shown in figures 4.10(a)–4.10(c).

It is evident that the results obtained using the standard Gaussian equations agree well with DSMC and experiment at the leading edge, however the density seems to be very under-predicted along the length of the airfoil. A similar finding was reported in the earlier work by Suzuki and van Leer [77]. It will be demonstrated later in chapter 6 of this work that this under-prediction is related to the fact that the Gaussian closure lacks heat transfer.

4.6 Observations

The Gaussian 10-moment model provides a globally hyperbolic treatment for gas flows outside of local thermodynamics equilibrium. Although is does not provide a treatment for heat transfer, the closure accounts for anisotropic pressures that are common in transition-regime flows. This chapter represents the first thorough study of the numerical solutions of these moment equations for a wide range of gas-flow problems. It is clearly demonstrated that they show very good promise for flows approaching a Knudsen number of unity. For higher Knudsen numbers, the agreement between numerical solutions of the Gaussian closure and theoretical, experimental, and/or numerical results is not as good and it is speculated that the disagreement in some cases may be due to the lack of thermal transport by random particle motion. A Godunov-type finite-volume scheme with AMR is shown to be effective in the solution of these moment equations and an efficient parallel implementation is readily achieved. Moreover, the computational costs associated with the solution of the Gaussian moment equations is only 1.5 to 2.0 times more expensive than an equivalent Euler calculation on the same mesh, making the closure significantly more affordable than other treatments for non-equilibrium flow prediction.

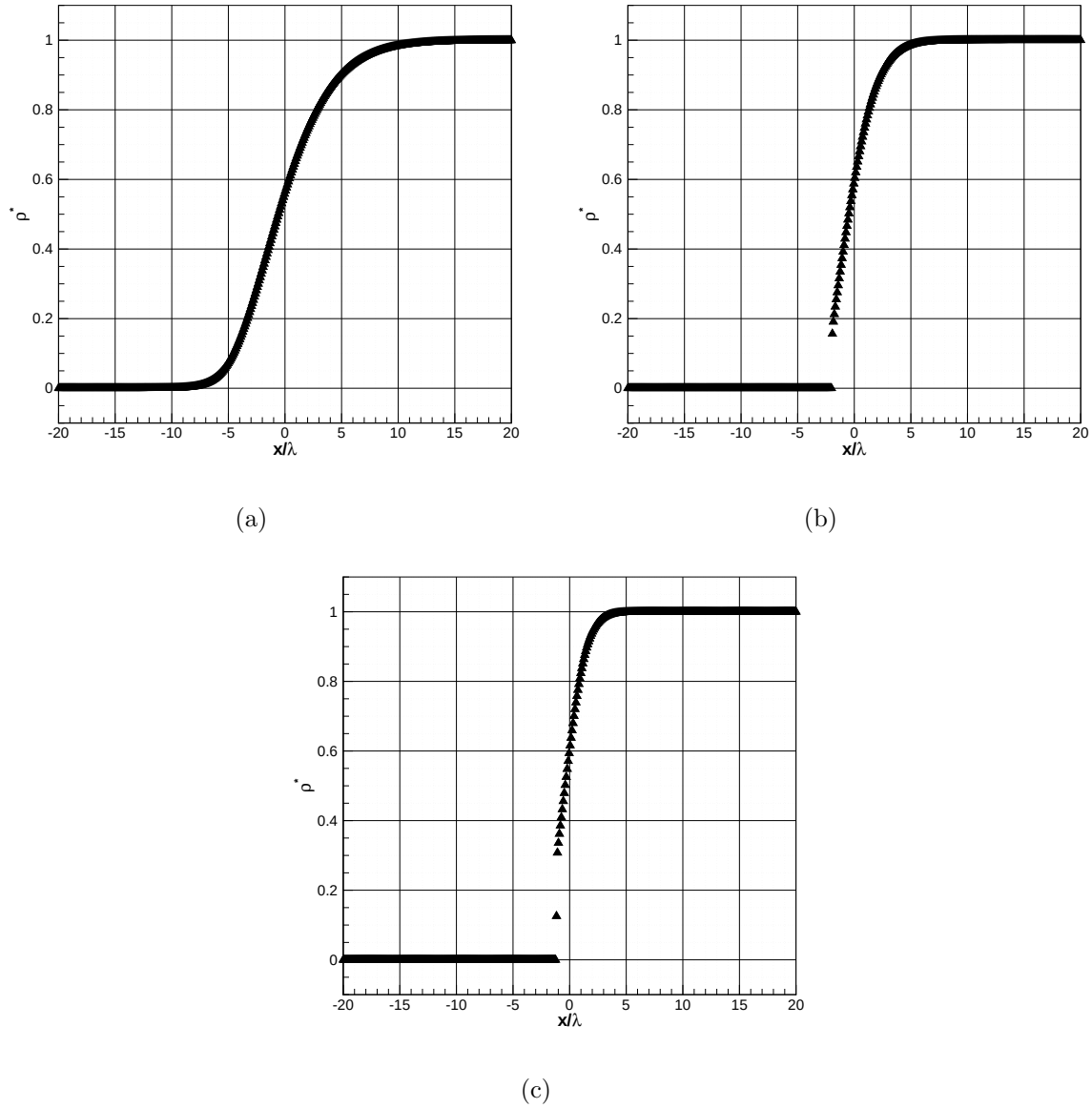

Figure 4.7: Normalized density variations through shock waves with shock Mach numbers of (a) $\mathrm{Ma_s} = 1.2$, (b) $\mathrm{Ma_s} = 1.5$, and (c) $\mathrm{Ma_s} = 2$ as predicted by the Gaussian model.

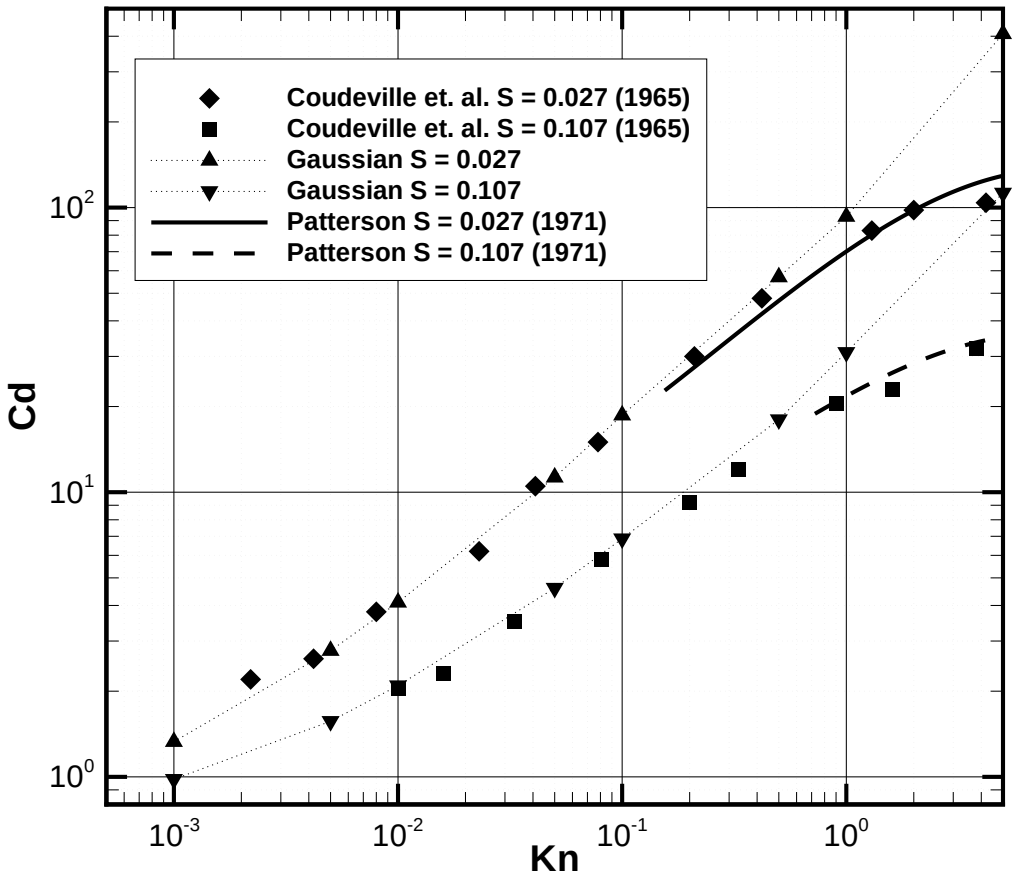

Figure 4.8: Coefficient of drag for airflow past a circular cylinder at two speed ratios (S): experimental results of Coudeville *et al.*, approximate solution due to Patterson, and Gaussian solution.

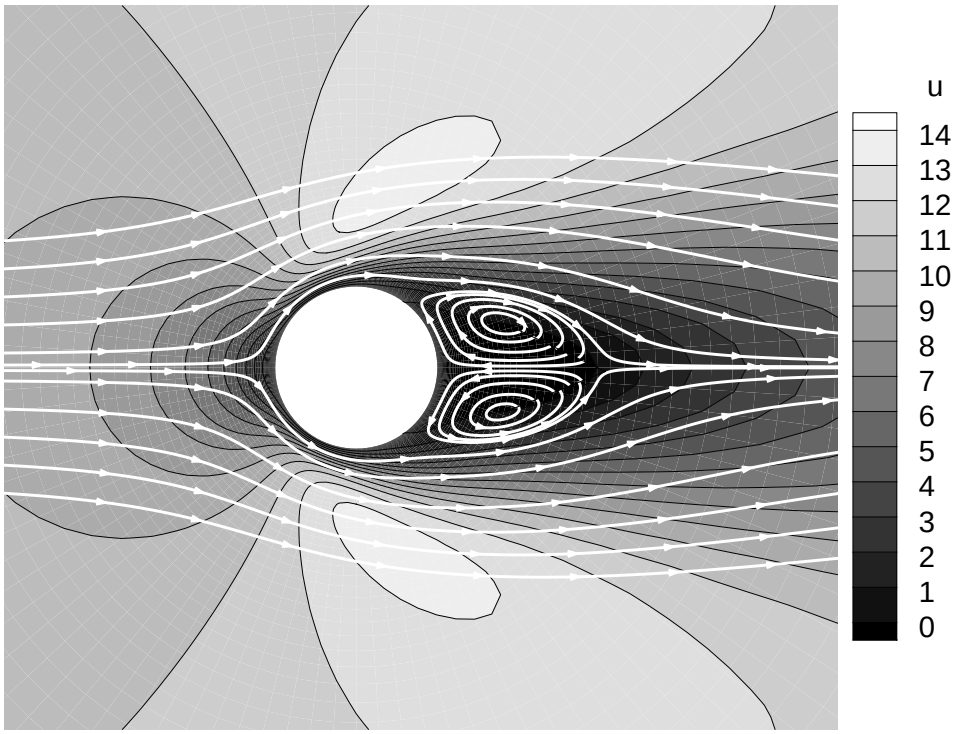

(a)

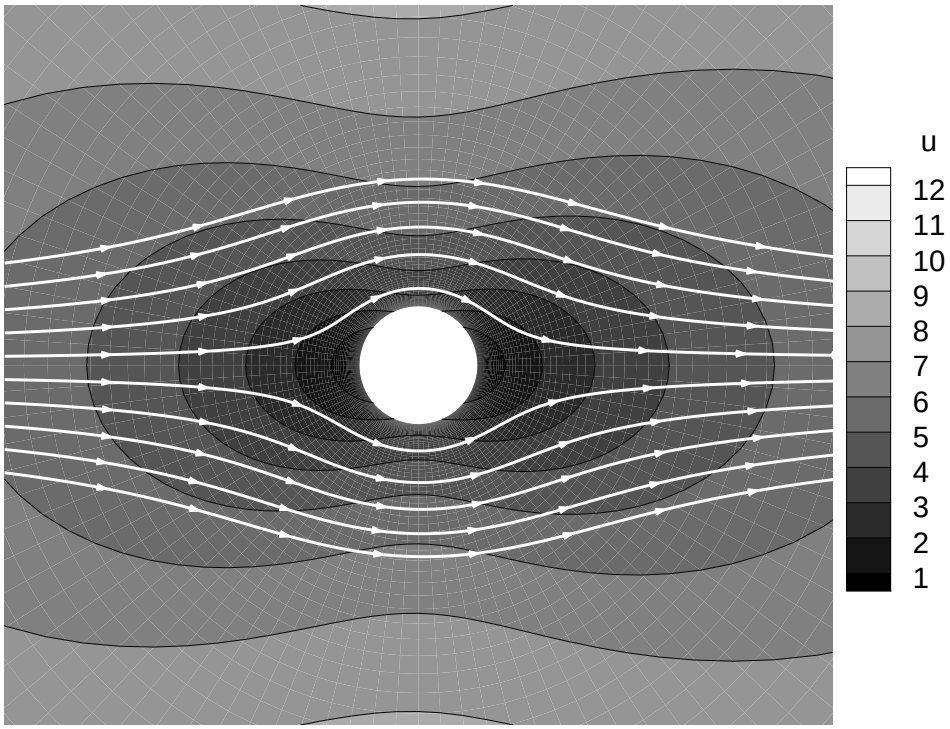

(b)

Figure 4.9: Comparison of x-direction velocity contours for flow past a circular cylinder at a speed ratio $S = 0.027$. (a) $\mathrm{Kn} = 1 \times 10^{-3}$. (b) $\mathrm{Kn} = 1$.

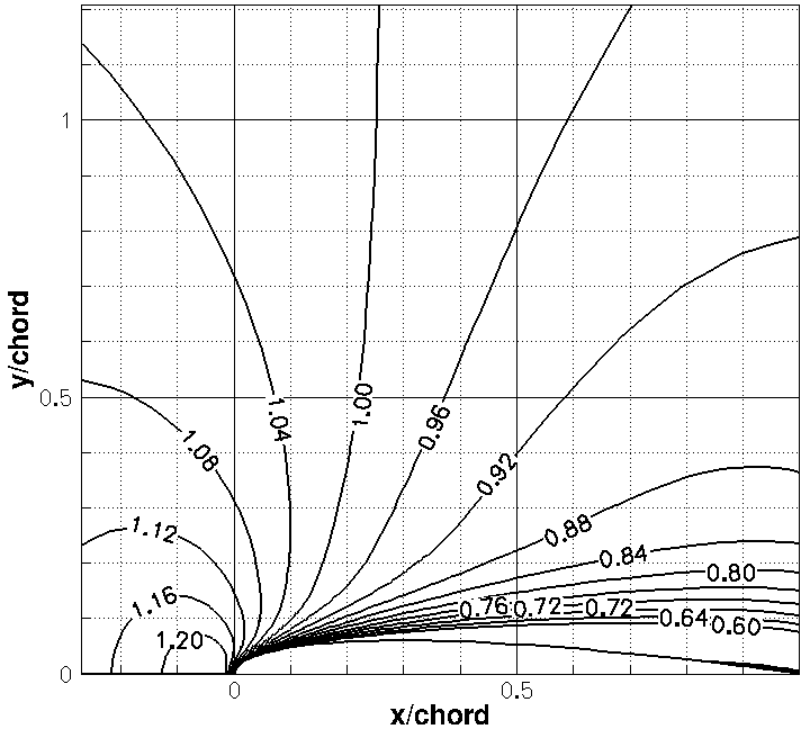

(a)

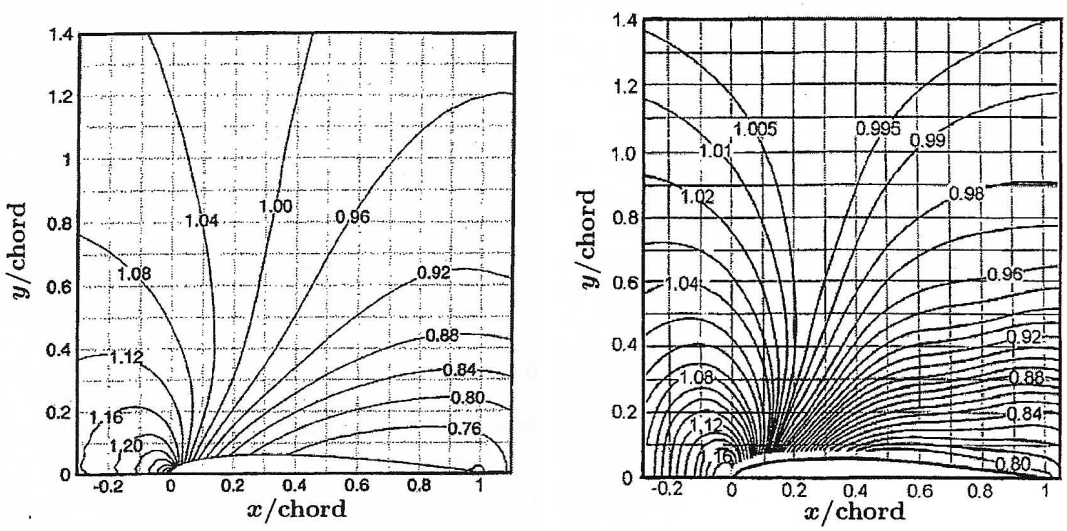

(b) (c)

Figure 4.10: Comparison of the normalized density contours around a NACA0012 micro airfoil: (a) predictions of the standard Gaussian moment equations, (b) predictions of the DSMC-based method of Sun and Boyd [6] and (c) experimental data of Allegre, Raffin and Lengrand [76].

Chapter 5

Gaussian Moment Closure with Embedded Boundaries

One of the main advantages that moment closures offer over traditional fluid-dynamic equations is their hyperbolic nature. Not only is this physically pleasing, as hyperbolicity ensures finite speeds of propagation within the system, but it also provides several computational advantages. Firstly, typical numerical schemes for the solution of PDEs tend to be well-suited for the solution of either hyperbolic or elliptic equations. Schemes that handle both equation types with equal elegance are rare. The ability to model viscous compressible gas flows in a purely hyperbolic manner can therefore be regarded as advantageous. This will be demonstrated clearly in the present chapter.

In addition to simplifying the design of numerical solution techniques, the first-order nature of moment equations can lead to increases in accuracy for several reasons. Firstly, for a given stencil or reconstruction order, the requirement to only approximate first derivatives during the numerical solution of moment equations can lead to an extra order of spacial accuracy as compared to the solution of equations which require second derivatives, such as the Navier-Stokes equations. Moreover, many numerical rules for the evaluation of derivatives become more sensitive to grid irregularities for higher-order derivatives. Moment equations can therefore be said to have another advantage over traditional fluid-dynamic equations: their numerical solution is less sensitive to grid quality. This will be demonstrated in a practical sense in this chapter.

In chapter 4, the ability of the Gaussian moment closure to accurately describe a range of continuum and non-continuum flows was shown. In this chapter, the moment closure insensitivity to grid irregularities is demonstrated for a mesh-adjustment scheme

that performs local alterations to a body-fitted mesh at embedded, possibly moving boundaries. These boundaries are not necessarily aligned with the underlying grid. The particular grid-movement technique used in this study is that developed by Sachdev and Groth [16, 17].

5.1 Spacial Discretization

For this implementation, spacial and temporal discretizations that are very similar to those outlined in chapter 4 are utilized. The added complexity is that the effects caused by the varying geometry of cells associated with moving boundaries must be taken into account. As before, flow domains are tessellated into blocks containing non-overlapping cells. Blocks can be connected in an unstructured manner, but cells within a block are structured quadrilaterals and can be indexed using i-j indices. If numerical quadrature is used to calculate inter-cellular fluxes, the time rate of change of the average of the conserved moments in a cell (i, j) can be written as

$$\frac{\mathrm{d}\mathbf{U}_{(i,j)}}{\mathrm{d}t} = -\frac{1}{A_{(i,j)}} \sum_k \left[(\mathbf{F}_k - w_k \mathbf{U}_k) \cdot n_k \, \Delta\ell \right]_{(i,j,k)} - \left(\frac{\mathbf{U}}{A_{(i,j)}} \frac{\mathrm{d}A_{(i,j)}}{\mathrm{d}t} \right)_{(i,j)} + \mathbf{S}_{(i,j)} \,, \tag{5.1}$$

where $A_{(i,j)}$ is the area of the cell, while w_k, n_k, and $\Delta\ell$ are the velocity of, unit normal to, and length of the kth cell face or edge respectively. The flux dyad is given by $\mathbf{F}_k$ and $\mathbf{U}_k$ is the solution state, both evaluated at the quadrature point on the kth face. The term on the right-hand side of this equation containing the factor $\mathrm{d}A_{(i,j)}/\mathrm{d}t$ corresponds to the time rate of change of the cell area. This term is approximated by the geometric conservation law that states that the change in cell area is equal to the area swept by the moving surfaces [78]. Given left and right solution states, $\mathbf{U}_{(L)}$ and $\mathbf{U}_{(R)}$, at each cell interface, the numerical flux given by

$$(\mathbf{F}_l - w_l \mathbf{U}_l) \cdot n_l = \mathfrak{F}(\mathbf{U}_{(L)}, \mathbf{U}_{(R)}, w_l, n_l) \,, \tag{5.2}$$

where $\mathfrak{F}$ is the numerical flux, is computed by approximately solving a Riemann problem in a frame of reference that is rotated to be aligned with the normal to the face and translated with the edge velocity. The left and right solution states are again determined via a least-squares, piecewise-linear reconstruction procedure in conjunction with the slope limiter of Venkatakrishnan [55, 56]. This allows second-order spacial accuracy in smooth regions and first-order accuracy at discontinuities. Roe's approximate Riemann

solver [53] is used to solve the Riemann problem and evaluate the numerical flux. The ordinary differential equations of equation 5.1 are integrated forward in time using the same time-marching scheme given in equations 4.47 and 4.48.

5.1.1 Mesh-Adjustment Scheme

The insensitivity to grid irregularities of moment equations as compared to other fluid-dynamic equations is shown here for a mesh-adjustment scheme proposed recently by Sachdev and Groth [16, 17]. The mesh-adjustment scheme provides an automated treatment for both fixed and moving, non-grid-aligned boundaries embedded in a body-fitted, multi-block mesh. Similar in nature to the Cartesian-cut-cell methods developed by Bayyuk *et al.* [79] and Murman *et al.* [80], this scheme allows for the nodes of an underlying body-fitted mesh to be adjusted so as to coincide with the embedded boundary. By making only local alterations to the grid, this scheme enables the solution of unsteady flows involving moving boundaries or for steady flow problems involving stationary boundaries that are not necessarily aligned with the mesh, while preserving the structured nature of the blocks and avoiding the creation of small cut cells that are often generated by traditional cut-cell approaches. In addition, the mesh-adjustment algorithm is fully compatible with block-based AMR and parallel implementation via domain decomposition used in the finite-volume scheme described above. A brief summary of the mesh-adjustment scheme is given in what follows. Full details are contained in the papers by Sachdev and Groth [16, 17].

Mesh adjustment is carried out in several steps. Firstly, a pre-mesh-adjustment flagging is used in order to determine which cells may require adjustment. The nodal locations of each cell is compared to bounding boxes that are constructed for each interface; a cell is known to be active if all four of its nodes lie outside all bounding boxes. Next, if the cell is partially or entirely contained in a bounding box, intersections between the edges of the cell and each boundary are sought. If no intersections exist, a ray-tracing algorithm is employed to determine if the cell is entirely inside or outside of the boundaries. This ray-tracing entails counting the number of intersections between the embedded boundary and a line connecting the cell centroid to a reference point within the boundary. An odd number of intersections indicates that the cell is outside of the interface. These cells are used during the solution of the fluid equations and are tagged as “active” cells. Conversely, an even number of intersections indicates that the cell is

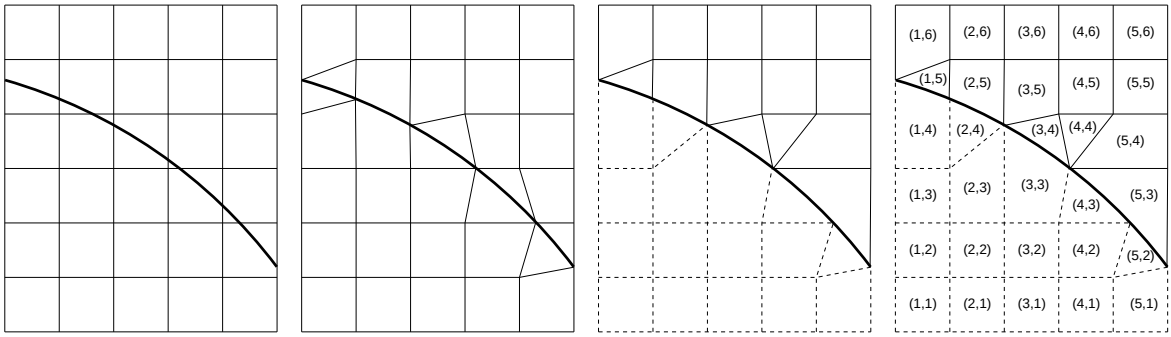

(a) (b) (c) (d)

Figure 5.1: Mesh adjustment algorithm: (a) Initial mesh and embedded boundary (thick line), (b) result of primary adjustment, (c) result of secondary adjustment (dashed lines indicate inactive cells), and (d) example of (i, j)-indexing on an adjusted mesh.

inside the interface and can be tagged as "inactive" since they are not used during the flow calculation. All cells that have not been deemed active or inactive are labelled as "unknown".

The first mesh-adjustment step involves identifying sharp corners in the interfaces. The unknown cell that contains each sharp corner is identified, and its nearest node is moved onto the corner. Once a node has been adjusted to lie on a boundary, it is tagged as "aligned". For the remaining "unknown" cells, the nodes nearest to the boundary are moved to the closest point of intersection between the interface and the mesh lines; this can be seen in figure 5.1(b). Again, nodes that have been moved are tagged as "aligned". This movement will leave cells that are bisected diagonally by the boundary. To account for this, the secondary step involves moving the nearest not-yet-aligned node of bisected cells so that it also lies on the boundary. This step will produce triangular cells, as seen in figure 5.1(c); these cells are simply treated as degenerate quadrilaterals with two coincident nodes. The final step in the mesh-adjustment algorithm involves using the same ray-tracing technique mentioned above to determine which of the "unknown" cells are "active" and which are "inactive". The resulting mesh remains structured and does not result in neighbouring cells of radically different sizes.

The present implementation allows for moving embedded boundaries whose motion can be prescribed either explicitly or through a level-set method [81, 82]. Boundary locations are computed at each time step and the mesh is readjusted. The velocity of the embedded boundary is accounted for during the flux calculation and the effect of the

rate-of-change of cell area is included as a source term (as seen in equation 5.1). To avoid excessive tangling, the mesh is first returned to an unadjusted state and then readjusted. Cells near the boundary will therefore change shape and previously active cells may become inactive, or vice versa. Solution content is supplied to newly activated cells and removed from newly deactivated cells through a redistribution algorithm designed to ensure conservation. The solution content of a newly deactivated cell is area-averaged into neighbouring active cells. The solution content of a newly activated cell is determined by taking the area-weighted average of the parts of the active cells from the previously adjusted mesh that intersect with the newly activated cell. A more detailed explanation of the mesh adjustment scheme and solution redistribution algorithm is provided in the papers by Sachdev and Groth [16, 17]. This redistribution algorithm is akin to the projection stage of a finite-volume scheme (determination of a cell-averaged solution).

5.2 Numerical Results

In order to verify and explore the potential of the proposed approach for predicting non-equilibrium micro-channel flows, several flow problems are now considered. The first such problem is subsonic boundary-layer flow over a flat plate as previously considered in chapter 4. The goal in this case is to demonstrate that the embedded boundary treatment and hyperbolic nature of the governing equations will yield smooth predictions of the frictional forces acting on the plate; traditional cut-cell-type approaches combined with the Navier-Stokes equations have been shown to produce large oscillations in viscous drag predictions [24]. Secondly, subsonic Couette flow will again be studied for a range of Knudsen numbers. The aim in this case is to show that the combination of the Gaussian closure with appropriate boundary conditions can describe the full range of flows from the well-known continuum regime at low Knudsen numbers, through the transition regime, and on to the free-molecular regime at high Knudsen numbers. It will also be demonstrated that the solution transition is equally well predicted by both a mesh that is aligned with the plates as with a mesh that is intersected at a 30° angle. Next, subsonic flow past a circular cylinder is again considered. As shown previously using body-fitted meshes, good agreement with experimental results has been achieved in the continuum and transition regimes [14], and it will be shown that equally good results can be achieved with the proposed embedded-boundary treatment. In order to show the ease with which complicated geometries including multiple stationary and moving embedded boundaries

can be treated, a micro-scale channel flow with complex moving geometry is considered for both continuum and non-equilibrium flows. A final demonstration of the capabilities of the proposed modelling and solution procedure is provided by a NACA0012 airfoil undergoing a prescribed oscillatory pitching motion. For this case, the treatment for embedded moving boundaries is combined with solution-directed adaptive mesh refinement, and comparisons are made with available experimental data. For all of the cases considered below, values for the mean free path, λ, used to define the Knudsen number were again determined using the expression for hard sphere collisional processes given by Bird [3], given in equation 4.46.

5.2.1 Subsonic Laminar Flat-Plate Boundary-Layer Flow

Subsonic boundary-layer air flow past a flat plate is re-considered. For this diatomic case, the free-stream Mach and Reynolds numbers are $\mathrm{Ma} = 0.2$ and $\mathrm{Re} = 2000$, respectively, and the Knudsen number is $1.5{\times}10^{-4}$, which indicates that the flow is laminar and in the continuum regime. Two computational meshes are considered: one aligned with, or at 0° to, the plate and a second mesh at 30° to the plate. Both meshes initially consist of one 16×16 Cartesian square block centred on the origin of the x and y axes. A boundary representing the flat plate is embedded in the block. This boundary is a line that is coincident with the x axis and passes through the origin. For $x < 0$, reflection (symmetry) boundary conditions are used, while for $x > 0$, solid-wall boundary conditions with full accommodation are used. In order to reduce the influence of the outflow boundary on the solution, the computational domain and plate stretch approximately twenty percent further than the length to be considered. The computational grid was then subjected to six or eight mesh refinements such that, at each level of refinement, any block crossed by the boundary was refined. The result was a mesh comprising 376 blocks and $48,128$ active cells for the zero-degree case and 508 blocks and $65,024$ active cells for the thirty-degree case when six levels of refinement were used. For eight levels of refinement, 764 active blocks and $195,584$ active cells for the zero-degree case and 1271 active blocks and $276,992$ active cells for the thirty-degree were used. A section of the mesh for each case can be seen in figure 5.2. The larger number of cells in the non-aligned case is a result of the fact that, at thirty degrees, the interface crosses more blocks, which will be flagged for refinement; the smallest cells are the same size for both angles.

Numerical predictions of the friction coefficient, C_f, are shown in figure 5.3. As in

chapter 4, comparisons are again made to the classical boundary layer results of Blasius [69]. It can be seen that the computed results and the Blasius solution show good agreement. It is important to note that there are no oscillations present in the skin-friction coefficient, even when the flat plate intersects the grid at an angle. The same two cases were also run with eight levels of mesh refinement. For this refined case, a close-up view of the plot at the center of the plate is shown. It can be seen that, with refinement, the Blasius solution is recovered quite well.

The smooth results of the Gaussian closure are in contrast with previous results obtained by Sachdev and Groth using the Navier-Stokes equations [16, 17]. Figure 5.4(a) shows typical results for predictions of skin-friction coefficients for flow past a flat plate angled at 30° to the grid. The same mesh adjustment scheme is used. The oscillations present in this figure are due to the necessity of evaluating second derivatives for the solution of the Navier-Stokes equations; these higher-order derivatives are more sensitive to the grid irregularities caused by the embedded boundary. It can be seen in figure 5.4(b) that the oscillations in the predicted coefficient of friction are related to the local modifications to the mesh caused by the embedded boundary. There is a jump in the prediction whenever the row of cells that is intersected by the boundary changes. Similar oscillations in the predicted skin-friction coefficients, with even larger and far more deleterious excursions, were observed in the AMR solutions of Coirier [24] and Coirier and Powell [25] using a cut-cell approach, which can produce meshes with large differences in adjacent cell sizes.

Grid convergence behaviour is demonstrated in figure 5.5. Here solutions to the same boundary-layer situation have been computed on sequences of meshes that were constructed either with uniform resolution or with AMR and with a plate embedded at either zero or thirty degrees to the grid. The coefficient of drag has then been computed from the predicted skin friction profile. It can be seen that each sequence is converging to the same value, however this value is less than the coefficient of drag of 0.0297 predicted by the Blasius approximation. This is because the Blasius solution is an approximate solution for incompressible flow, whereas the Gaussian closure accounts for compressibility effects. Also, the Blasius solution predicts a coefficient of friction which reaches infinity at the leading edge. Therefore, even though the solutions to the moment equations agree well with the Blasius solution further along the plate, they predict a lower drag near the leading-edge. In fact, it cannot be expected that these computations will converge exactly to any approximate analytic solution to the Navier-Stokes equations simply because

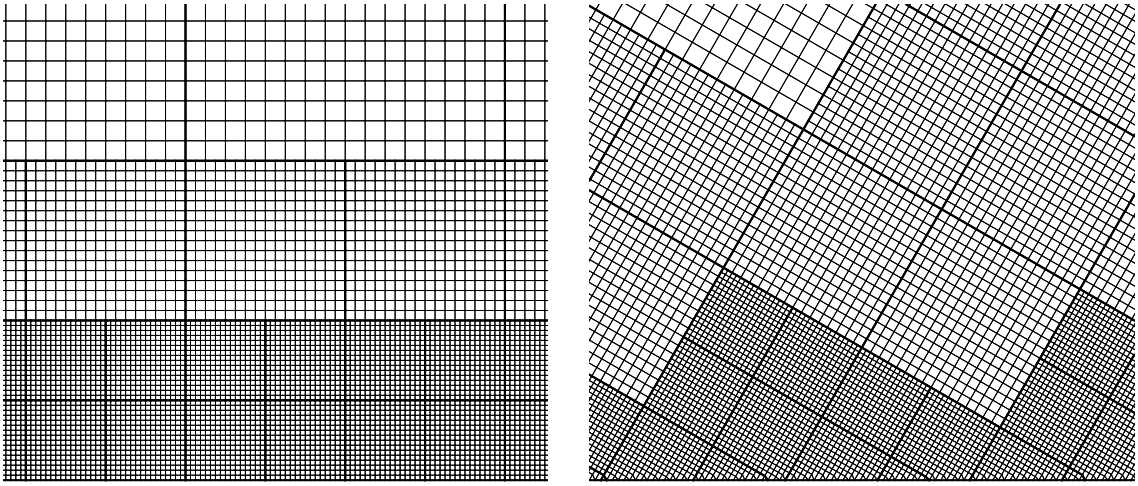

(a) (b)

Figure 5.2: (a) Section of 48, 128-cell embedded-boundary mesh with flat plate embedded at 0°. (b) Section of 65, 024-cell embedded-boundary mesh with flat plate embedded at 30°.

the governing equations are different. Figure 5.5 also provides a good illustration of the computational advantages provided by adaptive mesh refinement. It can be seen that the solutions obtained using AMR provide a given accuracy using only a fraction of the cells used in a uniform-mesh computation. Obviously in this situation a stretched mesh that concentrates cells near the boundary could obtain similar results to the AMR, however in more complicated situation it is not always clear where spacial resolution is needed. Also, if boundaries are moving or evolving during a simulation, areas requiring increased resolution will move; adaptive mesh refinement is especially useful in these situations.

5.2.2 Subsonic Laminar Couette Flow

The second problem considered is the one of Couette flow for a gas spanning a variety of flow regimes. The current investigation comprises two infinite-span plates separated by a fluid-filled gap that are translating in opposite directions with a speed of $u_p = 30$ m/s. The gap between the plates is filled with argon at a temperature of $T = 288$ K and standard pressure; the diatomic extension to the moment closure is therefore not used for this case. Again, two embedded meshes are considered, one aligned at 0° to the plates and one at 30° to the plates. The original mesh comprised 10, 240 cells, however many

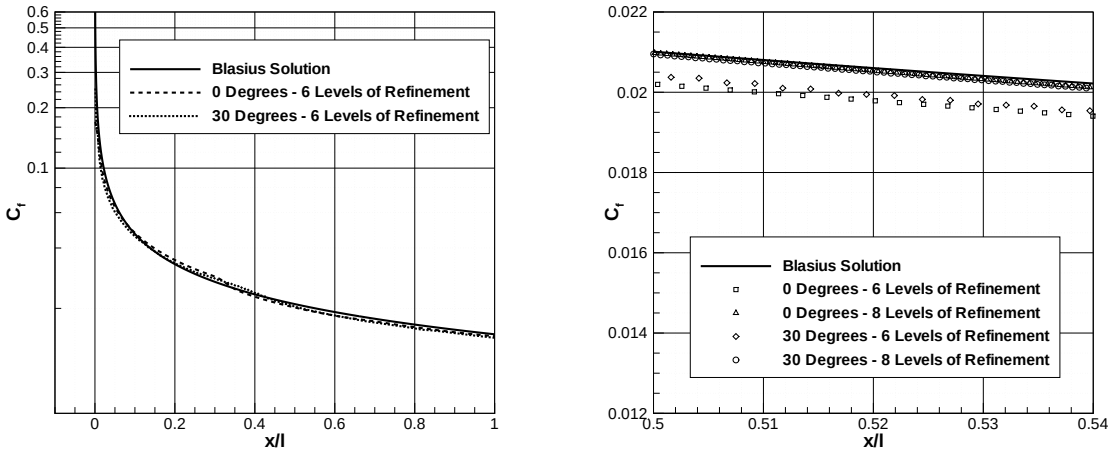

Figure 5.3: Coefficient of friction calculated for a Cartesian grid with an embedded flat plate at 0° and 30° to the grid as compared to Blasius solution; full and close-up views.

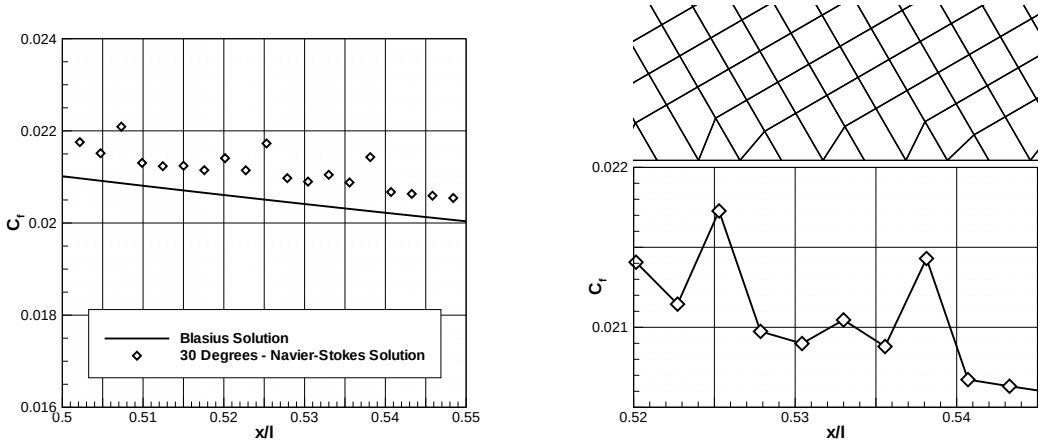

(a) (b)

Figure 5.4: (a) Coefficient of friction calculated for a Cartesian grid with an embedded flat plate at 30° to the grid using the Navier-Stokes equations. (b) Relation between oscillations in predicted coefficients of friction and local modifications to the mes caused by the embedded boundary.

of these cells were inactive. The number of active cells for all of the 0° computations was 2,560 and there were 2,956 active cells for the 30° situations; the active portions of these grids can be seen in figure 5.6. Boundary conditions for the solid walls were applied

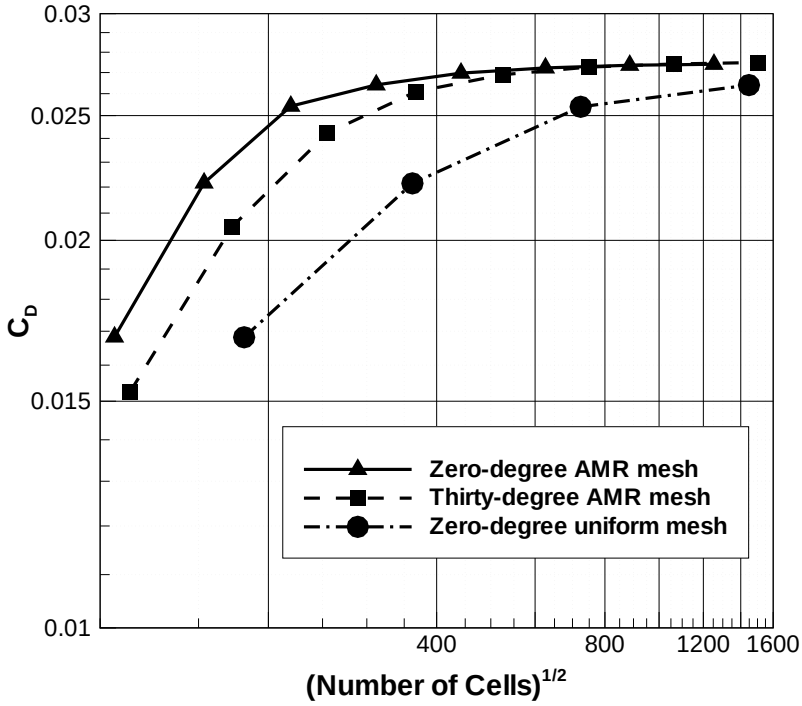

Figure 5.5: Coefficient of drag calculated using various Cartesian grids with an embedded flat plate at 0° and 30° to the grid, each of which was constructed using either with uniform resolution or AMR.

as described above. At the remaining two boundaries, velocity and shear pressure were extrapolated while all other flow properties where held fixed.

Figure 5.7 shows both the predicted normalized flow velocity at the wall, u/u_p, and normalized shear stress, $\tau_{xy}/\rho u_p\sqrt{2kT/\pi m}$ for the Couette flow problem as a function of Knudsen number. Values for the fluid velocity at the wall shown in figure 5.7 were evaluated by taking the average along each plate and values for the fluid shear were evaluated by taking the average over the entire domain. The results show that the Gaussian closure, combined with the Knudsen-layer analysis for the solid boundary, is able to reproduce the correct solutions in both the the continuum (Navier-Stokes) regime, where there is no slip between the fluid and the wall, and free-molecular regime, where there is perfect slip. In addition, it provides solutions that effectively transition from the continuum result to the free-molecular-flow solution in a manner that is in very good agreement with an approximate analytical solution developed by Lees [68]. Lastly, the

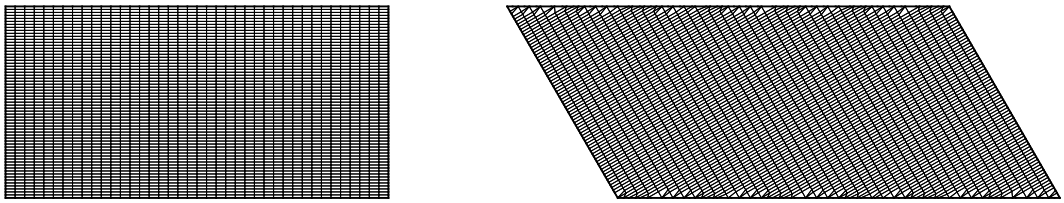

(a) (b)

Figure 5.6: (a) 2,560-cell mesh with plates embedded at 0°. (b) 2,956-cell mesh with plates embedded at 30°.

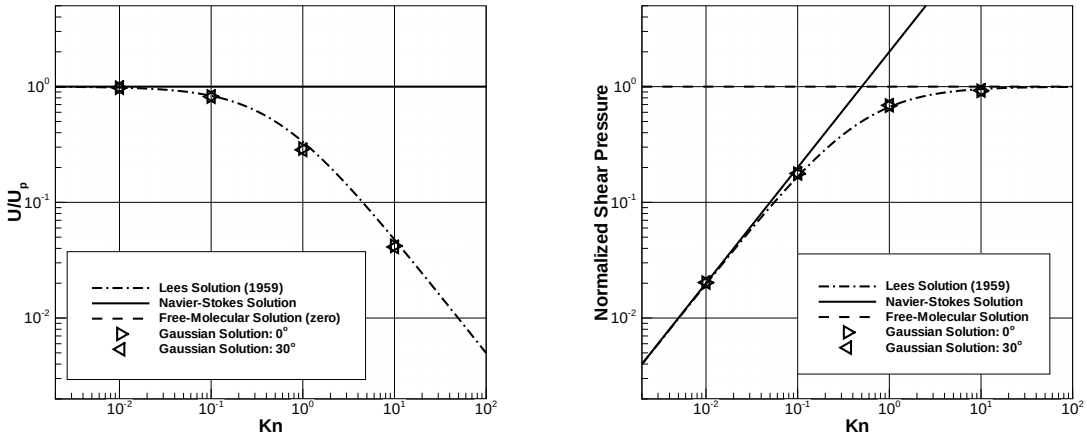

(a) (b)

Figure 5.7: (a) Predicted values of the normalized velocity at plate wall and (b) normalized shear pressure as a function of Knudsen number for planar subsonic laminar Couette flow of argon between parallel diffusely reflecting plates; $u_p = 30$ m/s, $T = 288$ K.

numerical predictions are essentially independent of the computational mesh used and further demonstrate the high numerical accuracy that can be achieved using the Gaussian closure coupled with the embedded-mesh algorithm.

5.2.3 Subsonic Laminar Flow Past a Circular Cylinder

Subsonic air flow past an circular cylinder is considered next. In order to demonstrate that the present embedded-mesh treatment can recover the drag results for the circular cylinder described above with virtually equal accuracy to those obtained with a body-

fitted mesh (shown in section 4.5.6), values for the coefficient of drag were re-computed using the Gaussian closure and embedded mesh approach for a range of Knudsen numbers with speed ratios of 0.027 and 0.107. All computations were again conducted on a square-shaped Cartesian mesh that initially contained one 16×16 block with an embedded circular cylinder. For most cases, the square domain had a dimension that was 125 times the cylinder radius. This mesh was then refined ten times in order to capture the boundary, resulting in a mesh of 556 blocks and 112,936 active cells, as seen in figure 5.8. As the Knudsen number increases, the distance to which the flow is disturbed by the boundary interactions also increases. Thus, in order to eliminate the effects of the far-field boundary on the solution, the size of the initial block had to be enlarged for the $\mathrm{Kn} = 0.5$ and $\mathrm{Kn} = 1$ cases; additional levels of mesh refinement were then used in order to preserve the resolution of the inner boundary.

The computed coefficients of drag are shown in figure 5.8. The embedded mesh results are compared the Gaussian-closure solutions obtained using a body-fitted mesh, as well as to the experimental results collected by Coudeville *et al.* [74]. It is quite apparent that agreement between the experimental results and the values predicted by the Gaussian closure are equally good when the embedded boundary treatment is used.

5.2.4 Channel Flow with Moving Boundaries

In previous work, Coirier explored Mach 0.1 air flow through a branched channel containing fourteen pin cooling fins using a Cartesian-cut-cell approach [24]. A similar case is considered here, except two rows of the pins are now assumed to oscillate with a prescribed motion. The aim of this case is to show how easily the current embedded-boundary treatment can be used for cases with numerous embedded boundaries, some of which are moving with respect to the frame of reference of the computational mesh. Coirier designed the geometry of the problem so as to loosely model the flow within turbine blades. It involves a channel through which fully developed flow enters. This channel contains a branch and three rows of cooling pins. The flow resistance caused by the pins causes some of the flow to be redirected though the secondary channel. An added characteristic of the current situation is that two of the rows of pins move through a prescribed oscillation. The computational grid used for this situation is shown in figure 5.9. A close-up view of the area surrounding the cooling pins at three different times is shown in figure 5.10. This figure shows the initial position as well as the extremes of

the pin oscillations. Two Knudsen numbers (based on pin diameter) were considered for this case: $\mathrm{Kn} = 7 \times 10^{-6}$ (continuum regime) and $\mathrm{Kn} = 7 \times 10^{-2}$ (transition regime). For both cases, the simulation was originally run to steady state with the pins held stationary. For the continuum-regime situation, this steady state solution was in good qualitative agreement with Coirier's results and showed similar velocity contours and recirculation regions. Once steady state had been achieved, the pins were set into oscillations described by the function $\delta x = \pm \Delta x \sin(2\pi f t)$, where δx is the pin displacement, Δx is the maximum displacement, t is the time and, $f = 100$ s^{-1} is the frequency. The CFL restriction on the time step for this explicit scheme ensured that a very large number of iterations was required for each period of the pin oscillations.

Figures 5.11 and 5.12 show the predicted contours of the x-direction velocity component for the above situation for $\mathrm{Kn} = 7 \times 10^{-6}$ and $\mathrm{Kn} = 7 \times 10^{-2}$, respectively. In each figure, the results in the top half of figure show the predicted solutions after 10 ms (one period) while the results in the bottom half depict the solutions after 15 ms (one and a half periods). The geometry at both presented times is identical, however at $t = 10$ ms, the two outside rows of pins are approaching the center row while at $t = 15$ ms the outside rows are moving further apart. The differences in the plots indicates that there is some level of hysteresis. It can also be noted that in the transition-regime case, the hysteresis as well as the general effects of the pins on the flow appears to be reduced. This should be expected since, in higher-Knudsen number cases such as this, the reduced frequency of collisions leads to a flow that is mostly dependent on the projected area of the cooling pins; something which does not change throughout the simulation.

5.2.5 Oscillating NACA0012 Airfoil

The final problem considered is that of a NACA0012 airfoil undergoing a prescribed oscillation in a background airflow. The specific problem selected is one studied experimentally by Landon [83] as part of a study of flow conditions for helicopter blades. Here a NACA0012 airfoil undergoes an oscillation about its quarter cord with angle of attack prescribed by the function $\alpha(t) = \alpha_0 + \alpha_m \sin(2\pi f t)$ where $\alpha_0 = 0.015°$, $\alpha_m = 2.51°$ and $f = 62.5\mathrm{s}^{-1}$. The Reynolds number based on chord length is $\mathrm{Re} = 5.5 \times 10^6$ and the Mach number is 0.775. The flow conditions surrounding the airfoil should therefore be turbulent, however there is, as yet, no method for the treatment of turbulence in the 10-moment model. Also, in order to avoid using the number of cells required to predict

a boundary layer at such a high Reynolds number, the solid-wall accommodation coefficient is set to zero for this case. This is equivalent to assuming fully specular reflection at the boundary and will lead to an inviscid, Euler-like, near-equilibrium, solution using the Gaussian model. The Knudsen number for this flow is 6.3×10^{-7}. This flow situation is therefore firmly in the continuum regime. This study is included to show both that the moment equations can reliably predict traditional continuum-regime flows and that the AMR and mesh-adjustment schemes can be used for the solution of practical unsteady problems.

Here, the NACA0012 airfoil is embedded in an O-type grid with the far-field boundary located sixteen chord lengths out from the quarter chord of the airfoil. This mesh originally consisted of two four-by-eight blocks, as shown in figure 5.13(a). This mesh was then refined uniformly twice so as to produce a thirty-two-block initial grid (figure 5.13(b)). A regiment of grid sequencing was then employed during which steady-state solutions for flow past the stationary airfoil were sought on sequentially finer meshes leading to a final mesh with eight refinement levels. Successive meshes were obtained either through refinement of every block lying within a bounding box surrounding the airfoil or through solution-directed refinement using the divergence of the velocity field as the refinement criterion (blocks containing areas where this value is high were flagged for refinement and blocks containing areas where this value is very low were flagged for possible coarsening). This criterion has been found to identify shocks effectively. The eight-level mesh resulting from the grid sequencing comprised 3023 blocks and 96, 736 cells, of these cells 46, 797 were internal to the airfoil and therefore inactive.

The mesh resulting from and steady-state solution from the previously-described grid-sequencing routine was used as the starting point for the time-accurate oscillatory study. For this simulation, adaptive mesh refinement was carried out every fifty time steps as this was found to be frequent enough to allow the grid to track changes in the flow solution effectively.

The adjusted grid and computed thermodynamic pressure contours are shown in figure 5.14. This figure shows the initial, steady-state solution as well as the solution after 36 and 44 ms (first and third quarter of the third period). Once again, the CFL restriction ensured that a very large number of time steps was taken for each period. It can be observed that as the airfoil pitches up, the shock on the upper surface strengthens and moves towards the trailing edge while the shock on the lower surface weakens and eventually disappears entirely. As the airfoil pitches down, the opposite is true. The effec-

tiveness with which the adaptive mesh refinement tracks the movement of the shocks can also be plainly seen in figure 5.14. The scheme effectively concentrates blocks, and thus computational cells, along the discontinuity. It is observed that, during the oscillation, there is a hysteresis in the shock position as the airfoil passes the symmetric situation. This hysteresis is reflected in the calculated coefficient of normal force, as seen in the bottom right panel of figure 5.14. In this figure the computed normal force coefficient moves from the near-symmetric steady-state initial solution to a periodic motion which is in good agreement with the experimental results of Landon [83] and similar to those obtained by Sachdev and Groth [16, 17].

5.3 Observations

The potential for the use of moment closures combined with a treatment of embedded boundaries for tackling continuum- and transition-regime flows has been demonstrated. The proposed approach allows for a non-Cartesian grid to undergo local adjustments such that it is aligned with arbitrary boundaries. Sharp corners in the interface can be accurately represented and very small cells, typical of traditional cut-cell approaches, are not created. The purely hyperbolic nature of moment equations allows for accurate treatment of micro-scale flows and gives solutions that are not strongly affected by the grid irregularities caused by the mesh adjustment.

The proposed approach has been verified through application to a number of representative, two-dimensional flow problems. It has been demonstrated that the hyperbolic nature of moment closures allows for smooth predictions of viscous effects along embedded boundaries when similar treatments applied to the Navier-Stokes equations yield oscillatory results.

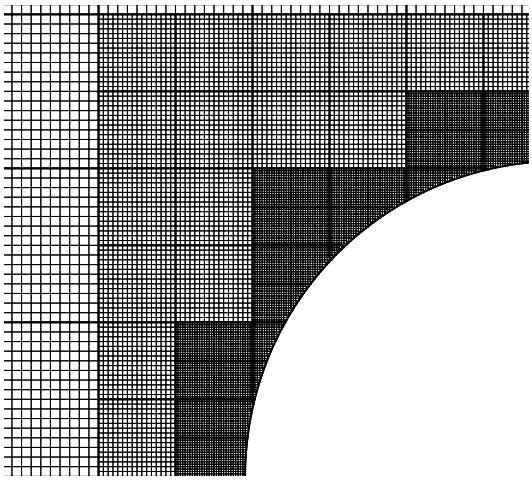

(a)

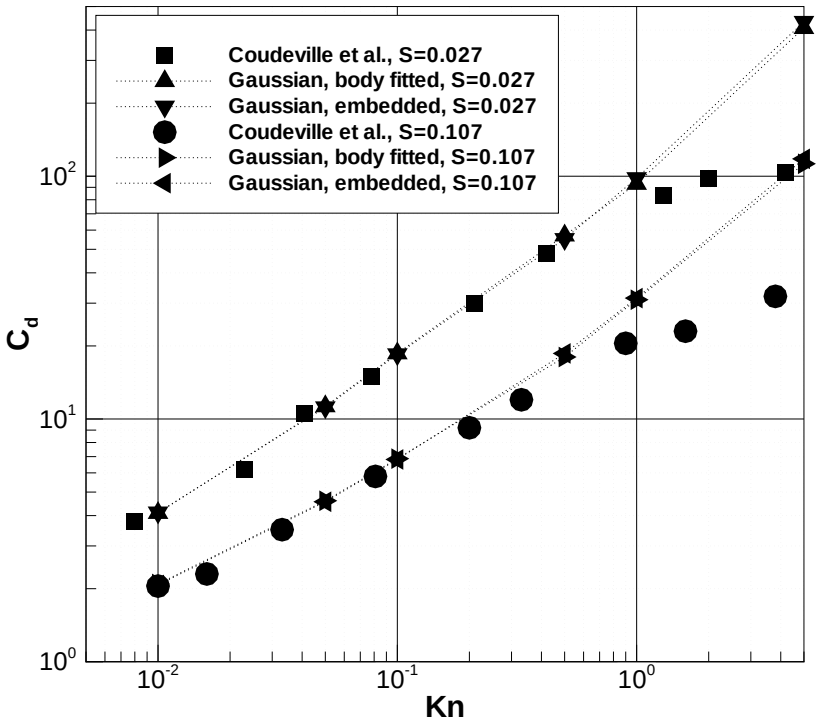

(b)

Figure 5.8: (a) Section of embedded-boundary grid used for cylinder calculations. (b) Coefficients of drag computed using the Gaussian closure with a body-fitted mesh and a Cartesian mesh with an embedded boundary at speed ratios of 0.027 and 0.107 are compared with experimental results.

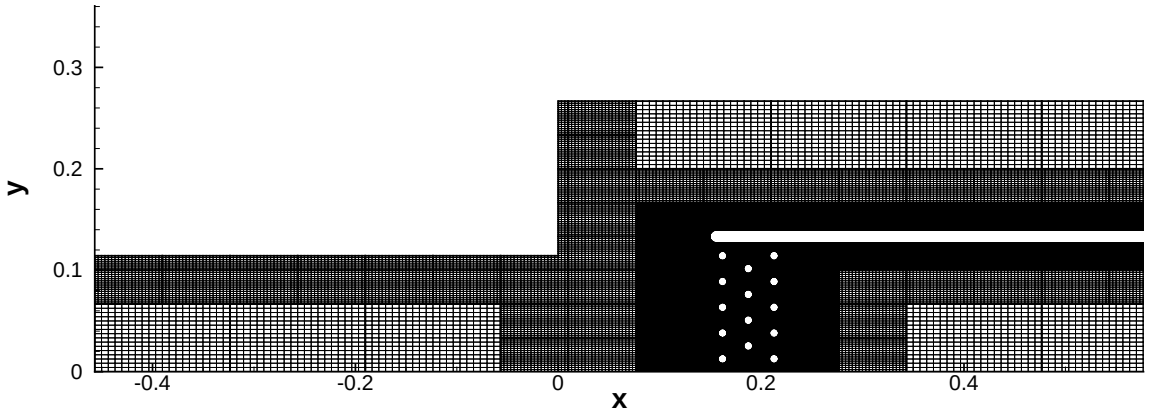

Figure 5.9: Computational grid used in embedded-boundary branched-duct simulation.

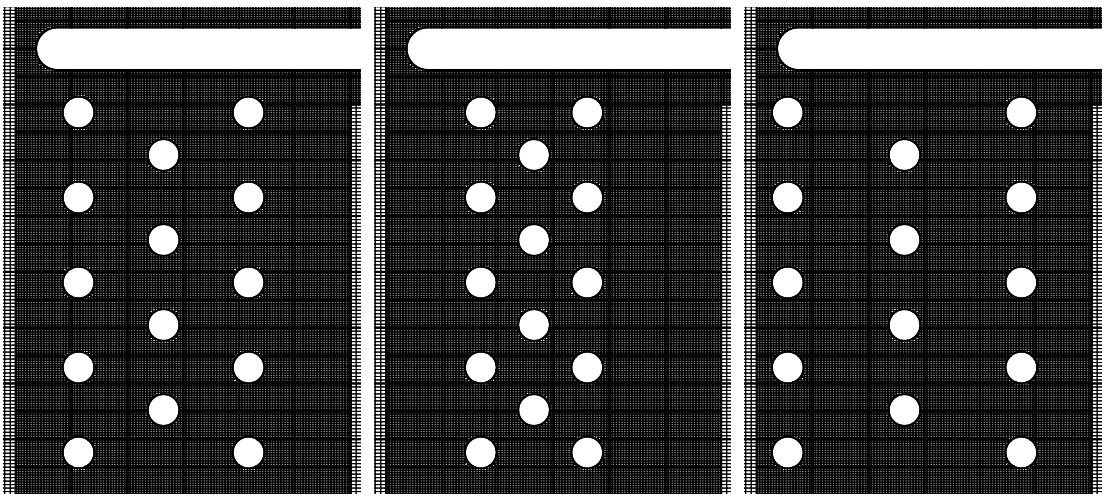

Figure 5.10: Close-up view of computational mesh around cooling pins for the branched-duct simulation at three different instances in time during their sinusoidal motion.

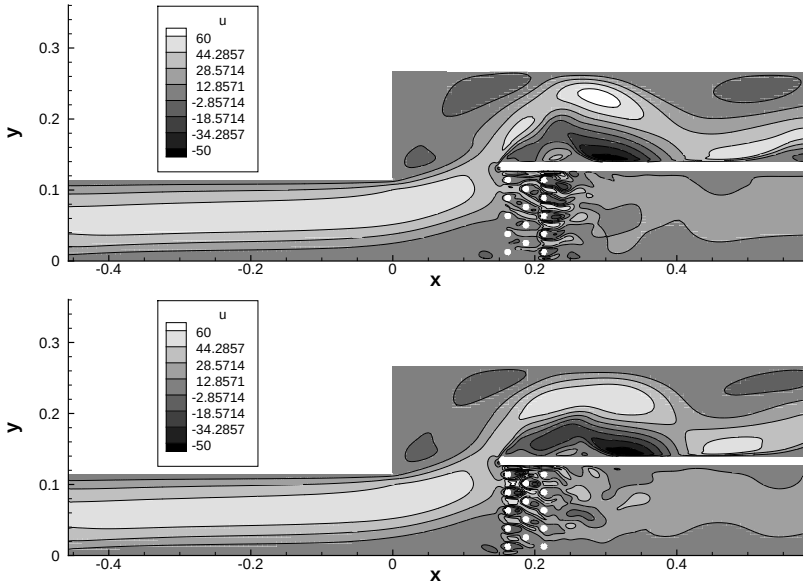

Figure 5.11: Shaded contours of the x-direction component of velocity for the branched channel simulation: $\mathrm{Kn} = 7 \times 10^{-6}$ simulation with result for $t = 10$ ms on the top and $t = 15$ ms on the bottom.

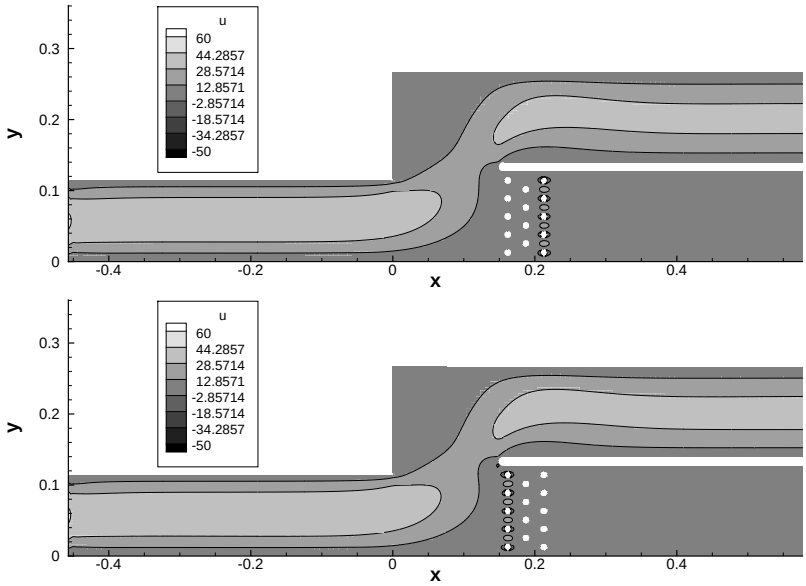

Figure 5.12: Shaded contours of the x-direction component of velocity for the branched channel simulation: $\mathrm{Kn} = 7 \times 10^{-2}$ simulation with result for $t = 10$ ms on the top and $t = 15$ ms on the bottom.

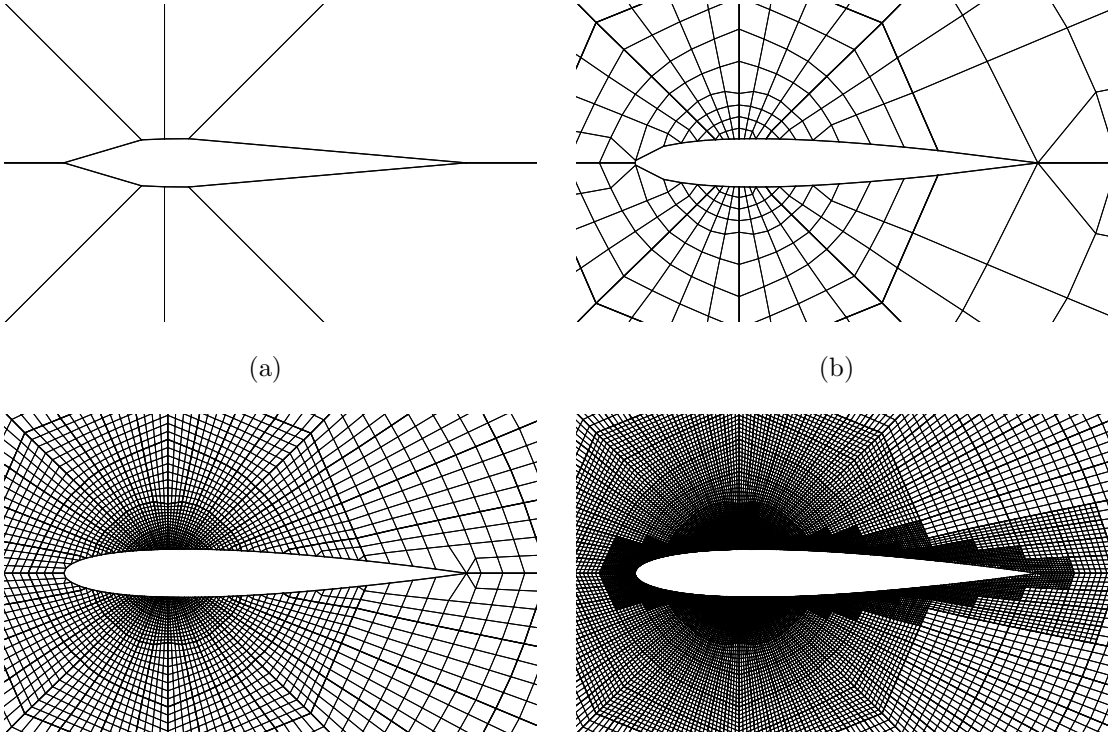

Figure 5.13: Section of computational mesh with embedded NACA0012 boundary shown at various states of construction: (a) initial two-block mesh, (b) mesh with thirty-two blocks resulting from two levels of mesh refinements, (c) mesh with 332 blocks resulting from five levels of mesh refinements, (d) mesh with 2921 blocks resulting from eight levels of mesh refinements

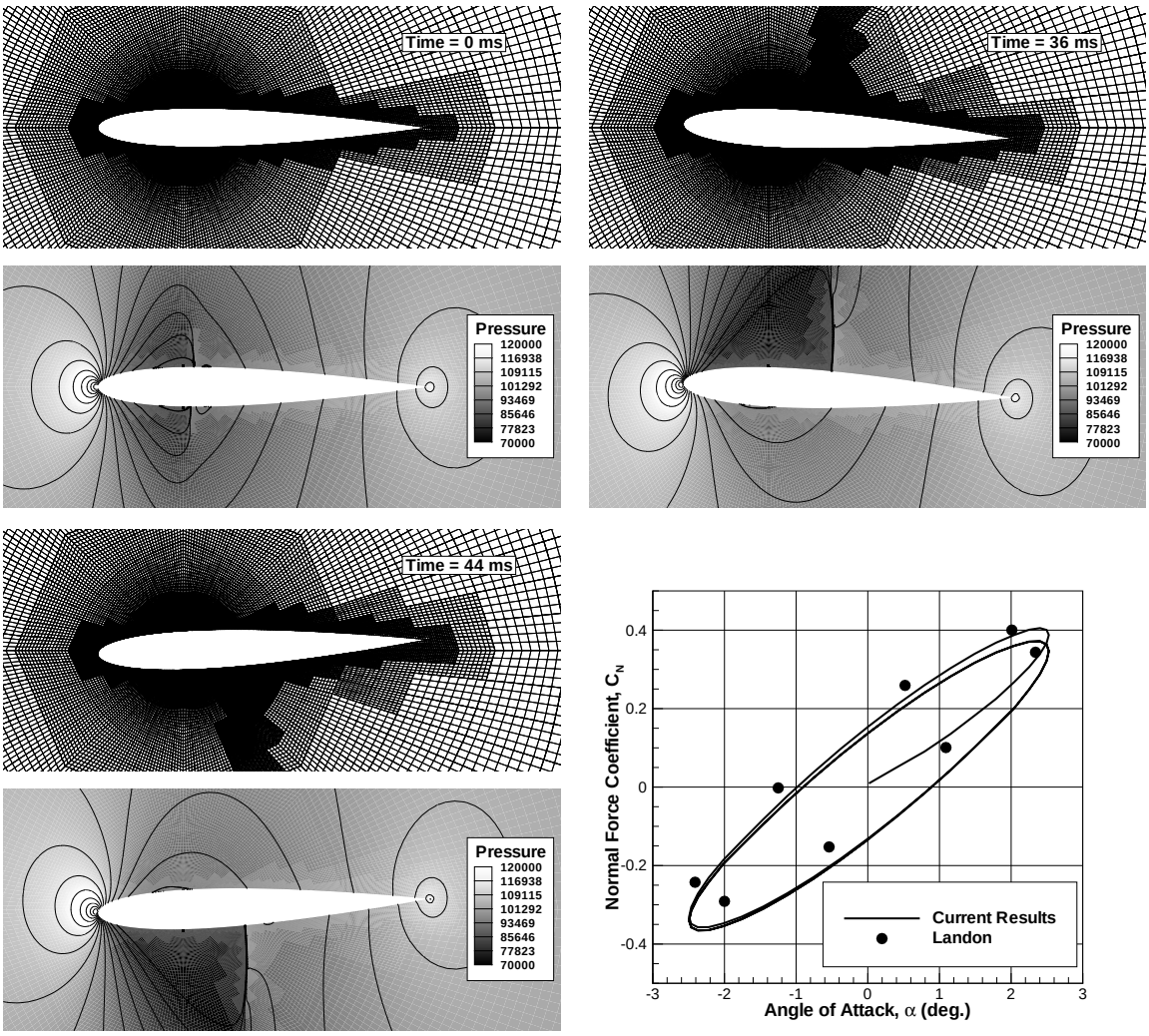

Figure 5.14: Computational grids and thermodynamic pressure contour plots for initial, steady state solution and solution after 36 and 44 ms as well as comparison of computed normal force coefficient for varying angle of attack and previous experimental results of Landon.

Chapter 6

Regularized Gaussian Moment Closure

As has been demonstrated in chapters 4 and 5, the Gaussian moment closure offers a robust set of hyperbolic moment equations for the prediction of viscous fluid flow across a wide range of flow regimes. It is, however, deficient in that it cannot account for heat-transfer effects. Recently, Stuchtrup and Torrilhon [21] have shown a technique for the regularization of moment equations and have applied this to the 13-moment equations from the Grad hierarchy. In essence, this technique consists of creating an expansion about the moment equations, thus allowing small deviations from the assumed distribution function. A required assumption for this procedure is that deviations from the assumed distribution function are suppressed by inter-molecular collisions more quickly than non-equilibrium effects contained in the original moment equations. In this chapter, a similar regularization technique is applied to the Gaussian closure. This procedure results in the addition of elliptic terms to the standard equations of the Gaussian closure. The resulting terms lead to a heat-transfer treatment which is dependent on the anisotropic pressure tensor. It is shown that the elliptic nature of the added terms leads to smooth (regularized) solutions.

The following section will describe the derivation of the present correction to the Gaussian equations. This is done both by expansion about the moment equations (this is the technique used by Struchtrup and Torrilhon), and also by explicitly taking an expansion around the assumed form of the distribution function in the kinetic equation. It is shown that both techniques yield identical results. Following these derivations, the application of a finite-volume scheme to the solution of the resulting equations is detailed.

Numerical results for a range of canonical continuum and micro-scale flow problems are then explored, including shock structure, Couette flow, and flow past a circular cylinder, as well as transonic flow past a micro airfoil. Comparisons with analytic, experimental, and direct-simulation Monte Carlo (DSMC) results are also made and demonstrate the capabilities of the proposed non-equilibrium model. Finally, some thoughts regarding the applicability of these equations to practical micro-scale applications are explored.

6.0.1 The Collision Operator

As stated earlier, the collision operator present in equations 2.8 and 2.18 is difficult or impossible to evaluate. Fortunately, for many engineering problems, approximate collision terms prove adequate. The most commonly used approximation is the BGK collision operator [36]. This operator can be written as

$$\frac{\delta \mathcal{F}}{\delta t} = -\frac{\mathcal{F} - \mathcal{M}}{\tau}\,. \tag{6.1}$$

In previous chapters, this collision operator has proven adequate for the Gaussian moment equations in the situations considered. However, the subject of the current chapter is the addition of heat-transfer modelling to the 10-moment equations and this simple collision operator is no longer sufficient. A well-known limitation of the BGK model is that it always yields a Prandtl number of

$$\frac{2}{5}\frac{\gamma}{\gamma - 1} = \begin{cases} 1 & \text{for monatomic gases, and} \\ 1.4 & \text{for diatomic gases.} \end{cases}$$

This is in contradiction with physical Prandtl numbers for most gases, which tend to be less than one.

There are several other collision-operator models available which can provide more realistic Prandtl numbers. In the present work, an approximate collision term proposed by Holway [48] will be used to describe collisional processes for monatomic gases. This model, often referred to the ellipsoidal statistical model, preserves much of the simplicity of the BGK model, while allowing for a tunable Prandtl number. It can be written as

$$\frac{\delta \mathcal{F}}{\delta t} = -\frac{\mathcal{F} - \mathcal{G}_{ES}}{\tau_{ES}}\,, \tag{6.2}$$

where

$$\mathcal{G}_{ES}(x_i, v_i, t) = \frac{\rho}{m(2\pi)^{3/2}(\det T_{\alpha\beta})^{1/2}} \exp\left(-\frac{1}{2} T^{-1}_{ij} c_i c_j\right)\,. \tag{6.3}$$

Again, m is the gas particle mass and ρ is the mass density. In fact, this distribution is a Gaussian distribution function with a modified pressure tensor. The tensor T_{ij} is defined as

$$T_{ij} = (1-\nu)RT\delta_{ij} + \nu\Theta_{ij}\,, \tag{6.4}$$

where Θ_{ij} is again a symmetric 'temperature' tensor given by $\Theta_{ij} = P_{ij}/\rho$. If the parameters τ_{ES} and ν are chosen such that $(1-\nu)\mu = \tau_{ES}p$ and $(1-\nu)\mathrm{Pr} = 1$ the model will predict the correct values for fluid viscosity and thermal conductivity in the continuum limit. The ellipsoidal statistical collision model's adherence to Boltzmann's H theorem was only recently demonstrated by Andries and Perthame [84] and only for monatomic gases. It is important to note that the relaxation times for these two models (τ and τ_{ES}) differ by a factor of the Prandtl number, and the moment equations which follow will be written in terms of the relaxation time for the standard BGK model for consistency with previous chapters and traditional forms of these equations.

6.1 Extended Fluid Treatment for Thermal-Diffusion Effects

As stated several times, one of the major shortfalls of the Gaussian closure is its inability to account for thermal diffusion. This is due to the construction of the assumed form of the distribution function used to obtain moment closure. By allowing small deviations from the Gaussian distribution, however, thermal diffusion can be re-introduced into the moment equations. This can be done by taking an appropriate Chapman-Enskog perturbative expansion of either the moment equations (equations. 4.1-4.3) or the kinetic equation using the Gaussian distribution as the base distribution. Both of these techniques are detailed here.

6.1.1 Perturbative Expansion About the Moment Equations

The perturbative expansion technique applied to the moment equations is considered first. A similar technique was previously used by Struchtrup and Torrilhon in the regularization of the 13-moment equations [21]. For this expansion, it is convenient to define the tensor

$$K_{ijkl} = m\left\langle c_i c_j c_k c_l \mathcal{F}\right\rangle - m\left\langle c_i c_j c_k c_l \mathcal{G}\right\rangle = m\left\langle c_i c_j c_k c_l \mathcal{F}\right\rangle - \frac{1}{\rho}\left[P_{ij}P_{kl} + P_{ik}P_{jl} + P_{il}P_{jk}\right] . \tag{6.5}$$

This quantity is the deviation of the fourth random-velocity moment from that calculated using a Gaussian distribution. The general moment quantities are then re-written as a perturbative expansion about their values as predicted by the Gaussian closure. This is done by introducing a formal smallness or perturbation parameter, ϵ, which is used to scale the solution and moment equations. For example, the scaled solution for the generalized heat flux, Q_{ijk}, and previously defined fourth-order tensors are written as

$$Q_{ijk} = Q_{ijk}^{(\mathcal{G})} + \epsilon Q_{ijk}^{(1)} + \epsilon^2 Q_{ijk}^{(2)} + \epsilon^3 Q_{ijk}^{(3)} + \cdots , \tag{6.6}$$

and

$$K_{ijkl} = K_{ijkl}^{(\mathcal{G})} + \epsilon K_{ijkl}^{(1)} + \epsilon^2 K_{ijkl}^{(2)} + \epsilon^3 K_{ijkl}^{(3)} + \cdots . \tag{6.7}$$

Here, the superscript $(\mathcal{G})$ denotes the value for a moment calculated using a Gaussian distribution function and the superscript (n) denotes the nth order correction. The moment equation for the moment $\langle c_i c_j \mathcal{F}\rangle$ using the ellipsoidal statistical collision model (without using an assumed form for the distribution function) is

$$\frac{\partial P_{ij}}{\partial t} + \frac{\partial}{\partial x_k}(u_k P_{ij}) + P_{jk}\frac{\partial u_i}{\partial x_k} + P_{ik}\frac{\partial u_j}{\partial x_k} + \frac{\partial Q_{ijk}}{\partial x_k} = -\frac{1}{\tau}\Big(P_{ij} - \frac{1}{3}P_{kk}\delta_{ij}\Big) . \tag{6.8}$$

It can be seen that for this general case, there is a term, $\frac{\partial Q_{ijk}}{\partial x_k}$, that is not present in equation 4.3. Setting this third-order tensor to be effectively zero is how closure was obtained in the Gaussian model. However, in the current technique, a non-zero first-order deviation, *i.e.*, $Q_{ijk}^{(1)}$, is introduced. For small deviations from the Gaussian closure, an approximation to this term can be determined by writing the scaled moment equation for Q_{ijk}, which, again using the approximate relaxation-time collision term of Holway [48], can be written for a monatomic gas as

$$\begin{aligned}&\frac{\partial Q_{ijk}}{\partial t} + \frac{\partial}{\partial x_l}\left(u_l Q_{ijk}\right) + Q_{jkl}\frac{\partial u_i}{\partial x_l} + Q_{ikl}\frac{\partial u_j}{\partial x_l} + Q_{ijl}\frac{\partial u_k}{\partial x_l} \\ &+P_{kl}\frac{\partial}{\partial x_l}\left(\frac{P_{ij}}{\rho}\right) + P_{jl}\frac{\partial}{\partial x_l}\left(\frac{P_{ik}}{\rho}\right) + P_{il}\frac{\partial}{\partial x_l}\left(\frac{P_{jk}}{\rho}\right) + \frac{\partial K_{ijkl}}{\partial x_l} = -\frac{\mathrm{Pr}}{\epsilon\tau}Q_{ijk} .\end{aligned} \tag{6.9}$$

Note that, in the expression above, equation 6.5 has been used and the scaling parameter, ϵ, has been explicitly introduced on the right-hand side. The small parameter ϵ is introduced in accordance with the assumption that deviations of the moment quantities

from those predicted by the Gaussian closure (*i.e.*, $Q_{ijk} = 0$) will be attenuated rapidly by collisional processes. By making use of equations 6.6 and 6.7, it can be seen that the unscaled zeroth-order terms of equation 6.9 yields

$$Q_{ijk}^{(\mathcal{G})} = 0\,, \tag{6.10}$$

in agreement with the Gaussian closure. The equation allowing for unscaled first-order deviations becomes

$$Q_{ijk}^{(1)} = -\frac{\tau}{\mathrm{Pr}}\left[P_{kl}\frac{\partial}{\partial x_l}\left(\frac{P_{ij}}{\rho}\right) + P_{jl}\frac{\partial}{\partial x_l}\left(\frac{P_{ik}}{\rho}\right) + P_{il}\frac{\partial}{\partial x_l}\left(\frac{P_{jk}}{\rho}\right)\right]. \tag{6.11}$$

This is the correction which will be used herein to introduce thermal diffusion to the Gaussian equations.

6.1.2 Perturbative Expansion About the Kinetic Equation

The above derivation was based on an expansion about the moment equations. The same result can also be obtained from an expansion about the kinetic equation with the ellipsoidal statistical collision model of Holway [48]. To do this, it is convenient to write the collision operator in a slightly different form. This is done by first assuming $(1-\nu) = \epsilon \ll 1$ and rewriting the expression for the tensor T_{ij} as

$$\begin{aligned} T_{ij} &= (1-\nu)RT\delta_{ij} + \nu\Theta_{ij} \\ &= \epsilon RT\delta_{ij} + (1-\epsilon)\Theta_{ij} \\ &= \Theta_{ij} + \epsilon\left[RT\delta_{ij} - \Theta_{ij}\right] \\ &= \Theta_{i\alpha}\left[\delta_{\alpha j} - \epsilon\Lambda_{\alpha j}\right], \end{aligned} \tag{6.12}$$

where $\Theta_{i\alpha}\Lambda_{\alpha j} = [RT\delta_{ij} - \Theta_{ij}]$. It can be seen in equation 6.3 that T_{ij}^{-1} is needed. This can be written as

$$T_{ij}^{-1} = \left[\delta_{i\alpha} - \epsilon\Lambda_{i\alpha}\right]^{-1}\Theta_{\alpha j}^{-1}\,. \tag{6.13}$$

Provided the spectral radius of $\epsilon\Lambda_{i\alpha}$ is less than unity, a fact that is true given the assumption of the smallness of ϵ, the term $\left[\delta_{i\alpha} - \epsilon\Lambda_{i\alpha}\right]^{-1}$ can be formally expanded as

$$\left[\delta_{i\alpha} - \epsilon\Lambda_{i\alpha}\right]^{-1} = \delta_{i\alpha} + \epsilon\Lambda_{i\alpha} + \epsilon^2\Lambda_{i\alpha}^2 + \epsilon^3\Lambda_{i\alpha}^3 + \cdots = \sum_{n=0}^{\infty}\epsilon^n\Lambda_{i\alpha}^n \tag{6.14}$$

where the notation $\Lambda_{i\alpha}^3 = \Lambda_{i\beta}\Lambda_{\beta\gamma}\Lambda_{\gamma\alpha}$ and $\Lambda_{i\alpha}^0 = \delta_{i\alpha}$ has been used. Equation 6.3 can therefore be rewritten as

$$\mathcal{G}_{ES} = \frac{\rho}{m(2\pi)^{3/2}(\det T_{\alpha\beta})^{1/2}}\exp\left(-\frac{1}{2}\left(\sum_{n=0}^{\infty}\epsilon^n\Lambda_{i\alpha}^n\right)\theta_{\alpha j}^{-1}c_i c_j\right). \tag{6.15}$$

The summation in the exponent can be rewritten as a product of terms as

$$\begin{aligned}
\mathcal{G}_{ES} &= \frac{\rho}{m(2\pi)^{3/2}(\det T_{\beta\gamma})^{1/2}} \prod_{n=0}^{\infty} \exp\left(-\frac{1}{2}\left(\epsilon^n \Lambda_{i\alpha}^n\right)\theta_{\alpha j}^{-1} c_i c_j\right) \\
&= \frac{\rho}{m(2\pi)^{3/2}(\det T_{\beta\gamma})^{1/2}} \exp\left(-\frac{1}{2}\theta_{ij}^{-1} c_i c_j\right) \prod_{n=1}^{\infty} \exp\left(-\frac{1}{2}\left(\epsilon^n \Lambda_{i\alpha}^n\right)\theta_{\alpha j}^{-1} c_i c_j\right) \\
&= \frac{\rho}{m(2\pi)^{3/2}(\det T_{\beta\gamma})^{1/2}} \exp\left(-\frac{1}{2}\theta_{ij}^{-1} c_i c_j\right) \prod_{n=1}^{\infty} \left(\sum_{k=0}^{\infty} \frac{\left(-\frac{1}{2}\epsilon^n \Lambda_{i\alpha}^n \theta_{\alpha j}^{-1} c_i c_j\right)^k}{k!}\right) \\
&= \frac{\rho}{m(2\pi)^{3/2}(\det T_{\beta\gamma})^{1/2}} \exp\left(-\frac{1}{2}\theta_{ij}^{-1} c_i c_j\right) \left[1 + \left(-\frac{\epsilon}{2}\Lambda_{i\alpha}\theta_{\alpha j}^{-1} c_i c_j\right) + \mathcal{O}\left(\epsilon^2\right)\right] . \quad (6.16)
\end{aligned}$$

At this point, using the small scaling parameter, ϵ, the scaled distribution function is assumed to have the form

$$\mathcal{F} = \mathcal{G}\left(g^{(0)} + \epsilon g^{(1)} + \epsilon^2 g^{(2)} + \epsilon^3 g^{(3)} + \cdots\right) . \quad (6.17)$$

This is then substituted into the scaled kinetic equation using equation 6.16, which yields

$$\frac{\partial \mathcal{F}}{\partial t} + v_k \frac{\partial \mathcal{F}}{\partial x_k} + = -\frac{\mathrm{Pr}}{\epsilon\tau}\left\{\mathcal{F} - \mathcal{G}\left[1 + \left(-\frac{\epsilon}{2}\Lambda_{i\alpha}\theta_{\alpha j}^{-1} c_i c_j\right)\right]\right\} , \quad (6.18)$$

where the smallness parameter multiplying the relaxation time is akin to assuming that the collision operator will force general distribution functions towards a Gaussian on a very fast time scale. Equation 6.18 can be rewritten by gathering terms of similar order in ϵ,

$$\begin{aligned}
\tfrac{\mathrm{Pr}}{\tau}\mathcal{G}\left[g^{(0)} - 1\right] + \epsilon\left[\tfrac{\partial g^{(0)}\mathcal{G}}{\partial t} + v_k \tfrac{\partial g^{(0)}\mathcal{G}}{\partial x_k} - \tfrac{\mathrm{Pr}}{\tau}\left\{\left(\tfrac{1}{2}\mathcal{G}\Lambda_{i\alpha}\theta_{\alpha j}^{-1} c_i c_j\right) - g^{(1)}\mathcal{G}\right\}\right] \\
+\epsilon^2\left[\cdots\right] + \epsilon^3\left[\cdots\right] = 0 \quad . \quad (6.19)
\end{aligned}$$

It is clear that the zeroth-order solution to this equation is $g^{(0)} = 1$. Retaining first-order terms, the relation

$$g^{(1)}\mathcal{G} = -\frac{\tau}{\mathrm{Pr}}\left[\frac{\partial \mathcal{G}}{\partial t} + v_k \frac{\partial \mathcal{G}}{\partial x_k} - \frac{\mathrm{Pr}}{2\tau}\mathcal{G}\Lambda_{i\alpha}\theta_{\alpha j}^{-1} c_i c_j\right] , \quad (6.20)$$

is obtained. Substitution of this relation into the unscaled kinetic equation (*i.e.*, using $\mathcal{F} = \mathcal{G}\left(1 + g^{(1)}\right)$) and taking moments using the weighting functions $\mathbf{V} = [m\,, mv_i\,, mv_i v_j]$ leads to

$$\begin{aligned}
\left\langle \mathbf{V}\frac{\partial \mathcal{G}}{\partial t}\right\rangle + \left\langle \mathbf{V}\frac{\partial\left(g^{(1)}\mathcal{G}\right)}{\partial t}\right\rangle + \left\langle \mathbf{V}v_k\frac{\partial \mathcal{G}}{\partial x_k}\right\rangle + \left\langle \mathbf{V}v_k\frac{\partial\left(g^{(1)}\mathcal{G}\right)}{\partial x_k}\right\rangle = \\
\frac{\mathrm{Pr}}{\tau}\left\langle \mathbf{V}\left(\mathcal{G}_{ES} - \mathcal{G}\right)\right\rangle - \frac{\mathrm{Pr}}{\tau}\left\langle \mathbf{V}\left(g^{(1)}\mathcal{G}\right)\right\rangle . \quad (6.21)
\end{aligned}$$

The second term on the left-hand side, as well as the second term on the right-hand side, must be equal to zero. This is because solution consistency dictates that $\left\langle \mathbf{V}\left(g^{(1)}\mathcal{G}\right)\right\rangle$ cannot alter the zeroth-order values of $\langle \mathbf{V}\mathcal{G}\rangle$. Once the moments have been computed, equation 6.21 can be written as

$$\frac{\partial \mathbf{U}}{\partial t} + \frac{\partial \mathbf{F}_k}{\partial x_k} + \frac{\partial}{\partial x_k}\left\langle \mathbf{V} v_k g^{(1)}\mathcal{G}\right\rangle = \frac{\mathbf{C}}{\tau}\left(\mathbf{U}_{ES} - \mathbf{U}\right) , \tag{6.22}$$

where $\mathbf{U}$ is the solution state, $\mathbf{U}_{ES}$ is the solution state variables obtained from the ellipsoidal statistical distribution function, $\mathbf{F}_k$ is the flux diad and $\mathbf{C}$ is a vector arising from the collision operator. It is therefore clear that $\left\langle \mathbf{V} v_k g^{(1)}\mathcal{G}\right\rangle$ must be determined. The same consistency argument made earlier shows that the moments $\left\langle m v_i g^{(1)}\mathcal{G}\right\rangle$ and $\left\langle m v_i v_j g^{(1)}\mathcal{G}\right\rangle$ must be zero and that $\left\langle m v_i v_j v_k g^{(1)}\mathcal{G}\right\rangle = \left\langle m c_i c_j c_k g^{(1)}\mathcal{G}\right\rangle$. It is this moment which must be determined. This can be written as

$$\left\langle m c_i c_j c_k g^{(1)}\mathcal{G}\right\rangle = -\frac{\tau}{\mathrm{Pr}}\left\langle m c_i c_j c_k \left(\frac{\partial \mathcal{G}}{\partial t} + v_l \frac{\partial \mathcal{G}}{\partial x_l} - \frac{\mathrm{Pr}}{2\tau}\mathcal{G}\Lambda_{l\alpha}\theta^{-1}_{\alpha m} c_l c_m\right)\right\rangle . \tag{6.23}$$

The moment $\left\langle m c_i c_j c_k c_l c_m \frac{\mathrm{Pr}}{2\tau}\mathcal{G}\Lambda_{l\alpha}\theta^{-1}_{\alpha m}\right\rangle$ represents the integral of odd functions and is thus equal to zero. The completion of this derivation, therefore, requires the calculation of $\left\langle m c_i c_j c_k \frac{\partial \mathcal{G}}{\partial t}\right\rangle$ and $\left\langle m c_i c_j c_k v_l \frac{\partial \mathcal{G}}{\partial x_l}\right\rangle$. These integrations will be demonstrated separately, beginning with $\left\langle m c_i c_j c_k \frac{\partial \mathcal{G}}{\partial t}\right\rangle$. This integration will make use of the fact that

$$\frac{1}{\mathcal{G}}\frac{\partial \mathcal{G}}{\partial t} = \frac{1}{\mathcal{G}}\frac{\partial \mathcal{G}}{\partial \rho}\frac{\partial \rho}{\partial t} + \frac{1}{\mathcal{G}}\frac{\partial \mathcal{G}}{\partial u_i}\frac{\partial u_i}{\partial t} + \frac{1}{\mathcal{G}}\frac{\partial \mathcal{G}}{\partial \Theta_{ij}}\frac{\partial \Theta_{ij}}{\partial t} . \tag{6.24}$$

The derivatives of the Gaussian distribution function with respect to the quantities ρ, u_i and θ_{ij} can be shown to be

$$\frac{1}{\mathcal{G}}\frac{\partial \mathcal{G}}{\partial \rho} = \frac{1}{\rho} , \tag{6.25}$$

$$\frac{1}{\mathcal{G}}\frac{\partial \mathcal{G}}{\partial u_i} = \Theta^{-1}_{ik} c_k , \tag{6.26}$$

$$\frac{1}{\mathcal{G}}\frac{\partial \mathcal{G}}{\partial \Theta_{ij}} = -\frac{1}{2}\frac{1}{\det \Theta_{\gamma\delta}}\frac{\partial \det \Theta_{\gamma\delta}}{\partial \Theta_{ij}} - \frac{1}{2}\frac{\partial \Theta^{-1}_{kl}}{\partial \Theta_{ij}} c_k c_l . \tag{6.27}$$

This results in the following expression

$$\begin{aligned}
\left\langle mc_ic_jc_k\frac{\partial\mathcal{G}}{\partial t}\right\rangle &= \overbrace{\left\langle mc_ic_jc_k\frac{1}{\rho}\mathcal{G}\frac{\partial\rho}{\partial t}\right\rangle}^{\text{odd}}+\left\langle mc_ic_jc_k\Theta^{-1}_{\alpha l}c_l\mathcal{G}\frac{\partial u_\alpha}{\partial t}\right\rangle \\
&\quad+\underbrace{\left\langle mc_ic_jc_k\left[-\frac{1}{2}\frac{1}{\det\Theta_{\gamma\delta}}\frac{\partial\det\Theta_{\gamma\delta}}{\partial\Theta_{\alpha\beta}}-\frac{1}{2}\frac{\partial\Theta^{-1}_{\gamma\delta}}{\partial\Theta_{\alpha\beta}}c_\gamma c_\delta\right]\mathcal{G}\frac{\partial\Theta_{\alpha\beta}}{\partial t}\right\rangle}_{\text{odd}} \\
&= \Theta^{-1}_{\alpha l}\left\langle c_ic_jc_kc_l\mathcal{G}\right\rangle\frac{\partial u_\alpha}{\partial t} \\
&= \Theta^{-1}_{\alpha l}\frac{[P_{ij}P_{kl}+P_{ik}P_{jl}+P_{il}P_{jk}]}{\rho}\left\{-u_\beta\frac{\partial u_\alpha}{\partial x_\beta}-\frac{1}{\rho}\frac{\partial P_{\alpha\beta}}{\partial x_\beta}\right\} \\
&= -\frac{1}{\rho}\left[P_{ij}\frac{\partial P_{k\beta}}{\partial x_\beta}+P_{ik}\frac{\partial P_{j\beta}}{\partial x_\beta}+P_{jk}\frac{\partial P_{i\beta}}{\partial x_\beta}\right] \\
&\quad-\left[P_{ij}u_\beta\frac{\partial u_k}{\partial x_\beta}+P_{ik}u_\beta\frac{\partial u_j}{\partial x_\beta}+P_{jk}u_\beta\frac{\partial u_i}{\partial x_\beta}\right]. \qquad (6.28)
\end{aligned}$$

The moment $\left\langle mc_ic_jc_kv_l\frac{\partial\mathcal{G}}{\partial x_l}\right\rangle$ can be integrated as

$$\begin{aligned}
\left\langle mc_ic_jc_kv_l\frac{\partial\mathcal{G}}{\partial x_l}\right\rangle &= \frac{\partial}{\partial x_l}\left\langle mc_ic_jc_kv_l\mathcal{G}\right\rangle-\left\langle\mathcal{G}\frac{\partial}{\partial x_l}\left[mc_ic_jc_kv_l\right]\right\rangle \\
&= \frac{\partial}{\partial x_l}\left[\left\langle mc_ic_jc_kc_l\mathcal{G}\right\rangle+u_l\underbrace{\left\langle mc_ic_jc_k\mathcal{G}\right\rangle}_{\text{odd}}\right] \\
&\quad-\left\langle\mathcal{G}\left[mc_ic_jv_l\frac{\partial c_k}{\partial x_l}+mc_ic_kv_l\frac{\partial c_j}{\partial x_l}+mc_jc_kv_l\frac{\partial c_i}{\partial x_l}\right]\right\rangle \\
&= \frac{\partial}{\partial x_l}\left\langle mc_ic_jc_kc_l\mathcal{G}\right\rangle+\left\langle\mathcal{G}\left[mc_ic_jv_l\frac{\partial u_k}{\partial x_l}+mc_ic_kv_l\frac{\partial u_j}{\partial x_l}+mc_jc_kv_l\frac{\partial u_i}{\partial x_l}\right]\right\rangle \\
&= \frac{\partial}{\partial x_l}\left\langle mc_ic_jc_kc_l\mathcal{G}\right\rangle+\overbrace{\left\langle\mathcal{G}\left[mc_ic_jc_l\frac{\partial u_k}{\partial x_l}+mc_ic_kc_l\frac{\partial u_j}{\partial x_l}+mc_jc_kc_l\frac{\partial u_i}{\partial x_l}\right]\right\rangle}^{\text{odd}} \\
&\quad+u_l\left\langle\mathcal{G}\left[mc_ic_j\frac{\partial u_k}{\partial x_l}+mc_ic_k\frac{\partial u_j}{\partial x_l}+mc_jc_k\frac{\partial u_i}{\partial x_l}\right]\right\rangle \\
&= \frac{\partial}{\partial x_l}\left[\frac{P_{ij}P_{kl}+P_{ik}P_{jl}+P_{il}P_{jk}}{\rho}\right] \\
&\quad+u_l\left[P_{ij}\frac{\partial u_k}{\partial x_l}+P_{ik}\frac{\partial u_j}{\partial x_l}+P_{jk}\frac{\partial u_i}{\partial x_l}\right]. \qquad (6.29)
\end{aligned}$$

This series of steps made use of the facts that $\frac{\partial v_i}{\partial x_j}=0$ and $\frac{\partial c_k}{\partial x_l}=-\frac{\partial u_k}{\partial x_l}$.

Combination of equations 6.28 and 6.29, followed by some simple algebra, leads to

the relation

$$Q_{ijk} = \left\langle mc_i c_j c_k g^{(1)} \mathcal{G} \right\rangle = -\frac{\tau}{\mathrm{Pr}} \left[P_{kl} \frac{\partial}{\partial x_l} \left(\frac{P_{ij}}{\rho} \right) + P_{jl} \frac{\partial}{\partial x_l} \left(\frac{P_{ik}}{\rho} \right) + P_{il} \frac{\partial}{\partial x_l} \left(\frac{P_{jk}}{\rho} \right) \right], \tag{6.30}$$

which is exactly the same result as obtained by the previous derivation based on a perturbative expansion applied directly to the moment equations. It should also be pointed out that these same thermal diffusion terms can also easily be used "as is" with the diatomic form of the Gaussian moment equations.

6.2 Regularized Gaussian Moment Equations

When the proposed treatment for thermal diffusion is inserted into the standard unmodified Gaussian moment equations for diatomic gas flow, the resulting equations for the regularized closure can be written as

$$\frac{\partial \rho}{\partial t} + \frac{\partial}{\partial x_k} \left(\rho u_k \right) = 0 \,, \tag{6.31}$$

$$\frac{\partial}{\partial t}(\rho u_i) + \frac{\partial}{\partial x_k}(\rho u_i u_k + P_{ik}) = 0 \,, \tag{6.32}$$

$$\begin{aligned} &\frac{\partial}{\partial t} \left(P_{ij} + \rho u_i u_j \right) + \frac{\partial}{\partial x_k} \left(\rho u_i u_j u_k + u_i P_{jk} + u_j P_{ik} + u_k P_{ij} \right) \\ &- \frac{\partial}{\partial x_k} \left(\frac{\tau}{\mathrm{Pr}} \left[P_{kl} \frac{\partial}{\partial x_l} \left(\frac{P_{ij}}{\rho} \right) + P_{jl} \frac{\partial}{\partial x_l} \left(\frac{P_{ik}}{\rho} \right) + P_{il} \frac{\partial}{\partial x_l} \left(\frac{P_{jk}}{\rho} \right) \right] \right) \\ &= -\frac{3P_{ij} - P_{kk}\delta_{ij}}{3\tau_t} - \frac{2(P_{kk} - 3E_{rot})}{15\tau_r} \delta_{ij} \,, \end{aligned} \tag{6.33}$$

$$\frac{\partial}{\partial t}(E_{rot}) + \frac{\partial}{\partial x_k}(u_k E_{rot}) = -\frac{3E_{rot} - P_{kk}}{5\tau_r} \,. \tag{6.34}$$

As can be seen, the moment equations for density, momentum, and rotational energy are unmodified. The additional thermal-diffusion terms are present only in the six translational energy equations.

6.2.1 Solid-Wall Boundary Conditions

For this study, the same Knudsen-layer boundary conditions for the 10-moment equations as mentioned above were utilized. However, the thermal diffusion terms which are added

to the standard Gaussian closure when used with Knudsen-layer boundary conditions [7] do not allow for temperature slip between the gas and solid boundary. However this phenomenon is expected for moderate Knudsen-number flows and must be accounted for. Temperature-slip boundary conditions have been previously studied [85]. For the present work, the following expression is used

$$T = T_w + g\lambda \frac{\partial T}{\partial n_i}\,, \tag{6.35}$$

where T is the temperature of the fluid at the boundary, T_w is the temperature of the wall, n_i is the unit normal to the wall, and g is the slip distance factor given by the expression

$$g = \frac{10\pi}{16\mathrm{Pr}} \left(\frac{2 - \alpha_t}{\alpha_t} \right) \frac{\gamma}{\gamma + 1}\,. \tag{6.36}$$

Here α_t is a thermal accommodation coefficient which describes the fractional extent to which molecules which impact a surface and are re-emitted from it have their energy adjusted to that of a stream of particles in thermal equilibrium with the wall; $\alpha_t = 0$ corresponds to reflected particles having no change to their energy and $\alpha_t = 1$ corresponds to particles begin fully thermally accommodated by the wall. These boundary conditions can be combined with Knudsen-layer boundary conditions, described earlier in chapter 4, by assuming that particles are emitted from solid boundaries at the temperature predicted by the slip condition of equation 6.35.

6.3 Parallel AMR Finite-Volume Scheme

In order to explore the present regularized 10-moment model, the same parallel high-order Godunov-type finite-volume scheme with block-based adaptive mesh refinement (AMR) from the previous chapters was utilized. The elliptic fluxes arising from thermal diffusion are calculated using the diamond-path reconstruction technique [16, 25].

The time-marching method used is the same predictor-corrector method shown in equations 4.47 and 4.48. This point-implicit technique, which treats the flux terms explicitly, is not ideal for the regularized moment equations. This is due to the fact that when the fluxes contain elliptic terms the stability limit of the time-marching scheme is proportional to $1/(\Delta x)^2$. As Knudsen numbers increase (*i.e.*, length scales become small) this limit on the time step quickly becomes extremely restrictive. This is another numerical reason why hyperbolic equations are preferable, the time-step restriction on

hyperbolic equations is only proportional to $1/\Delta x$. Nevertheless, for the cases to be considered herein, the computational expense involved in the solution of the regularized moment equations was high, but not intractable.

6.4 Numerical Results

Application of the regularized Gaussian closure discussed above to some standard flow problems is now considered for a range of Knudsen numbers. For the calculation of the mean free path required to determine the Knudsen number, the gas is assumed to be comprised of hard spheres and equation 4.46 is again used.

6.4.1 Shock-Structure Calculations

As a preliminary study into the behaviour of the Gaussian closure with the present correction for thermal diffusion, one-dimensional planar shock structures were investigated for shock waves of differing strengths travelling through argon, as was investigated in chapter 4. The internal structure of shocks is characterized by highly non-equilibrium features and represents a significant challenge for any non-equilibrium model. The results of the present investigation can be seen in figures 6.1 and 6.2 where normalized density and one entry of the generalized heat-flux tensor, Q_{xxx}, are plotted. The density is again normalized by the relation

$$\rho^\star = \frac{\rho - \rho_u}{\rho_d - \rho_u},$$

where ρ_u and ρ_d are the upstream and downstream densities respectively. The heat-flux entry Q_{xxx} is normalized as

$$Q^\star_{xxx} = \frac{Q_{xxx}}{\left(p_{xx}\sqrt{\frac{p_{xx}}{\rho}}\right)}.$$

Results for shock Mach numbers, $\mathrm{Ma_s}$, of 1.2, 1.5, and 2 are shown.

Again, due to hyperbolicity of the standard moment equations, above a critical Mach number a discontinuity is observed, as was explained in chapter 4. This discontinuity can clearly be seen in the $\mathrm{Ma_s} = 1.5$ and $\mathrm{M_s} = 2$ cases of figures 6.1(b) and 6.1(c). Conversely, it can be seen that the proposed correction for thermal diffusion leads to smooth (fully dispersed) shock transitions for a wide range of shock Mach numbers, as should be expected by the regularization procedure. It can also be seen that for lower-Mach-number cases, the agreement between the regularized Gaussian moment equations

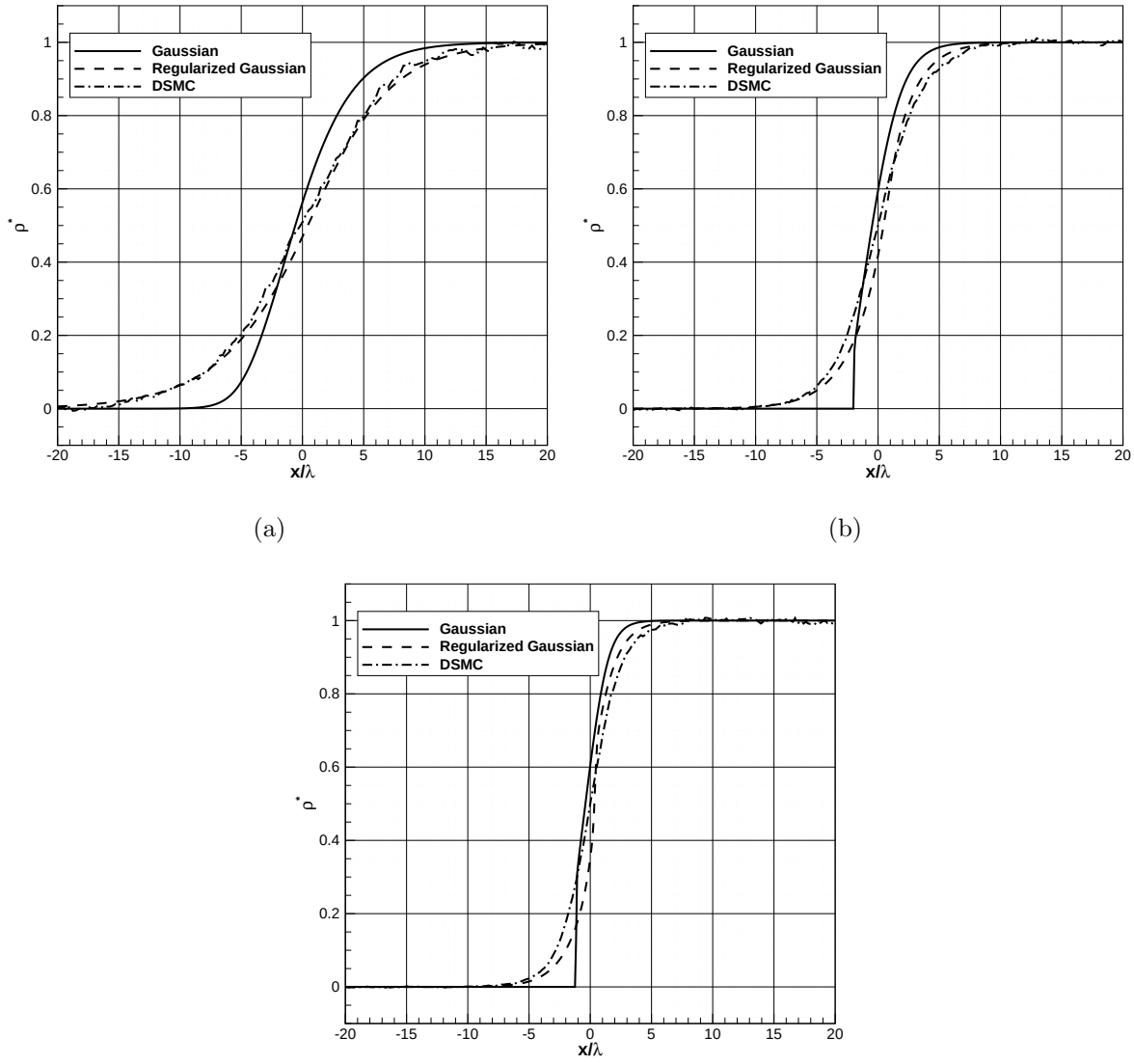

Figure 6.1: Normalized density variations through shock waves with shock Mach numbers of (a) $\mathrm{Ma_s} = 1.2$, (b) $\mathrm{Ma_s} = 1.5$, and (c) $\mathrm{Ma_s} = 2$ as predicted by regularized Gaussian model.

and DSMC calculations is generally quite good. However, for the $\mathrm{Ma_s} = 2$ case, the generalized Gaussian and the DSMC results begin to differ due to the increased amount of non-equilibrium effects present. A comparison of the predicted normalized values of Q_{xxx} for the regularized Gaussian closure and DSMC are shown in figure 6.2. Again it can be seen that there is very good agreement, especially for shock Mach numbers of 1.2 and 1.5.

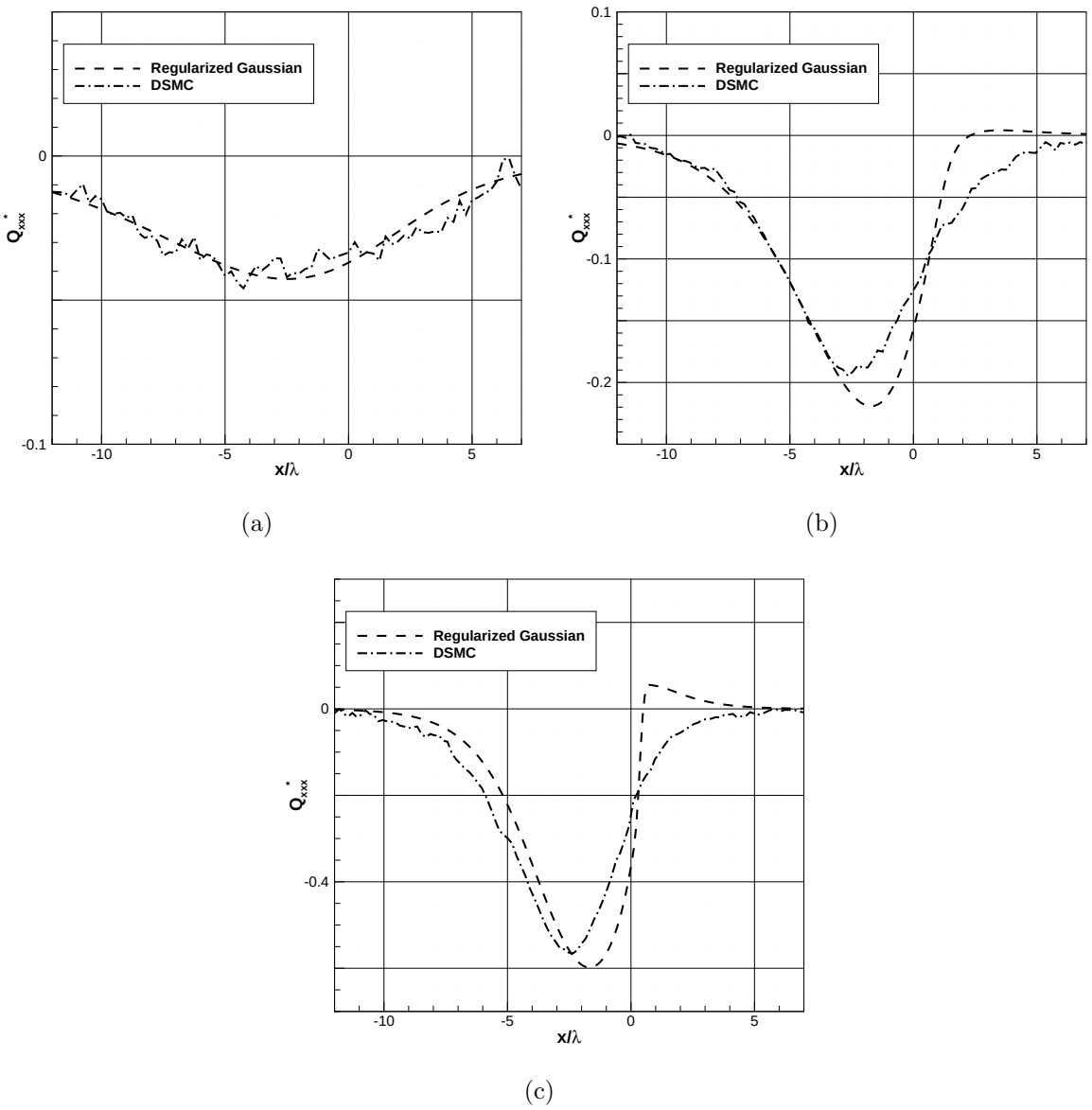

Figure 6.2: Normalized heat-flux variations through shock waves with shock Mach numbers of (a) $Ma_s = 1.2$, (b) $Ma_s = 1.5$, and (c) $Ma_s = 2$ as predicted by regularized Gaussian model.

6.4.2 Heat Transfer Between Infinite Plates

A good test case to verify the proper implementation of the temperature-slip boundary conditions is heat transfer between infinite isothermal plates. This case can be used both to ensure that the correct temperature slip is predicted at the boundary and to study the predicted heat transfer between the plates over a range of flow regimes and Knudsen

numbers. It is expected that for low-Knudsen-number situations, the temperature slip between the boundary and the fluid should be imperceptible. It is only as the Knudsen number increases into the slip-flow regime that any appreciable slip should be observed. Finally, in the limit of infinite Knudsen number, the temperature slip should be perfect and the fluid should have a uniform temperature throughout.

Figure 6.3(a) shows the temperature of argon gas at one of the solid plates for the situation where the plate temperatures differ by 20 K. This temperature is normalized by the formula

$$T^\star = \frac{T - T_m}{T_w - T_m},$$

where $T^\star$ is the normalized temperature, T is the temperature of the gas at the boundary, T_w is the temperature of the solid wall, and T_m is the temperature of the gas midway between the plates. It can be seen that all of the expected behaviours detailed above are observed; there is no noticeable slip ($T^\star \approx 1$) in the low-Knudsen-number situations and the slip approaches perfect slip conditions ($T^\star \to 0$) as the Knudsen number increases.

Non-continuum effects are also very evident when the predicted heat transfer between the plates is considered. This data has been plotted in figure 6.3(b). This figure shows the predicted heat flux for the continuum Navier-Stokes equations, the Navier-Stokes equations with slip-temperature boundary conditions, solutions obtained using the regularized Gaussian moment equations with slip boundary conditions, and the heat flux predicted by integration of two half Maxwellians emitted from the solid walls (the free-molecular solution); these have all been normalized with respect to the free-molecular solution. It can be seen that the extended Gaussian moment equations together with slip-temperature boundary condition transition from the continuum solution to a free-molecular limit which is slightly higher than the true free-molecular solution. This is a consequence of the derivation used to calculate the slip distance (equation. 6.36). It is possible to "tune" the slip distance so as to obtain the correct free-molecular heat flux for the case of heat transfer between two plates, however it would only be correct in this situation. It seems more advisable to use the equation for slip distance given above as this is derived from more physical arguments.

6.4.3 Subsonic Flow Past a Circular Cylinder

In order to investigate whether the new thermal-diffusion terms provided by the regularization procedure improve flow predictions for transition regime flows, subsonic airflow

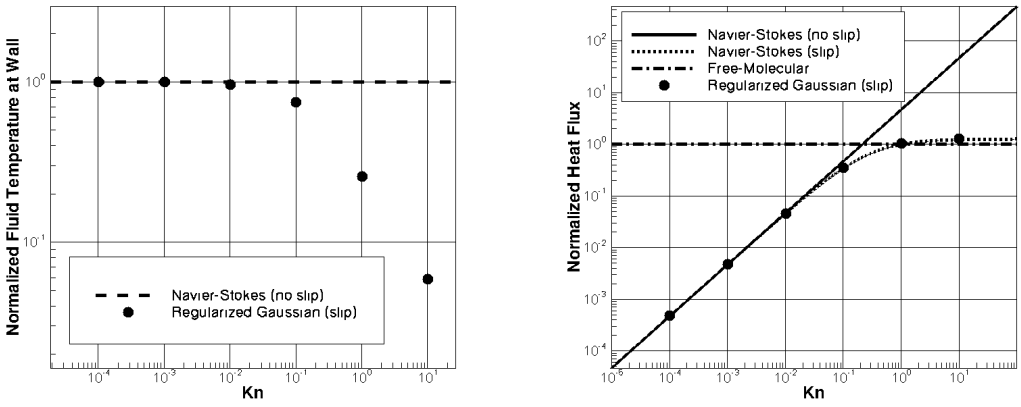

(a) (b)

Figure 6.3: Heat transfer between infinite plates: (a) normalized temperature of the gas the wall, (b) predicted heat flux between the plates using regularized Gaussian model.

past a circular cylinder is again considered. With hopes of obtaining better agreement for higher-Knudsen-number situations than was found is sections 4.5.6 and 5.2.2, these flow situations were re-computed using the regularized Gaussian moment equations. Figure 6.4 shows the results of this effort.

Before considering the results of figure 6.4, it should be mentioned that it was found that the slip-temperature boundary conditions described above introduce numerical difficulties for the cylinder flows and often result in aphysical negative temperatures at the boundary when a large temperature gradient at the surface of the cylinder is produced by compressibility effects. This is especially true for higher-Knudsen-number situations when length scales are very small and even small temperature differences produce large gradients. In order to obtain solutions, it was found that isothermal boundary conditions had to be imposed at the cylinder wall. This was carried out by maintaining a fixed or constant value for the wall temperature, T_w.

In figure 6.4, it is observed that for lower-Knudsen-number cases the good agreement between the Gaussian moment equations and the experimental results is not degraded. As the Knudsen number increases, it can be seen that the thermal diffusion leads to a reduction of the drag coefficient. Initially this seems promising as the original unmodified Gaussian closure tends to vastly over-predict the drag at high Knudsen numbers, however the reduction in the drag caused by the inclusion of heat transfer becomes too large. The

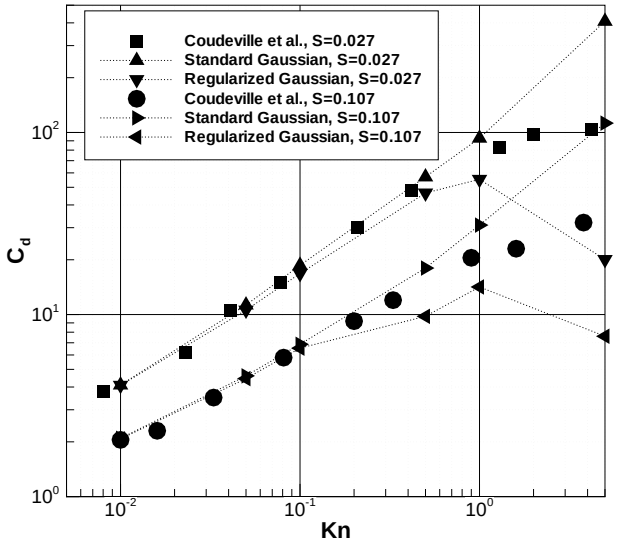

Figure 6.4: Coefficients of drag for $S = 0.027$ and $S = 0.107$ airflow past a circular cylinder computed using the standard and regularized Gaussian moment closure on a body-fitted mesh as compared to experimental results of Coudeville *et al.* [74]

drag is now under-predicted for high Knudsen numbers.

6.4.4 Transonic Flow Past a NACA0012 Micro Airfoil

As a final example and to illustrate the importance of heat transfer in many transition-regime flow problems, transonic steady flow of air around a NACA0012 micro-airfoil at zero angle of attack is again considered. This is the same situation as was considered in section 4.5.7. For the case of interest, the free-stream Mach and Reynolds numbers are $\mathrm{M} = 0.8$ and $\mathrm{Re} = 73$, respectively, and the Knudsen number is $\mathrm{Kn} = 0.017$ based on the chord length. Numerical predictions for this flow were obtained using the regularized Gaussian moment equations, with extensions for a diatomic gas, and are given in figure 6.5(b).

Numerical predictions of the distribution of the flow density are again shown in the figures. For comparison, results obtained using the DSMC scheme by Sun and Boyd [6] and corresponding experimental results based on the measurements of Allegre, Raffin and Lengrand [76] are also reproduced here in figures 6.5(c) and 6.5(d).

It is evident from the comparisons of figures 6.5(a)–6.5(d) that the predictions obtained using the standard and regularized Gaussian closure agree surprisingly well with both the DSMC and experiment results in the vicinity of the leading edge of the airfoil. In fact, the 10-moment model provides a better estimate of the stagnation-point density than the DSMC method, which tends to overestimate this value. The disagreement with DSMC results and experimental measurements in the stagnation region illustrates the imperfections, uncertainties, and challenges with predicting micro-scale non-equilibrium flows, even with particle-based methods.

In spite of the good predictive capabilities of the standard Gaussian model for the leading edge region of the airfoil, the moment closure results in predicted flow densities that seem to be very much under-predicted along the length of the airfoil towards the trailing edge. Again, a similar finding was reported in the previous work of Suzuki and van Leer [77]. While it may be argued that some of this disagreement between the Gaussian closure and DSMC and experimental data may be attributed to the application of boundary conditions, the inclusion of thermal diffusion via the regularized Gaussian closure provides greatly improved agreement between the moment closure results and those of both DSMC and experiment, particularly towards the trailing edge of the airfoil. In general, the overall agreement between the regularized Gaussian and DSMC and experimental results are very good and this strongly indicates the importance of non-equilibrium heat transfer for this class of flow problem. The comparisons would also suggest that a physically realizable and hyperbolic moment closure which properly accounts for non-equilibrium thermal transport has the potential to perform very well for problems of this type.

6.5 Observations

A new regularized form of the Gaussian closure has been developed, based on perturbative expansion techniques applied both to the moment equations and the underlying kinetic equation. It has been shown that this extension to the standard Gaussian moment equations can lead to improved results for transition-regime flows in which heat transfer has a significant effect. There are, however, several issues in the derivation which should be mentioned. First, the assumption that deviations from the moment quantities predicted by the Gaussian closure will be attenuated rapidly by collisional processes which lead to the introduction of ϵ on the right-hand side of equation 6.9 is

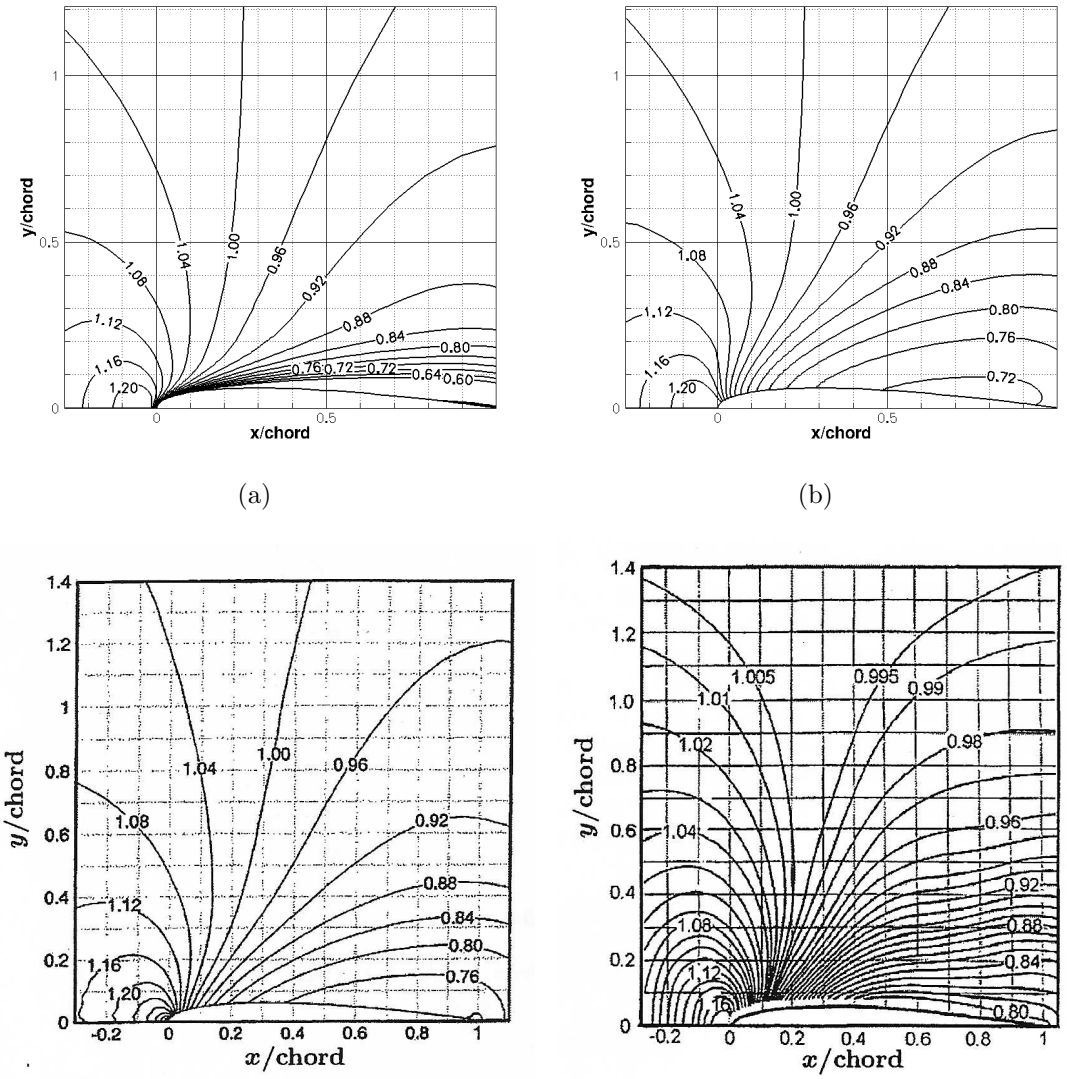

(a) (b)

(c) (d)

Figure 6.5: Comparison of the normalized density contours around a NACA0012 micro airfoil: (a) predictions of the standard Gaussian moment equations, (b) predictions of the the regularized Gaussian moment equations, (c) predictions of the DSMC-based method of Sun and Boyd [6] and (d) experimental data of Allegre, Raffin and Lengrand [76].

not well founded as relaxation times for higher-order moments tend to be larger than for lower-order moments [21].

There is a related problem with the derivation using the kinetic equation. Remembering the relation between the Prandtl number and the parameter ν in the ellipsoidal statistical collision model ($(1-\nu)\mathrm{Pr} = 1$), it can be seen that the assumption that

$(1-\nu) = \epsilon \ll 1$ is equivalent to assuming that the Prandtl number of the gas is much larger than unity. This is in contrast with many typical gases.

It should also be mentioned that the ellipsoidal statistical collision model's adherence to Boltzmann's H theorem has only been demonstrated for monatomic gases. However, experience obtained during this study suggests that for the present purposes it also leads to good results for diatomic gases.

The advantage of the regularized 10-moment equations is that they provide a set of PDEs for non-equilibrium, viscous, heat-conducting gas flows. The elliptic nature of the added terms is similar to the elliptic terms present in the Navier-Stokes equations. The numerical solution of the new equation can therefore be relatively easily carried out using virtually any of the standard numerical frameworks and techniques devised for the solution of the Navier-Stokes equations. Unfortunately, one of the main advantages of standard moment equations has been lost: their uniform hyperbolicity. It is for this reason that a hyperbolic set of higher-order moment equations that provides a treatment for heat transfer is sought. This will be the subject of chapter 7.

Chapter 7

Higher-Order Moment Closures

It has been demonstrated in chapters 4 and 5 that the Gaussian closure offers a fully hyperbolic treatment for viscous gas-flow prediction. As was stated earlier, this 10-moment system obtained closure through the choice of a maximum-entropy distribution function constrained by the choice of moments which yields no heat transfer by construction. Although the regularization procedure developed in chapter 6 leads to useful fluid-dynamic equations that include heat transfer, the resulting moment equations have an elliptic nature and strict hyperbolicity is lost. Following the successes of the 10-moment maximum-entropy closure, high expectations for closures of this type to effectively model viscous heat-conducting gas flows seem justified and higher-order members of the Levermore hierarchy, for example the 14-, 20-, and 35-moment closures, do provide a hyperbolic treatment for heat-transfer effects. Unfortunately things are not so easy. There exist two impediments to the use of higher-order maximum-entropy moment closures. Firstly, closed-form expressions for the integrals of the maximum-entropy distribution functions do not exist in general. This means that expressions relating the closure coefficients, $\boldsymbol{\alpha}^{(N)}$, to the macroscopic moments, $\boldsymbol{U}^{(N)}$, cannot be found. The result of this is that at every instance that a flux is needed, the entropy maximization problem must be solved numerically, as shown in section 3.2. This maximization problem must be solved iteratively in a procedure that requires the repeated accurate numerical integration of distribution functions whose domain stretches from negative to positive infinity in all directions of velocity space. This problem adds a huge numerical expense to the solution of higher-order moment closures, however there is a more subtle and far more devastating issue. It has been shown that for all members of the Levermore hierarchy of moments closures which contain moments corresponding to super-quadratic velocity weights there

exist physically realistic moment values for which the underlying entropy maximization problem has no solution [28, 29]. In these regions the whole mathematical framework on which the method is based breaks down.

In this chapter, a simplified one-dimensional 5-moment maximum-entropy model is considered in order to better study the practical implications of both of these challenging issues. Several techniques aimed at rectifying the problems associated with higher-order maximum-entropy closures are presented and numerical solutions to several canonical flow problems are discussed.

7.1 Mathematical Properties of One-Dimensional Moment Closures

In order to examine the modelling issues associated with higher-order maximum-entropy closures, kinetic theory applied to a one-dimensional gas is considered. A one-dimensional gas is defined as a gas whose molecules can only have velocities in one space dimension. In the case of no external acceleration fields, the Boltzmann equation for a one-dimensional gas simplifies to

$$\frac{\partial \mathcal{F}}{\partial t} + v\frac{\partial \mathcal{F}}{\partial x} = \frac{\delta \mathcal{F}}{\delta t}\,. \tag{7.1}$$

Now independent variables velocity, v, and position, x, are scalars. Similarly, Maxwell's equation of change simplifies to

$$\frac{\partial}{\partial t}\left\langle mM\mathcal{F}\right\rangle + \frac{\partial}{\partial x}\left\langle mvM\mathcal{F}\right\rangle = \Delta[M\mathcal{F}]\,. \tag{7.2}$$

An N-moment system of moment equations corresponding to velocity weights $V^{(N)}$ can be written as

$$\frac{\partial \mathbf{U}^{(N)}}{\partial t} + \frac{\partial \mathbf{F}^{(N)}}{\partial x} = \mathbf{S}\,, \tag{7.3}$$

where $\mathbf{F}$ is now a vector rather than a diad and $\mathbf{S}$ is the local source vector arising from inter-particle collisions.

One-dimensional moment equations have some remarkable mathematical properties which can be examined by rewriting equation 7.3 as

$$\frac{\partial \mathbf{U}^{(N)}}{\partial t} + \frac{\partial \mathbf{F}^{(N)}}{\partial \mathbf{U}^{(N)}}\frac{\partial \mathbf{U}^{(N)}}{\partial x} = \mathbf{S}\,. \tag{7.4}$$

When polynomial velocity weights are used to generate the moment equations, the flux of one moment will be a moment that is of one order higher. For the simplified one-dimensional situation, the fact that velocity is a scalar means that there is only one

moment of each order and the flux Jacobian, $\frac{\partial \mathbf{F}^{(N)}}{\partial \mathbf{U}^{(N)}}$, has the structure of a companion matrix having the form

$$\frac{\partial \mathbf{F}^{(N)}}{\partial \mathbf{U}^{(N)}} = \begin{bmatrix} 0 & 1 & 0 & 0 & \cdots & 0 \\ 0 & 0 & 1 & 0 & \cdots & 0 \\ 0 & 0 & 0 & 1 & \cdots & 0 \\ \vdots & \vdots & \vdots & \ddots & \ddots & \vdots \\ 0 & 0 & 0 & 0 & \cdots & 1 \\ a_0 & a_1 & a_2 & a_3 & \cdots & a_{(N-1)} \end{bmatrix}. \tag{7.5}$$

Companion matrices[1] are interesting as their characteristic equation, $p(\lambda)$, has the form

$$p(\lambda) = a_0 + a_1\lambda + a_2\lambda^2 + a_3\lambda^3 + \cdots + a_{(N-1)}\lambda^{(N-1)} - \lambda^N . \tag{7.6}$$

The N roots of this equation, λ_n, represent the N eigenvalues of the matrix. Moreover, the matrix with right eigenvectors as columns that corresponds to a companion matrix is a Vandermonde matrix of the form

$$\bar{\mathbf{R}} = \begin{bmatrix} 1 & 1 & 1 & \cdots & 1 \\ \lambda_0 & \lambda_1 & \lambda_2 & \cdots & \lambda_{(N-1)} \\ \lambda_0^2 & \lambda_1^2 & \lambda_2^2 & \cdots & \lambda_{(N-1)}^2 \\ \lambda_0^3 & \lambda_1^3 & \lambda_2^3 & \cdots & \lambda_{(N-1)}^3 \\ \vdots & \vdots & \vdots & \vdots & \vdots \\ \lambda_0^{(N-1)} & \lambda_1^{(N-1)} & \lambda_2^{(N-1)} & \cdots & \lambda_{(N-1)}^{(N-1)} \end{bmatrix} \tag{7.7}$$

It is known that for all hyperbolic systems there exists a diagonal matrix, $\mathbf{W}$, containing eigenvector scalings, w_i, such that systems of the form shown in equation 7.4 can be written in symmetric form as

$$\bar{\mathbf{H}}\frac{\partial \boldsymbol{\alpha}}{\partial t} + \bar{\mathbf{J}}\frac{\partial \boldsymbol{\alpha}}{\partial x} = \mathbf{S}\,, \tag{7.8}$$

where $\bar{\mathbf{H}} = \bar{\mathbf{R}}\bar{\mathbf{W}}\bar{\mathbf{R}}^{\mathrm{T}}$ and $\bar{\mathbf{J}} = \bar{\mathbf{R}}\bar{\mathbf{W}}\bar{\mathbf{\Lambda}}\bar{\mathbf{R}}^{\mathrm{T}}$ are symmetric matrices while $\boldsymbol{\alpha}$ are the so-called entropy variables and $\mathbf{\Lambda}$ is a diagonal matrix containing the eigenvalues of the flux Jacobian [86]. It was shown in section 3.1 that for maximum-entropy moment closures, the symmetrizing variables are in fact the closure coefficients. These coefficients are also

[1]It should be noted that companion matrices are often, but not always, presented as having the structure of a matrix which is the transpose of the matrix above. The mathematical properties of companion matrices presented here are not changed by working with the transpose.

the entropy variables for the system, while $\bar{\mathbf{H}}$ and $\bar{\mathbf{J}}$ are the Hessians of the density and flux potentials, as given earlier in equations 3.16 and 3.17.

For the one dimensional case, both of the Hessians $\bar{\mathbf{H}}$ and $\bar{\mathbf{J}}$ are Hankel matrices whose entries are moments of the maximum-entropy distribution function. That is, they have the form

$$\bar{\mathbf{H}} = \begin{bmatrix} U_0 & U_1 & U_2 & \cdots & U_{N-1} \\ U_1 & U_2 & U_3 & \cdots & U_N \\ U_2 & U_3 & U_4 & \cdots & \vdots \\ \vdots & \vdots & \vdots & \ddots & U_{2N-3} \\ U_{N-1} & U_N & \cdots & U_{2N-3} & U_{2N-2} \end{bmatrix}, \tag{7.9}$$

and

$$\bar{\mathbf{J}} = \begin{bmatrix} U_1 & U_2 & U_3 & \cdots & U_N \\ U_2 & U_3 & U_4 & \cdots & U_{N+1} \\ U_3 & U_4 & U_5 & \cdots & \vdots \\ \vdots & \vdots & \vdots & \ddots & U_{2N-2} \\ U_N & U_{N+1} & \cdots & U_{2N-2} & U_{2N-1} \end{bmatrix}, \tag{7.10}$$

where here U_n is the nth-order conserved moment.

It is at this point that a very interesting property of one-dimensional maximum-entropy moment closures can be demonstrated. By carrying out the matrix multiplication $\bar{\mathbf{H}} = \bar{\mathbf{R}}\bar{\mathbf{W}}\bar{\mathbf{R}}^{\mathrm{T}}$ and $\bar{\mathbf{J}} = \bar{\mathbf{R}}\bar{\mathbf{W}}\bar{\mathbf{\Lambda}}\bar{\mathbf{R}}^{\mathrm{T}}$ with $\bar{\mathbf{R}}$, $\bar{\mathbf{H}}$, and $\bar{\mathbf{J}}$ defined by equations 7.7, 7.9, and 7.10 respectively, it can be seen that the conserved velocity moments can be expressed as

$$U_n = \sum_{i=0}^{(N-1)} w_i \lambda_i^n \quad \text{for} \quad n \leq 2N-1\,. \tag{7.11}$$

That is, the eigenvalues of the system are the N Gauss quadrature points for which the zeroth to the $(2N-1)$th moments of the maximum-entropy velocity distribution function are captured exactly and the N eigenvector scaling factors, w_i, are in fact the corresponding weights for the numerical integration rule. The relationship between the Vandermonde decomposition of a Hankel matrix and Gauss Quadrature rules has been known for some time [87, 88]. However, the surprising relationship between Gauss quadrature points and the eigenvalues of a maximum-entropy moment system does not seem to be in the published literature pertaining to moment closures for kinetic theory.

7.2 Navier-Stokes-Like Equations for a One-Dimensional Gas

In order to assess the advantages that the proposed hyperbolic moment closures have over traditional fluid-dynamic equations, a one-dimensional equivalent to the Navier-Stokes equations will be examined. The derivation of these equations for the one-dimensional gas is detailed here.

7.2.1 One-Dimensional Maxwell-Boltzmann Distribution and 3-Moment Equilibrium Closure

The equilibrium Maxwell-Boltzmann distribution function for a one-dimensional gas can be written as

$$\mathcal{M} = \frac{\rho}{m}\sqrt{\frac{\rho}{2\pi p}}\exp\left(-\frac{\rho}{2p}c^2\right) . \tag{7.12}$$

This distribution function has moments:

$$\begin{aligned}
\rho &= \langle m\mathcal{M}\rangle , & & \\
\rho u &= \langle mv\mathcal{M}\rangle , & 0 &= \langle mc\mathcal{M}\rangle , \\
\rho u^2 + p &= \langle mv^2\mathcal{M}\rangle , & p &= \langle mc^2\mathcal{M}\rangle , \\
\rho u^3 + 3up &= \langle mv^3\mathcal{M}\rangle , & 0 &= \langle mc^3\mathcal{M}\rangle , \\
\rho u^4 + 6u^2p + \frac{3p^2}{\rho} &= \langle mv^4\mathcal{M}\rangle , & \frac{3p^2}{\rho} &= \langle mc^4\mathcal{M}\rangle , \\
\rho u^5 + 10u^3p + 15u\frac{p^2}{\rho} &= \langle mv^5\mathcal{M}\rangle , & 0 &= \langle mc^5\mathcal{M}\rangle .
\end{aligned} \tag{7.13}$$

If this equilibrium distribution function is substituted into Maxwell's equation of change, the result is a three moment system that can be written as

$$\frac{\partial\rho}{\partial t} + \frac{\partial}{\partial x}(\rho u) = 0 , \tag{7.14}$$

$$\frac{\partial}{\partial t}(\rho u) + \frac{\partial}{\partial x}\left(\rho u^2 + p\right) = 0 , \tag{7.15}$$

$$\frac{\partial}{\partial t}\left(\rho u^2 + p\right) + \frac{\partial}{\partial x}\left(\rho u^3 + 3up\right) = 0 \quad . \tag{7.16}$$

This 3-moment Euler system describes one-dimensional gas flow in thermodynamic equilibrium. The system has wavespeeds $u + a$, u, and $u - a$ with $a = \sqrt{3p/\rho}$.

7.2.2 Collision Operators for a One-Dimensional Gas

The form of the BGK collision operator [36] is unaltered for a one-dimensional gas and can be written as

$$\frac{\delta \mathcal{F}}{\delta t} = -\frac{\mathcal{F} - \mathcal{M}}{\tau} \,. \tag{7.17}$$

Even though the aim of this chapter is to develop hyperbolic moment equations with a treatment for heat conduction, this collision operator will be sufficient. There is no need to worry about choosing a collision operator that has a tunable Prandtl number for this situation, as was needed in the previous chapter, because, by definition, one-dimensional gases are not permitted directional anisotropies. There is therefore no equivalent viscosity in this case and a Prandtl number cannot be defined nor is it relevant. The relaxation time in this collision operator will be tuned so as to agree with the thermal conductivity of the soon-to-be defined Navier-Stokes-like equations in the continuum limit.

7.2.3 Chapman-Enskog Expansion for a One-Dimensional Gas and Navier-Stokes Model

The Navier-Stokes-like equations for a one-dimensional gas can be derived through a Chapman-Enskog expansion, as was done for the derivation of the regularized Gaussian closure in section 6.1.1 of chapter 6. Once again it is convenient to define the fourth moment

$$k = \left\langle mc^4 \mathcal{F} \right\rangle - \left\langle mc^4 \mathcal{M} \right\rangle = \left\langle mc^4 \mathcal{F} \right\rangle - \frac{3p}{\rho} = r - \frac{3p}{\rho} \,, \tag{7.18}$$

which is the deviation of the fourth moment $r = \langle mc^4 \mathcal{F} \rangle$ from its value in thermodynamic equilibrium. Next, the third-order random-velocity heat-transfer moment $q = \langle mc^3 \mathcal{F} \rangle$ and k are written as perturbative expansions about their equilibrium value as

$$q = q^{(\mathcal{M})} + \epsilon q^{(1)} + \epsilon^2 q^{(2)} + \epsilon^3 q^{(3)} + \cdots \,, \tag{7.19}$$

$$k = k^{(\mathcal{M})} + \epsilon k^{(1)} + \epsilon^2 k^{(2)} + \epsilon^3 k^{(3)} + \cdots \,. \tag{7.20}$$

The moment equation for the second-order moment $\langle mv^2 \mathcal{F} \rangle$ can be written for a general distribution function as

$$\frac{\partial}{\partial t}\left(\rho u^2 + p\right) + \frac{\partial}{\partial x}\left(\rho u^3 + 3up + q\right) = 0 \,. \tag{7.21}$$

It is the moment q that corresponds to the heat flux and is not present in the equilibrium Euler equations for a one-dimensional gas (equations 7.14–7.16). The moment equation

that describes the evolution of q is then written with a scaled BGK collision term as

$$\frac{\partial q}{\partial t} + 4q\frac{\partial u}{\partial x} + u\frac{\partial q}{\partial x} + 3p\frac{\partial}{\partial x}\left(\frac{p}{\rho}\right) + \frac{\partial k}{\partial x} = -\frac{q}{\epsilon\tau}\,. \tag{7.22}$$

Here the smallness parameter ϵ on the right-hand side of the equations again signifies that any deviation from equilibrium is attenuated very rapidly. The expansions for q and k, equations 7.19 and 7.20, are now inserted and terms of equal order in ϵ are gathered. Once this is done it can be seen that the zeroth-order terms lead to the equation

$$q^{(\mathcal{M})} = 0\,, \tag{7.23}$$

and

$$k^{(\mathcal{M})} = 0\,, \tag{7.24}$$

as required. The first-order approximation to the heat-flux moment is then found to be

$$q^{(1)} = -3p\tau\frac{\partial}{\partial x}\left(\frac{p}{\rho}\right)\,. \tag{7.25}$$

This expression can then be combined with equation 7.21 to yield the one-dimensional Navier-Stokes-like equations that will be used as a representative continuum-regime model for comparison in this chapter. The resulting transport equations can be summarized as follows:

$$\frac{\partial \rho}{\partial t} + \frac{\partial}{\partial x}\left(\rho u\right) = 0\,, \tag{7.26}$$

$$\frac{\partial}{\partial t}\left(\rho u\right) + \frac{\partial}{\partial x}\left(\rho u^2 + p\right) = 0\,, \tag{7.27}$$

$$\frac{\partial}{\partial t}\left(\rho u^2 + p\right) + \frac{\partial}{\partial x}\left(\rho u^3 + 3up\right) - \frac{\partial}{\partial x}\left(3p\tau\frac{\partial}{\partial x}\left(\frac{p}{\rho}\right)\right) = 0 \quad . \tag{7.28}$$

7.3 A 5-Moment One-Dimensional Maximum-Entropy Moment Closure

The lowest-order member of the Levermore hierarchy for a one-dimensional gas which provides a treatment for heat transfer is a 5-moment system. The vector of generating weights is $\mathbf{V}^{(5)} = [1, v, v^2, v^3, v^4]^{\mathrm{T}}$; the resulting maximum-entropy distribution function is

$$\mathcal{F}^{(5)} = e^{(\alpha_0 + \alpha_1 v + \alpha_2 v^2 + \alpha_3 v^3 + \alpha_4 v^4)}\,, \tag{7.29}$$

and the corresponding moment equations are

$$\frac{\partial \rho}{\partial t} + \frac{\partial}{\partial x}(\rho u) = 0\,, \tag{7.30}$$

$$\frac{\partial}{\partial t}(\rho u) + \frac{\partial}{\partial x}\left(\rho u^2 + p\right) = 0\,, \tag{7.31}$$

$$\frac{\partial}{\partial t}\left(\rho u^2 + p\right) + \frac{\partial}{\partial x}\left(\rho u^3 + 3up + q\right) = 0\,, \tag{7.32}$$

$$\frac{\partial}{\partial t}\left(\rho u^3 + 3up + q\right) + \frac{\partial}{\partial x}\left(\rho u^4 + 6u^2 p + 4uq + r\right) = -\frac{q}{\tau}\,, \tag{7.33}$$

$$\frac{\partial}{\partial t}\left(\rho u^4 + 6u^2 p + 4uq + r\right) + \frac{\partial}{\partial x}\left(\rho u^5 + 10u^3 p + 10u^2 q + 5ur + s\right) = -\frac{1}{\tau}\left(4uq + r - 3\frac{p^2}{\rho}\right)\,. \tag{7.34}$$

It is the fifth-order random-velocity moment $s = \langle mc^5 \mathcal{F} \rangle$ which is not a member of the solution vector, and must therefore be determined from a closure relation. As explained earlier, the standard BGK relaxation operator is used to represent the collision terms.

The distribution function of equation 7.29 has been studied previously in the field of probability [89, 90, 91, 92]. It is known that moments of this distribution function, $\langle mv^n \mathcal{F} \rangle$, cannot be expressed as a closed-form function of the closure coefficients. This means that the closing flux cannot be expressed as an explicit function of the lower-order moments that are present in the solution vector. It is for this reason that the entropy-maximization problem must be solved numerically at every time a flux is needed in any numerical solution procedure for the moment equations.

Again, this is not the only hindrance to the use of such closures. As with all higher-order maximum-entropy closures, Junk has shown that there exist physically realizable moment states for this system for which the entropy-maximization problem has no solution. In these regions the entire mathematical framework of the maximum-entropy moment closure breaks down [28, 29].

7.4 Moment Realizability

The term moment realizability refers to the existence of a function with certain specified properties that correspond to a given set of moments. Although a finite set of velocity moments can not in general be used to uniquely specify a distribution function and multiple distributions can usually be defined which share the same N moment densities, in assessing moment realizability, the question is asked whether any distribution function

with specified properties can correspond to the given set of moments.

7.4.1 Physical Realizability

The question of physical realizability is a question of whether a positive, semi-definite, probability-density function exists which corresponds to certain prescribed moments. For any given set of velocity weights, $\mathbf{M} = m[1, v_i, v_i v_j, \ldots]^{\mathrm{T}}$, one can construct polynomials, $\mathcal{P}(v_i)$, as

$$\mathcal{P}(v_i) = \boldsymbol{a}^{\mathrm{T}}\mathbf{M}\,, \tag{7.35}$$

where $\boldsymbol{a}$ is a column vector containing the coefficients of the polynomial. For any positive-valued distribution, $\mathcal{F}$, and polynomial, $\mathcal{P}$, it is clearly a requirement that

$$<||\mathcal{P}(v_i)||^2\mathcal{F}> \;=\; \boldsymbol{a}^{\mathrm{T}} <\mathbf{M}\mathbf{M}^{\mathrm{T}}\mathcal{F}> \boldsymbol{a} \;=\; \boldsymbol{a}^{\mathrm{T}}\bar{\mathbf{Y}}\boldsymbol{a} \;\geq\; 0\,, \tag{7.36}$$

and thus the moments present in the real symmetric matrix $\bar{\mathbf{Y}}$, given by

$$\bar{\mathbf{Y}} =<\mathbf{M}\mathbf{M}^{\mathrm{T}}\mathcal{F}>\,, \tag{7.37}$$

are physically realizable provided this matrix is positive definite. It should be noted, that in assessing the physical realizability of a given moment state, the vector of velocity weights, $\mathbf{M}$, does not only need to be equal to the vector of generating weights, $\mathbf{V}^{(N)}$, of the known moments. In fact, for a distribution function to be realizable, the matrix $\bar{\mathbf{Y}}$ must be positive definite for every possible choice of $\mathbf{M}$. In order to assess the physical realizability of a specific moment state, the vector, $\mathbf{M}$, which will lead to the known moments being included in $\bar{\mathbf{Y}}$ should be chosen.

For situations in which $\bar{\mathbf{Y}}$ is not positive definite, it follows that the velocity moments it contains are not consistent with any possible positive-valued distribution function and, hence, are not physically realizable. The preceding analysis for physical moment realizability follows from the early work of Hamburger [93, 94] and is closely related to the now classical Hamburger moment problem.

7.4.2 Physical Realizability of 5-Moment Distribution Functions

By dimensional analysis and the requirement of Galilean invariance, it can be shown that, without loss of generality, a 5-moment distribution function, can be non-dimensionalized

such that $\rho = 1$, $u = 0$, and $p = 1$. The questions of realizability can therefore be explored on a non-dimensional $q^\star$-$r^\star$ plane with

$$q^\star = \frac{1}{\rho}\left(\frac{\rho}{p}\right)^{\frac{3}{2}} q \quad \text{and} \quad r^\star = \frac{1}{\rho}\left(\frac{\rho}{p}\right)^{2} r \tag{7.38}$$

Once this non-dimensionalization has been carried out, the matrix $\bar{\mathbf{Y}}$ of equation 7.37 that will show the region of physical realizability for the five moments considered in the above closure can be generated using the velocity weights $\mathbf{M} = [1, v, v^2]$ and can be written as

$$\bar{\mathbf{Y}} = \begin{bmatrix} 1 & 0 & 1 \\ 0 & 1 & q^\star \\ 1 & q^\star & r^\star \end{bmatrix}. \tag{7.39}$$

This matrix is positive-definite for all states for which $r^\star \geq 1 + (q^\star)^2$. These states are therefore physically possible. This is not to say that all points on this plane are realizable by a distribution function of the form given in equation 7.29, but that for any state that $r^\star \geq 1 + (q^\star)^2$ there exists *some* corresponding positive-valued distribution function.

7.4.3 Realizability of Maximum-Entropy Distribution Functions

As has been shown by Junk, there do exist moment states which satisfy the constraints on physical realizability but for which the entropy-maximization problem does not have a solution (*i.e.*, there is no corresponding distribution function of the form given in equation 7.29) [28, 29]. In these situations the distribution function that has the maximum entropy while being consistent with the moments cannot be said to exist.

Following the analysis of Junk, it can be shown that the physical region for which the entropy-maximization problem cannot be solved is the line on which $q^\star = 0$ and $r^\star > 3$. This last constraint is particularly troubling, as the point at the end of this line, $q^\star = 0$ and $r^\star = 3$ is the point that corresponds to local thermodynamic-equilibrium. The physically realizable region and line along which no maximum-entropy distribution exists is depicted in figure 7.1.

This issue of non-solvability of the entropy-maximization problem is related to the inability to satisfy simultaneously all of the restrictive conditions on the closure coefficients, $\boldsymbol{\alpha}^{(N)}$, which ensure that the polynomial $(\boldsymbol{\alpha})^{(N)\mathrm{T}}\mathbf{V}^{(N)}$ in equation 3.6 decreases toward negative infinity in all directions as $|v_i|$ becomes large. More devastating still,

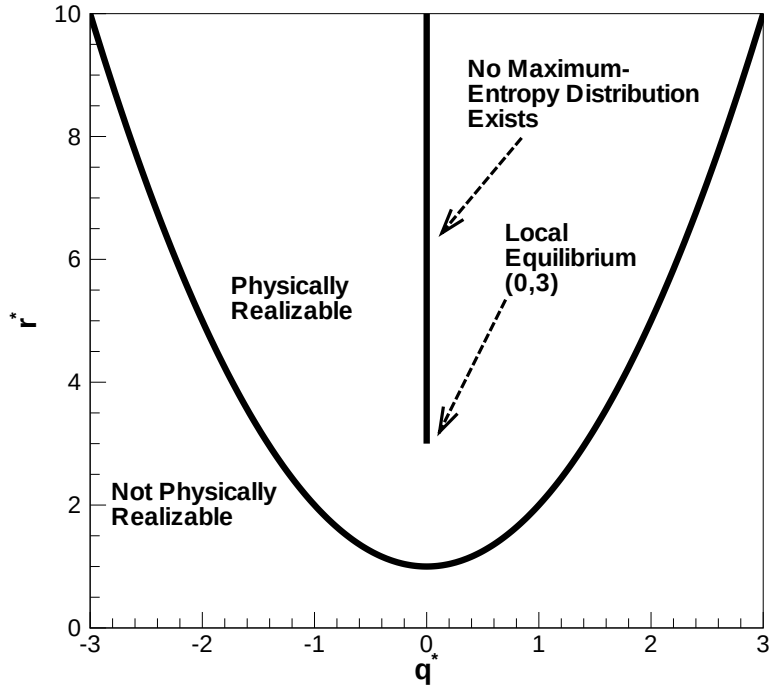

Figure 7.1: Region of physical realizability and realizability of maximum-entropy distribution function for the one-dimensional 5-moment system.

for all higher-order moment closures, the equilibrium state lies on the boundary in moment space separating regions in which the entropy maximization problem can be solved and regions in which a solution is not possible [29]. This seems to leave little hope that numerical solutions to moment closure problems can be computed for any practical situations.

Investigation of the behaviour of the non-dimensional closing flux, $s^\star$, as a function of $q^\star$ and $r^\star$ shows the practical nature of the problem of realizability for this 5-moment system. The closure is not defined on the line extending upward from the point $(0, 3)$. It can be seen in figure 7.2 that as this line is approached from either the left or the right, the closing flux diverges quickly towards negative of positive infinity respectively. For practical use of higher-order moment closures, it is not only the mathematical problem of realizability which must be overcome as even in realizable regions, the flux becomes arbitrarily large and could never be computed using finite-precision arithmetic. This issue could be referred to as a problem of numerical realizability.

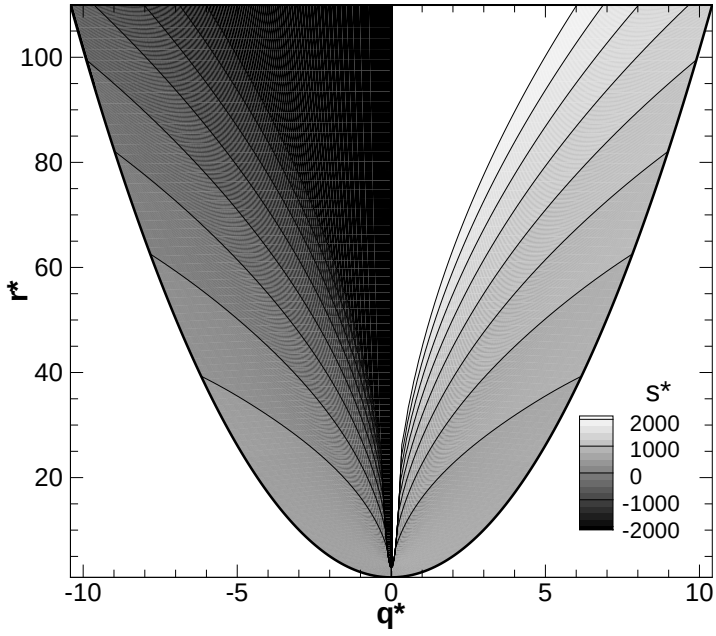

Figure 7.2: Non-dimensionalized closing flux $s^\star$ for the one-dimensional, 5-moment, maximum-entropy closure.

7.5 Realizable Distribution Functions

One possible technique to avoid issues with non-realizability of maximum-entropy closures that is explored herein is to modify slightly the assumed form for the distribution function. This can be accomplished by adding an additional term or factor, σ, to the exponential of equation 3.6 to yield

$$\mathcal{F}^{(N)} = e^{\left(\boldsymbol{\alpha}^{(N)\mathrm{T}}\mathbf{V}^{(N)}+\sigma\right)} = e^{\left(\boldsymbol{\alpha}^{(N)\mathrm{T}}\mathbf{V}^{(N)}\right)} f_w \,, \tag{7.40}$$

where $f_w = e^{\sigma}$. This type of modification to the maximum-entropy moment distribution was first proposed by Au [95] and then later re-considered by Junk [96]. The modification is equivalent to multiplying the distribution function by a factor f_w. This factor can be viewed as a "window" function that attenuates the distribution at high velocities, thus ensuring the distribution remains finite. In general, σ is a velocity-dependent term that must be chosen such that it approaches negative infinity more quickly than the polynomial, $\boldsymbol{\alpha}^{(N)\mathrm{T}}\mathbf{V}^{(N)}$, can approach positive infinity as $|v_i|$ becomes large in any direction. This allows the closure to remain valid for all physically realizable sets of velocity moments.

In the case that σ is not a function of the closure coefficients, proof of hyperbolicity as described in chapter 3 remains valid and the hyperbolic properties of the moment closure are retained. A simple example where this is true is to take $\sigma = -b|v_i|^n$ where b is a positive real value and n is an even integer larger than the highest power of the velocity weights in $\mathbf{V}^{(N)}$. In this case, $\partial\sigma/\partial\boldsymbol{\alpha}^{(N)} = 0$ and the proof of hyperbolicity remains entirely unaltered. Unfortunately, for velocity-weight vectors in the Levermore hierarchy, the closure is no-longer Galilean invariant for this choice of σ. Taking $\sigma = -b|c_i|^n$ leads to a Galilean-invariant closure; however, in this case, $\partial\sigma/\boldsymbol{\alpha} \neq 0$ and hyperbolicity of the closure is not assured. This is because it is no longer possible to ensure in a general manner that $h_{\boldsymbol{\alpha}\boldsymbol{\alpha}}$ is symmetric positive definite.

In practise, it would seem prudent to define σ to be a function of the local solution so as to ensure Galilean invariance of the closure. Moreover, it has been found that it is also desirable to have the effective width of the window function, σ, be dependent on the solution so as to match the standard deviation of the unmodified distribution in some fashion and thereby result in a more appropriate windowing function. In the current work, the modification to the maximum-entropy distribution is chosen to have the form

$$\sigma = -b\left(\frac{\rho}{p}\right)^{\frac{L+2}{2}} |c_i|^{L+2}\,, \tag{7.41}$$

where L is the highest exponent of the velocity weights used in the moment closure and b is some specified positive number. This form for σ clearly makes strict proof of hyperbolicity elusive; however, it can be shown through numerical experiments that the resulting moment equations are well behaved and remain hyperbolic for a wide range of flow conditions.

One cause for concern with this proposed approach may be its treatment of equilibrium conditions as the modified distribution function no longer contains the Maxwellian. Nevertheless, under equilibrium conditions, the moments of the modified distribution function used in the closure are in full agreement with those of the Maxwellian up to one order higher than the order of the closure provided that the velocity weights of the Levermore hierarchy are used. In addition, all odd-order random velocity moments of the modified assumed-form for the distribution function vanish and are equal to those of the Maxwellian under equilibrium conditions.

It should be noted that with the introduction of the window function no longer requires the strict use of the velocity weights, $\mathbf{V}^{(N)}$ or $\mathbf{C}^{(N)}$, proposed in the Levermore

hierarchy as the window function must be used to ensure that the distribution approximate function remains finite regardless of the velocity weights. Other choices are therefore possible for the velocity moments of the closure while still remaining both realizable and hyperbolic [96].

7.5.1 Alternate Remedies for Non-Realizability

Recently, Schneider [30, 31] has proposed an alternate approach to dealing with the realizability of maximum-entropy closures. He proposes appropriately relaxing some of the equality constraints on the moments in the entropy minimization procedure when defining the maximum-entropy distribution. This leads to a maximum-entropy solution; however, it is one that does not satisfy the full set of predicted moments (only those that can be satisfied and represented by the maximum-entropy distribution). Hauck *et al.* [31] have subsequently carried out a thorough mathematical analysis of this alternate approach to modifying maximum-entropy closures.

Mathematically, this approach does preserve hyperbolicity while leading to universally realizable closures. However, there remain practical issues that are not resolved. The new closure is modified only in the area where the traditional closure is non-realizable; all other regions are unaltered. Referring to figure 7.2, it is clear that even in regions where the maximum-entropy distribution function exists, there are areas where practical computation of the closing flux will be problematic. In fact, the closing flux still approaches infinity as the problematic line is approached and there are regions arbitrarily close to equilibrium where the closing flux is arbitrarily large.

7.5.2 Application to One-Dimensional 5-Moment System

The application of the windowing technique shown above is now considered for the one-dimensional 5-moment system. The resulting distribution function is

$$\mathcal{F}^{(5)} = e^{\alpha_0+\alpha_1 c+\alpha_2 c^2+\alpha_3 c^3+\alpha_4 c^4-b(\rho/p)^3 c^6} = e^{\alpha_0+\alpha_1 c+\alpha_2 c^2+\alpha_3 c^3+\alpha_4 c^4} e^{-b(\rho/p)^3 c^6}, \qquad (7.42)$$

where $f_w = e^{-b(\rho/p)^3 c^6}$ is the window function. The parameter b can be adjusted to modify the effective width of the window. For $b=0$, the maximum-entropy closure is recovered. Figure 7.3 shows the numerical computation of $s^\star$ as predicted by the new closure for a wide range of physically realizable situations for $b = 10^{-4}$ and $b = 10^{-5}$. For these two values of b, the modified realizable distribution function fully spans the region in $q^\star$-$r^\star$

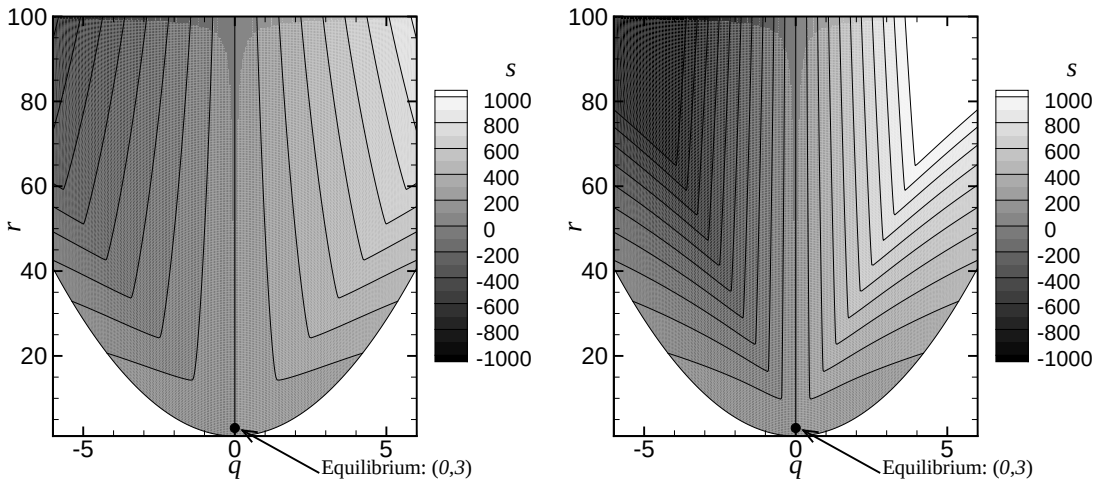

Figure 7.3: Predicted fifth-order non-dimensional random-velocity moment, $s^\star$, as a function of $q^\star$ and $r^\star$ for the 5-moment one-dimensional realizable moment closure with (a) $b=10^{-4}$; and (b) $b=10^{-5}$.

space of all physically realizable moments and values for $s^\star$ are computable. In fact, the proposed closure is realizable for all positive non-zero values of b. It is interesting to note that $s^\star$ does not appear to be a smooth function of $q^\star$ and $r^\star$ as indicated by the sharp changes in the contour lines.

From figure 7.3, it is evident that the modification to the maximum-entropy distribution function has resulted in a moment closure which covers the whole realizable moment space; however, formal proof of global hyperbolicity is not possible in this case. Hyperbolicity of the proposed closure is instead investigated numerically. The flux Jacobians are computed numerically using a second-order accurate centred finite-difference technique. Eigenvalues of the Jacobians are then computed numerically. The system of moment equations is deemed hyperbolic whenever the eigenvalues are real. Figure 7.4 shows the largest imaginary part of the computed eigenvalues as a function of $q^\star$ and $r^\star$ for the normalized distribution function, again for the cases where $b=10^{-4}$ and $b=10^{-5}$. The computed eigenvalues do not remain real, and hence, the system is not globally hyperbolic. Fortunately, as b decreases, the region of hyperbolicity expands greatly. It should be obvious that for $b=0$ the closure will be hyperbolic but not realizable and as b is increased the closure is now realizable but the region of hyperbolicity is reduced and does not span the full range of realizable moments. This points to a trade-off in the

selection of the realizability parameter b: it must be non-zero and large enough so that all moments are numerically integrable (numerically realizable) but sufficiently small so that the closure remains hyperbolic for the non-equilibrium flow conditions of interest.

In order to gain a feel for the degree of non-equilibrium behaviour which is contained in the hyperbolic region, the orbits of moments describing the structure of shock waves with shock Mach numbers of 2, 4, and 8 as predicted by a high-resolution numerical solution of the BGK kinetic equation (equation 7.1) are shown in both figures 7.4(a) and 7.4(b). The orbit corresponding to a shock with an upstream Mach number of 2 is quite small as compared to that of the stronger shocks. It can be observed that, if b is taken to be 10^{-5}, even the relatively high shock-Mach-number case remains in the hyperbolic region. The appearance of complex eigenvalues along the line across which $s^\star$ seems to be a non-smooth function of $q^\star$ and $r^\star$ is most likely due to the unsuitability of finite differences across this line. The hyperbolic nature of the closure and its moment equations is difficult to evaluate on this line.

7.5.3 Godunov-Type Finite-Volume Scheme

As a preliminary investigation of the predictive capability offered by the proposed higher-order realizable hyperbolic moment equations, a numerical solution procedure has been constructed for the one-dimensional moment system described above. The moment equations are solved using a Godunov-type finite-volume scheme. The HLL [97] approximate Riemann solver is used to evaluate inter-cellular fluxes, for which estimates for the maximum and minimum wave speeds are based on the numerical evaluation of the eigenvalues of an approximate flux Jacobian for the moment closure. Higher-order accuracy is achieved through piecewise limited linear reconstruction and a point-implicit predictor-corrector time-marching scheme is again used to advance the solution [14].

As stated earlier, for the 5-moment closure there is no explicit conversion from conserved moments, $\mathbf{U}^{(N)}$, to the closure coefficients, $\boldsymbol{\alpha}^{(N)}$. The evaluation of the highest-order flux requires that all of the coefficients be known at each time step. These coefficients can be determined by finding the solution to equation 3.25 with the modified distribution function used to define a modified density potential. This leads to a minimization problem given by

$$\mathcal{S}(\mathbf{U}^{(N)}) = -\min_{\boldsymbol{\alpha}^{(N)}} \left[< \exp\left(\boldsymbol{\alpha}^{\mathrm{T}}\mathbf{V}^{(N)} + \sigma\right) > - \boldsymbol{\alpha}^{\mathrm{T}}\mathbf{U}^{(N)} \right] . \tag{7.43}$$

Although the resulting solution from the minimization of the functional given in equation 7.43 above is no longer the mathematical entropy and the corresponding distribution function is not the maximum-entropy distribution, the minimization process still defines the relationship between the predicted moments and closure coefficients. As this function can be shown to be convex, the minimization problem can be solved using an approximate Newton's method. In some cases, it is possible for the computed update from Newton's method to move the vector $\boldsymbol{\alpha}^{(N)}$ to a location where numerical integration of the moments is not possible. When this happens, a simple back-tracking technique is used to step back into a computable region of moment space.

This technique for synchronization of $\boldsymbol{\alpha}^{(N)}$ and $\mathbf{U}^{(N)}$ involves many numerical integrations of the velocity distribution function and is quite computationally expensive compared to the other elements of the one-dimensional flow solver. A technique to reduce the number of re-synchronizations required is therefore very desirable. One possibility is to again make use of the Hessian of the density potential, $\partial^2 h/\partial\boldsymbol{\alpha}^2 = \partial\boldsymbol{U}/\partial\boldsymbol{\alpha}$ to update the closure coefficients after each time step by exploiting the relationship

$$\Delta\boldsymbol{\alpha} = \left(\frac{\partial\mathbf{U}}{\partial\boldsymbol{\alpha}}\right)^{-1}\Delta\mathbf{U}\,. \tag{7.44}$$

If this update of the coefficients is sufficiently accurate, re-synchronization of $\boldsymbol{\alpha}$ in terms of $\mathbf{U}$ may not be required, thus greatly reducing the cost of the scheme. However, determining the effectiveness of this simplified update and deciding when a full re-synchronization is required can be somewhat difficult. One possibility is to apply the simple update above and integrate one velocity moment and compare it to the target value. A large deviation in the two values can be used as a trigger for a costly re-synchronization.

7.5.4 Numerical Results for Stationary Shocks

Predictions of the structure of stationary shocks for the one-dimensional gas obtained by solving the 5-moment version of the physically-realizable moment equations are now considered. The numerical results are shown in figure 7.5 and compared with numerical solutions to the equivalent Navier-Stokes-like equations given previously for a range of shock Mach numbers. Due to the expense of solving the re-synchronization problem, it was only affordable to use a grid in physical space comprising 300 volumes, however this resolution seems to give good results. High-resolution numerical solutions of the one-dimensional BGK kinetic equation for this one-dimensional gas are also depicted

for comparison. The discrete-velocity method of Mieussens [4] is used to obtain the numerical solution of the one-dimensional kinetic equation with a region of velocity space stretching from $-5,000$ m/s to $5,000$ m/s discretized into 500 equally spaced points. It can plainly be observed that the 5-moment system is in much better agreement with the BGK solution than the Navier-Stokes-like solution. As with all hyperbolic systems, a discontinuity appears in the moment solution when the incoming flow speed exceeds the maximum wavespeed in the system. In this case, however, the size of the jump is very small. This is in contrast to many other moment-closure predictions of shock structure where the size of the discontinuity tends to grow with the shock Mach number and quickly dominates the profile.

7.5.5 Numerical Results for the Riemann Problem

In order to explore further the behaviour of the modified 5-moment closure across a range of Knudsen numbers, a Riemann initial-value problem is considered. The case of interest consists of a two-state initial condition with a pressure ratio of 2.5 and a density ratio of 2. Three different situations were examined corresponding to Knudsen numbers of 2.3×10^{-5}, 2.3×10^{-2}, and 23, thus spanning the continuum, transition, and free-molecular flow regimes. Again, a computational grid of 300 volumes is used. The resulting solutions are shown in figure 7.6. Here the 5-moment system is compared to the 3-moment closure (which is equivalent to the Euler equations for a one-dimensional gas), high-resolution numerical solutions of the BGK kinetic equation, and numerical solution of the equivalent Navier-Stokes-like equations. All of which were described above. Again, the discrete-velocity method of Mieussens [4] is used to obtain the kinetic solutions now with a resolution of 200 points stretching from $-2,000$ m/s to $2,000$ m/s.

It can be seen in figures 7.6(a) and 7.6(b) that, in the continuum regime, all three non-equilibrium solutions treatments are in close agreement with the equivalent Euler-like equations for this one-dimensional gas. On this scale of interest, the regions of the flow which are not in local thermodynamic equilibrium are much smaller than the domain of interest and are generally not resolved.

Figures 7.6(c) and 7.6(d) depicts the numerical results for the transition regime, lying somewhere between continuum and free-molecular results. In this regime, the 3-moment model, which can only correctly account for flows in thermodynamic equilibrium, gives an identical solution, although on a different scale, to that found for the continuum

regime. The non-equilibrium solutions of the 5-moment model, Navier-Stokes equations, and BGK equation on this scale are all still quite similar to each other in this case, but are now quite distinct from the equilibrium or equivalent Euler-like result. For the non-equilibrium solutions, the wave structures that appear as discrete near discontinuities in the continuum situation are still identifiable but are now quite diffuse and approach one another such that they interact, yielding a solution with a smooth transition between the two constant initial states at either end of the solution domain.

The free-molecular results for the Riemann initial-value problem are given in figure 7.6(e) and 7.6(f). For this case, the 3-moment model again yields results that are the same as those for the continuum flow solution. For the modified 5-moment model, due to infrequent inter-particle collisions, the terms associated with the collision operator have now become so insignificant that the moment closure essentially behaves as a purely hyperbolic system without relaxation. It yields a solution with five distinct waves separated by essentially constant solution states. This non-equilibrium result is in contrast to the BGK kinetic equation solution, which consists of a single smooth transition between the two constant initial states, with no clearly identifiable wave structure. The agreement between 5-moment closure solution and the exact or BGK kinetic solution is certainly not very good in this case, indicating that, while it is still possible to obtain solutions, there is an upper bound on the Knudsen number for which the 5-moment model remains physically valid. Higher-order moment closures would be needed to improve on this result. For this highly rarefied case, the speed with which significant heat-transfer effects are carried in the Navier-Stokes case is over predicted and is so high that any temperature differences are smoothed out extremely rapidly. These thermal effects move so quickly relative to the hyperbolic components of the equations that they impact the boundary of the computational domain almost immediately and therefore boundary conditions play an important role; in this case a zero-derivative Neumann boundary condition was used for all variables. Regardless of which boundary condition is used, the speed at which temperature differences are diffused away leads the Navier-Stokes-like equations to predict solutions that approach the solution to the isothermal Euler solution. This is why a two-wave solution is predicted in this case.

7.6 Closed-Form Approximation to a Maximum-Entropy Moment Closure

As stated earlier, one of the major stumbling blocks to the adoption of maximum-entropy-based moment closures is the lack of a closed-form expression for closing moment fluxes. It will now be shown that a simple surface fit can provide an adequate approximation to the true maximum-entropy 5-moment closure above, equations 7.30–7.34. By using a fit in this manner, the complexity and expense of moment and distribution function resynchronization can be avoided. Numerical-solution costs are therefore reduced by orders of magnitude. Moreover, and somewhat serendipitously, this fit will also avoid the problem of non realizability of the true maximum-entropy closure.

Firstly, it should be noted that along the line defining the envelope of the region of physical realizability, $r^\star = 1 + (q^\star)^2$, the distribution function is comprised of two delta functions. On this line the closing relationship can be easily found analytically and is $s^\star = (q^\star)^3 + 2q^\star$. Next, realizing that the region of realizability is parabolic, it seems sensible to parametrize this space using a parabolic transformation of the form given by

$$r^\star = \frac{2(q^\star)^2}{\sigma} + 3 - \sigma \quad \text{with} \quad 0 \leq \sigma \leq 2 \,. \tag{7.45}$$

For this mapping, lines of constant σ are parabolas and σ is the distance down from local equilibrium, $r^\star = 3$, that these lines intersect the $r^\star$ axis. These parabolas have curvatures that increase from $\sigma = 2$, where the parabola coincides with the limit of physical realizability, to $\sigma = 0$ where the parabola collapses to the line $q^\star = 0$ and $r^\star \geq 3$, thus covering the entire realizable region.

It was found through numerical experimentation that along the lines of constant σ the moment $s^\star$ can be well approximated by a cubic function of $q^\star$ as $s^\star = p_3(\sigma)(q^\star)^3 + p_1(\sigma)q^\star$. The functions $p_3(\sigma)$ and $p_1(\sigma)$ must be fit by first numerically finding finite difference approximations to these derivatives along the line $q^\star = 0$ and $1 \leq r^\star \leq 3$. These data points are then fit using standard fitting software; it has been found that these functions are well approximated as

$$p_1 = a_1 + b_1\sigma + c_1\sigma^2 + d_1\sigma^3 + e_1\sigma^4 + f_1\sigma^5 + g_1\sigma^6 \,, \tag{7.46}$$

with

$$\begin{array}{rclrcl} a_1 &=& 9.9679007422678190 & e_1 &=& 4.3920303941514343 \\ b_1 &=& -9.234367231975216 & f_1 &=& -1.452821303578764 \\ c_1 &=& 8.2142492688404296 & g_1 &=& 0.2006200057926356 \\ d_1 &=& -7.372320367163680 & & & \end{array} ,$$

and

$$p_3 = \frac{a_3 + b_3\sigma + c_3\sigma^2 + d_3\sigma^3}{1 + e_3\sigma + f_3\sigma^2 + g_3\sigma^3} , \tag{7.47}$$

with

$$\begin{array}{rclrcl} a_3 &=& -20840.93761193234 & e_3 &=& -1077.797102997202 \\ b_3 &=& 7937.3772948278038 & f_3 &=& -3072.303291055466 \\ c_3 &=& 405.05250560053173 & g_3 &=& 1056.0890741355661 \\ d_3 &=& -329.3827765656151 & & & \end{array} .$$

Having determined the fits above, the closing flux is expressible as a closed form function of $q^\star$ and $r^\star$.

7.6.1 Accuracy of Fit and Hyperbolicity

Figures 7.7(a) and 7.7(b) show the non-dimensionalized closing flux, $s^\star$ of the 5-moment maximum entropy system as well as the surface fit shown above. The relative error is plotted in figure 7.6.1. It can be seen that away from the line on which the maximum-entropy distribution does not exist and the predicted flux is singular, the fit is quite good. In practise, the fact that the fit does not approximate the singularity well is actually advantageous as the fit transitions smoothly across the $r^\star$ axis and numerical overflow is avoided.

Once again, there is no formal proof of hyperbolicity when this surface fit is used for the closing flux. However, experience gained from numerical calculation of many flows using this fit suggests that non-hyperbolicity does not seem to be an issue for a wide range of conditions.

7.7 Numerical Calculations of Shock Structures

As a preliminary investigation into the behaviour of the fitted moment closure, shock waves of Mach numbers 2, 4, and 8 are again considered. Once again, the same Godunov-type finite-volume scheme is used. The costly re-synchronization step is now unnecessary

as the closing flux is known as a function of the known moments. A computational mesh with $5,000$ volumes can now easily be used to ensure a solution that is entirely grid-converged. Eigenvalues must still be determined in order to use the HLL flux function; these are found numerically using the analytic flux Jacobian.

Comparisons are once again made to high-resolution simulation of the kinetic equation, 2.8, with the same relaxation collision operator as was used in the moment equations [36] and with the equivalent Navier-Stokes-like equations for this situation. Figures 7.9(a), 7.9(c), and 7.9(e) show normalized density profiles for shocks with a Mach number of 2, 4, and 8 respectively, while normalized heat transfer is shown in figures 7.9(b), 7.9(d), and 7.9(f).

It can be seen that agreement between the moment equations and the BGK equation is again very good, far better than the Navier-Stokes-like equations. The profiles predicted by the surface fit are almost identical to the profiles predicted by the modified, realizable, 5-moment system of section 7.5. The same relatively small discontinuities in the shock profile are again present. Figure 7.6.1 shows the orbits traced by these shock profiles in the $\hat{q}$-$\hat{r}$ plane. All shocks begin at equilibrium, jump to a non-equilibrium state across the discontinuity, and return smoothly to equilibrium. It can be seen that in all cases, the area of largest relative error in the fit is avoided.

7.8 Riemann Problem

Finally, the 5-moment closure fit it used for the computation of the Riemann problem of section 7.5.5. For this case a computational mesh comprising $3,000$ cells was used. The results are shown in figure 7.10. One again, solutions are almost identical to those obtained with the modified, realizable, 5-moment closure. The same transition from a three-wave equilibrium solution through a diffuse smooth transition into a 5-wave non equilibrium solution is observed. The only difference in solution that is noticeable to the eye is in the heat-flux prediction for the free-molecular case (figures 7.6(f) and 7.10(f)). These solutions, however, are obtained in orders of magnitude less time than the previous calculations with the costly re-synchronizations of moments and closure coefficients.

7.9 Remarks Regarding Computational Cost

The computational expense of the different techniques considered in this chapter varied widely. Although real effort has been made to optimize the solution methods or computer implementations of the techniques, it is felt that some remarks on computational cost are warranted.

The numerical solution of the kinetic equation for most of the problems above required multiple days on a single CPU. Such computations for a realistic three-dimensional gas would require huge resources. For example, if the same resolution in velocity space was used in three space dimensions as was used for the shock-structure calculations above, the solution vector in each cell would have over a hundred million entries! This is clearly not an attractive option.

The prospects for the moment closure based on a realizable distribution function shown above are not much better. Computation of the presented shock-structures solutions took more than a day on a single CPU. The extension to a three-dimensional gas would require the integration of distribution functions which would now exist in three dimensions. A similar curse of dimensionality that afflicts the kinetic method also affects this method. For any physically realistic cases the re-synchronization procedure would be prohibitively expensive.

The surface-fit closure does offer much more affordable option. The computations carried out above only took several minutes. Moreover, the extension of this method to a realistic three-dimensional gas does not need to bring the same devastating cost increase as either the kinetic method or the method based on realizable distribution functions. The simplest three-dimensional equivalent to the maximum-entropy 5-moment system shown above is a 14-moment system. Closing fluxes would therefore have to be fit in a higher-dimensional space, but not by orders of magnitude.

The time required for the Navier-Stokes-like computations varied based on the Knudsen number. For low-Knudsen-number cases computations were very fast and only took a matter of seconds. However, as the Knudsen number increases and length scales get relatively smaller, the time-step restriction required for stability of the calculation becomes very restrictive due to the partially elliptic nature of the equations.

Solution of the equilibrium 3-moment equations is far faster than all the other methods. However, with no treatment for non-equilibrium effects, the usefulness of these equations for practical problems involving any level of non-equilibrium is limited.

7.10 Observations

Although maximum-entropy-based moment closures are known to have several apparent disadvantages, including a lack of a closed-form expression for closing fluxes and regions of non-realizability, it has been demonstrated that these difficulties can be handled in practise, at least for some closures that contain heat transfer.

The preceding discussion has proposed a technique for the construction of realizable 5-moment moment closures. For this technique, the underlying distribution function is a modification of the maximum-entropy distribution function that ensures universal moment realizability for the entire range of physical validity. Global hyperbolicity has been lost, however through careful selection of the parameter b moments remain numerically realizable and the closure remains hyperbolic for a very wide range non-equilibrium behaviour. The technique leads to usable moment equations, however the cost of their numerical solution remains somewhat high. Numerical integration of distribution functions is costly, even for the one-dimensional case. For a true three-dimensional gas, the costs associated with the resynchronization procedure would be overwhelming. However, the numerical results for the one-dimensional case shown above show the promise of hyperbolic moment closures to provide very accurate prediction of non-equilibrium flows. If such closures are going to be used as a practical tool, more computationally affordable variants must be sought.

It has also been shown that, for this 5-moment system, a simple surface fit can provide equally good flow predictions for the cases considered. This includes predictions for highly non-equilibrium strong-shocks. Eigenvalues must still be obtained numerically, however the cost of using the surface fit remains orders of magnitude lower than the technique of using the modified, realizable distribution function with its costly re-synchronizations.

Extension of the methods considered here to a fully three-dimensional gas is however not necessarily simple. It is anticipated that the modified-distribution technique of section 7.5 will technically extend to three-dimensions. Nevertheless, the cost of the accurate numerical integration of multi-dimensional distribution functions required for the re-synchronization step is expected to be overwhelming.

If hyperbolic moment closures are to be affordable for large-scale, practical, multi-dimensional problems, closing fluxes should be expressible as a function of known moments. This was the case for the simple surface fit shown above. A three-dimensional extension of this technique would require the determination of an appropriate mapping

(similar to that in equation 7.45) after which closing fluxes can be fit easily; this mapping may not be obvious to find.

The main point that should be taken from this chapter is not a specific technique for the construction of hyperbolic high-order moment closures as such, but rather the promise that they offer for accurate and affordable flow predictions for a wide range of regimes.

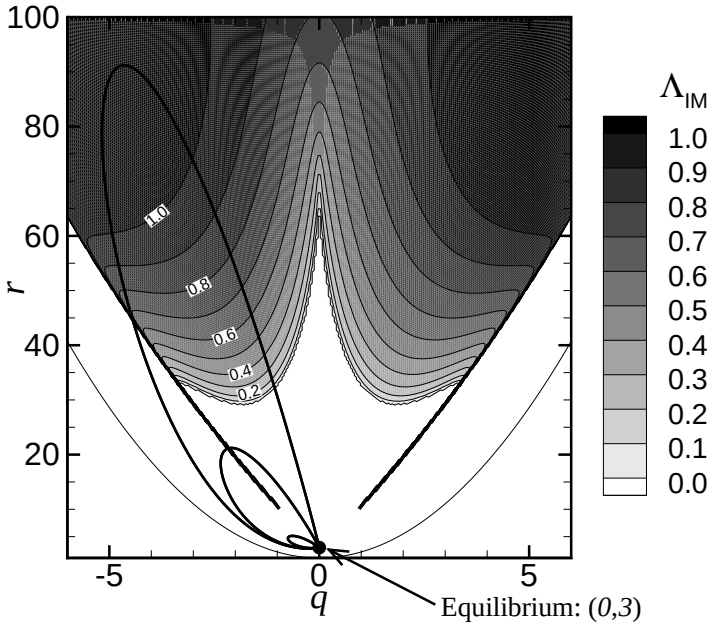

(a)

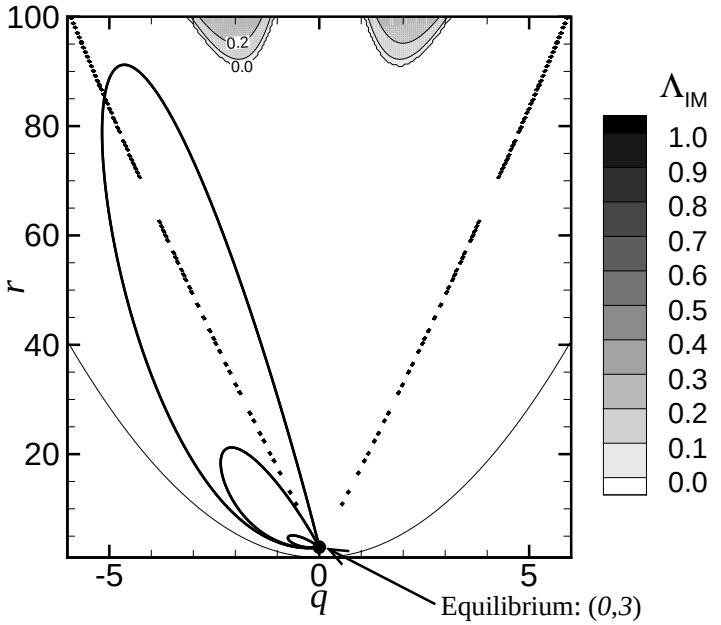

(b)

Figure 7.4: Largest imaginary part of the numerically determined eigenvalues of flux Jacobian for the modified, realizable, 5-moment moment closure with (a) $b = 10^{-4}$; and (b) $b = 10^{-5}$. The orbits of velocity moments corresponding the transition and internal structure for stationary shock wave solutions with shock Mach numbers of Ma = 2, Ma = 4, and Ma = 8 are also shown with the larger orbits corresponding to the higher shock Mach numbers.

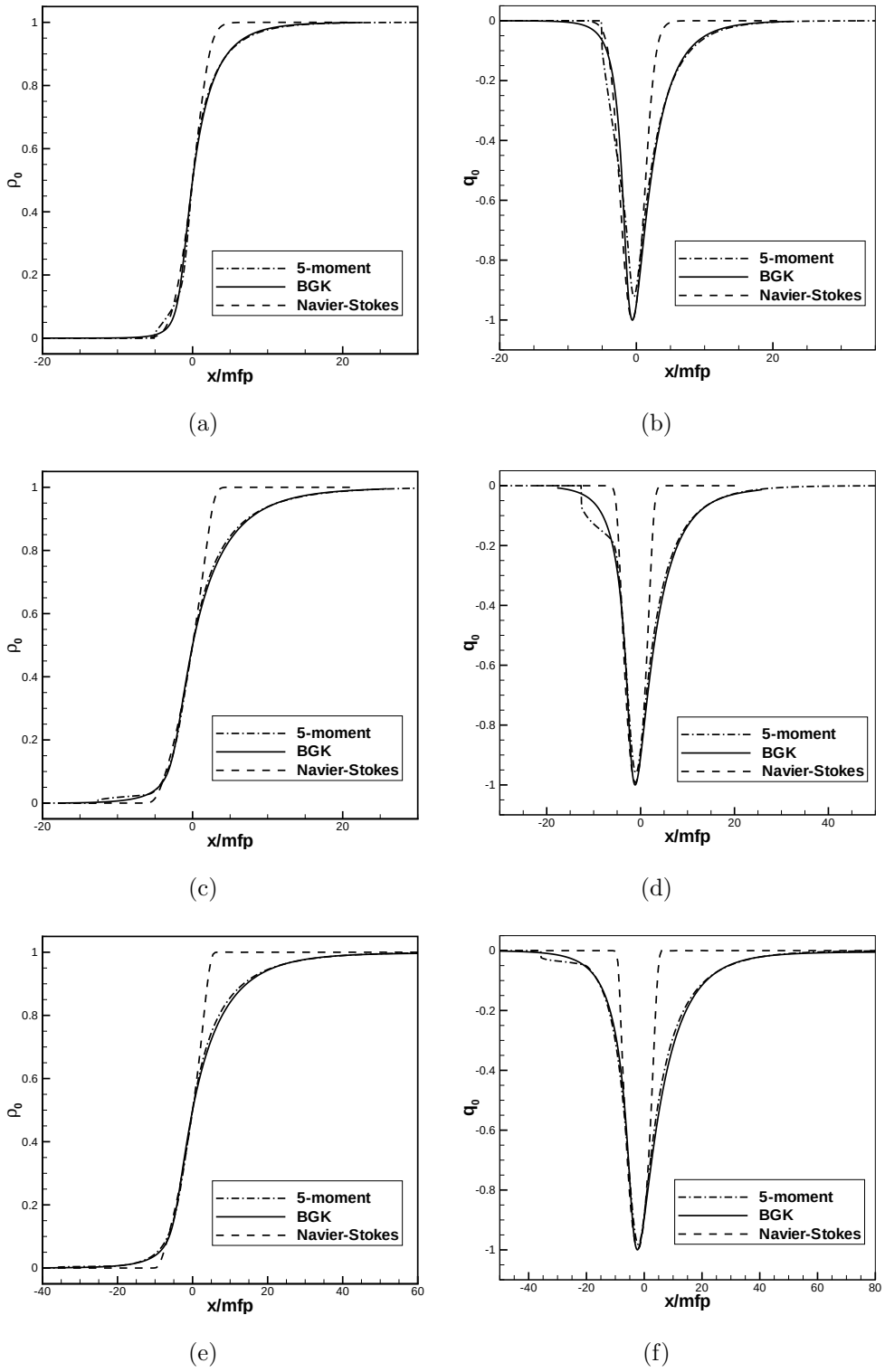

Figure 7.5: Predicted normalized density and heat-transfer through a stationary shock wave for a one-dimensional gas as determined using the modified, realizable, 5-moment closure. The predicted shock structure is compared to results obtained by the direct numerical solution of the BGK kinetic equation and Navier-Stokes-like equations for a range of shock Mach numbers, (a)–(b) Ma = 2; (c)–(d) Ma = 4; and (e)–(f) Ma = 8.

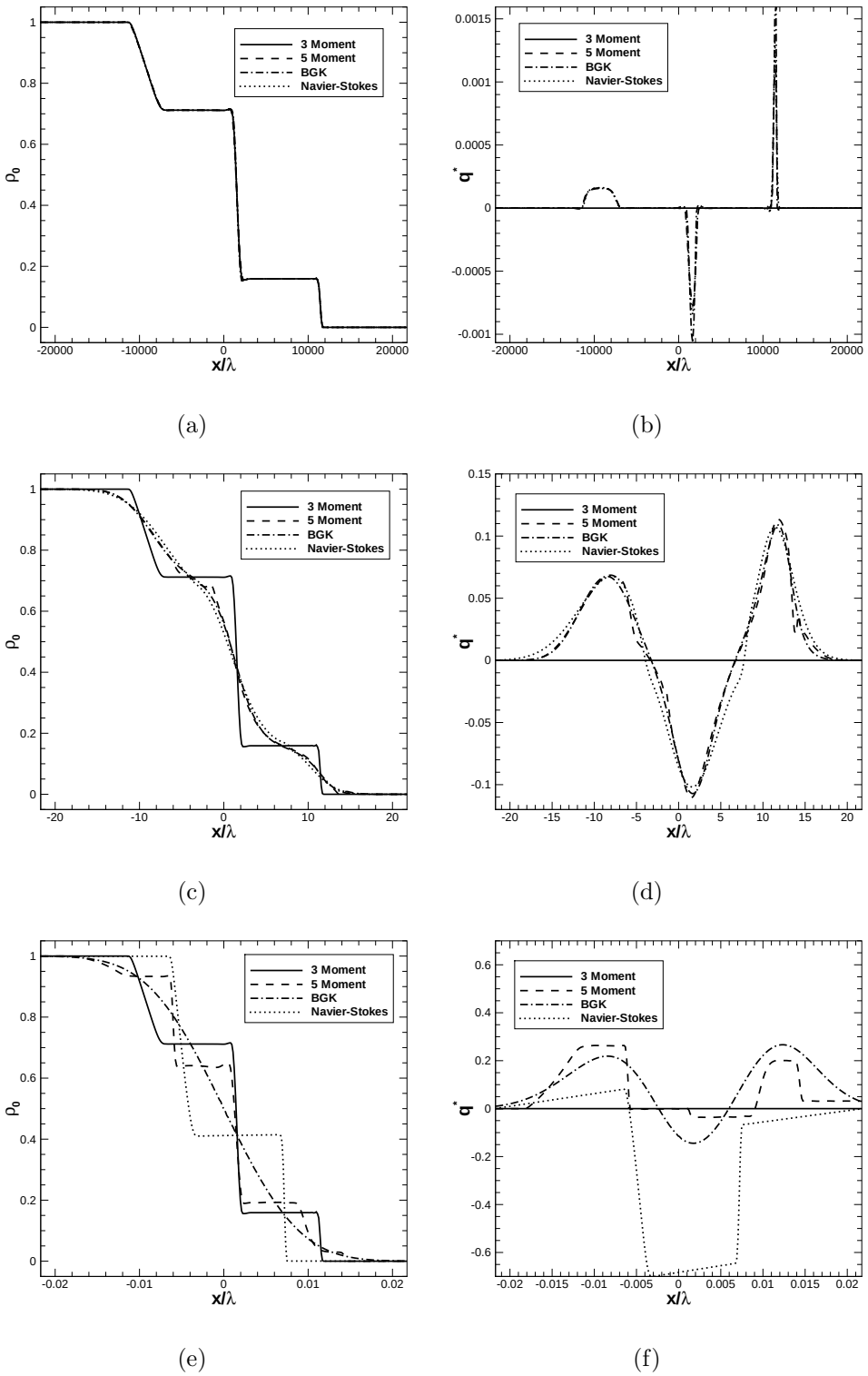

Figure 7.6: Predicted normalized density and heat flux for the Riemann initial-value problem as determined using the modified, realizable, 5-moment closure as compared to the equilibrium 3-moment closure, the kinetic equation, and the Navier-Stokes-like solutions for a range of Knudsen numbers: (a)–(b) $\mathrm{Kn} = 2.3\times10^{-5}$; (c)–(d) $\mathrm{Kn} = 2.3\times10^{-2}$; and (e)–(f) $\mathrm{Kn} = 23$.

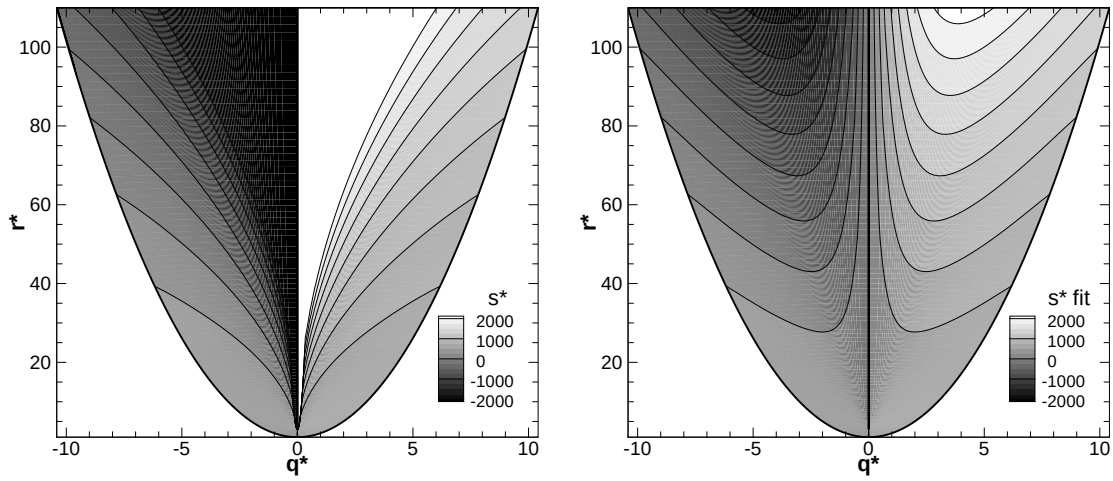

(a) (b)

Figure 7.7: (a) $s^\star$ predicted by maximum-entropy closure. (b) $s^\star$ predicted by surface fit.

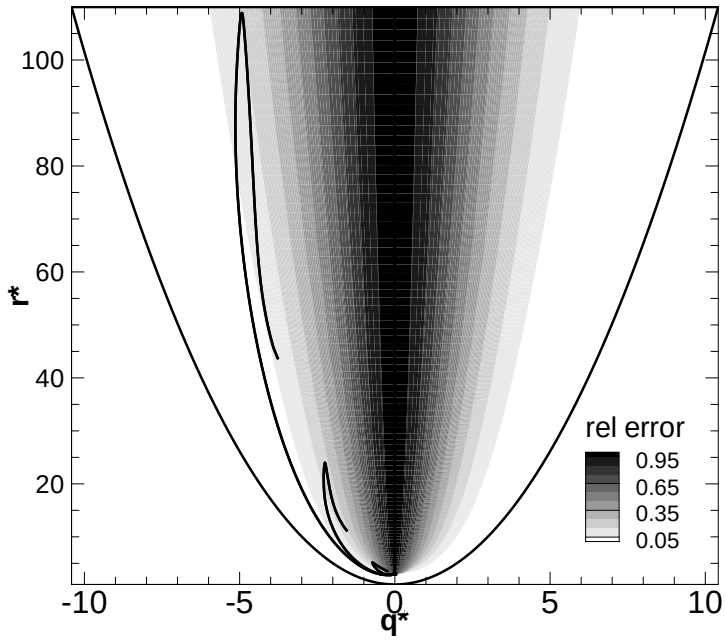

Figure 7.8: Relative error between fit and true moment $s^\star$ and orbits for shock waves with Mach numbers 2, 4, and 8.

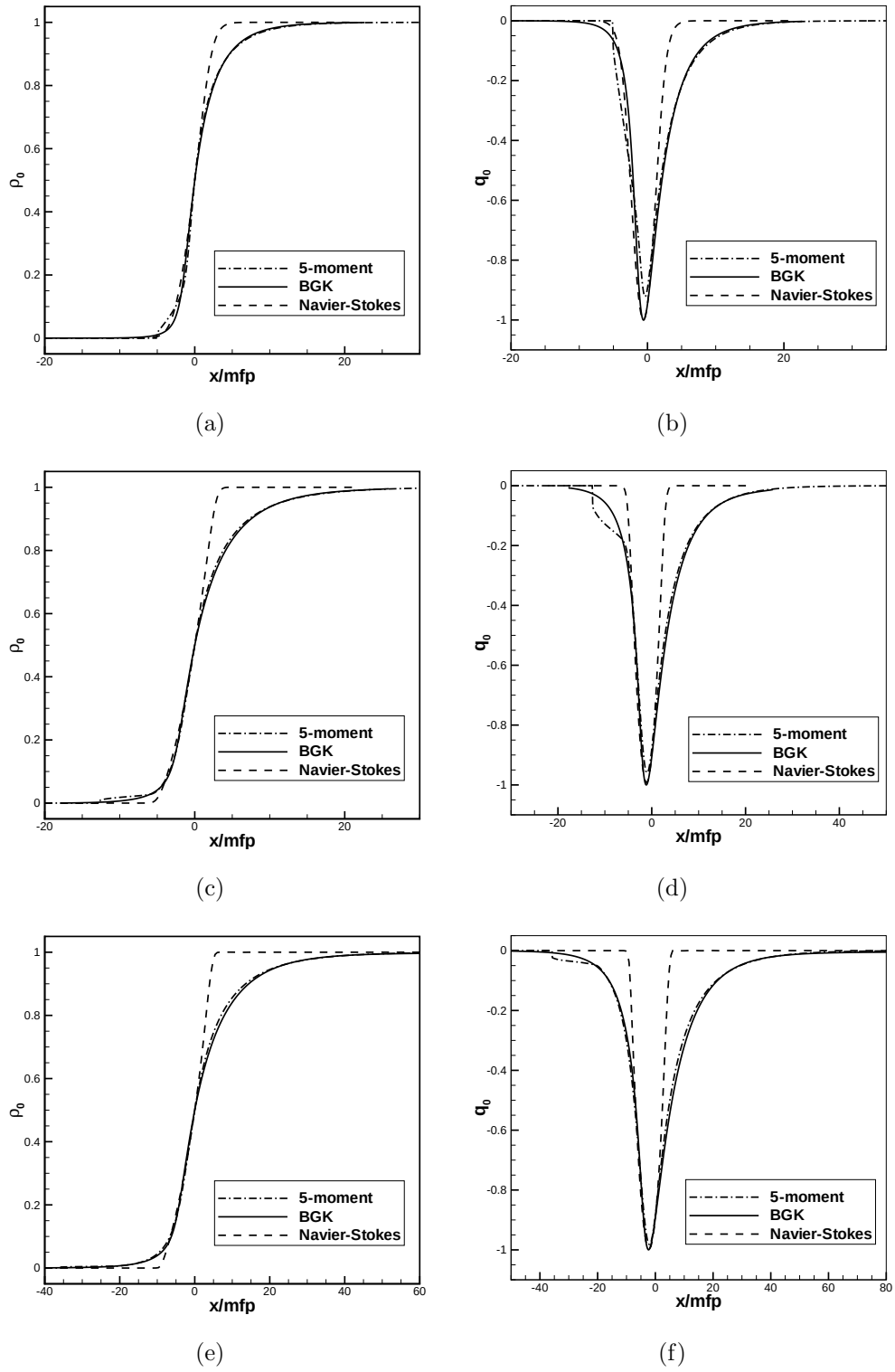

Figure 7.9: Predicted normalized density and heat-transfer through a stationary shock wave for a one-dimensional gas as determined using a surface fit for the closing flux of the maximum-entropy 5-moment closure. The predicted shock structure is compared to results obtained by the direct numerical solution of the BGK kinetic equation and Navier-Stokes-like equations for a range of shock Mach numbers (a)–(b) Ma = 2; (c)–(d) Ma = 4; and (e)–(f) Ma = 8.

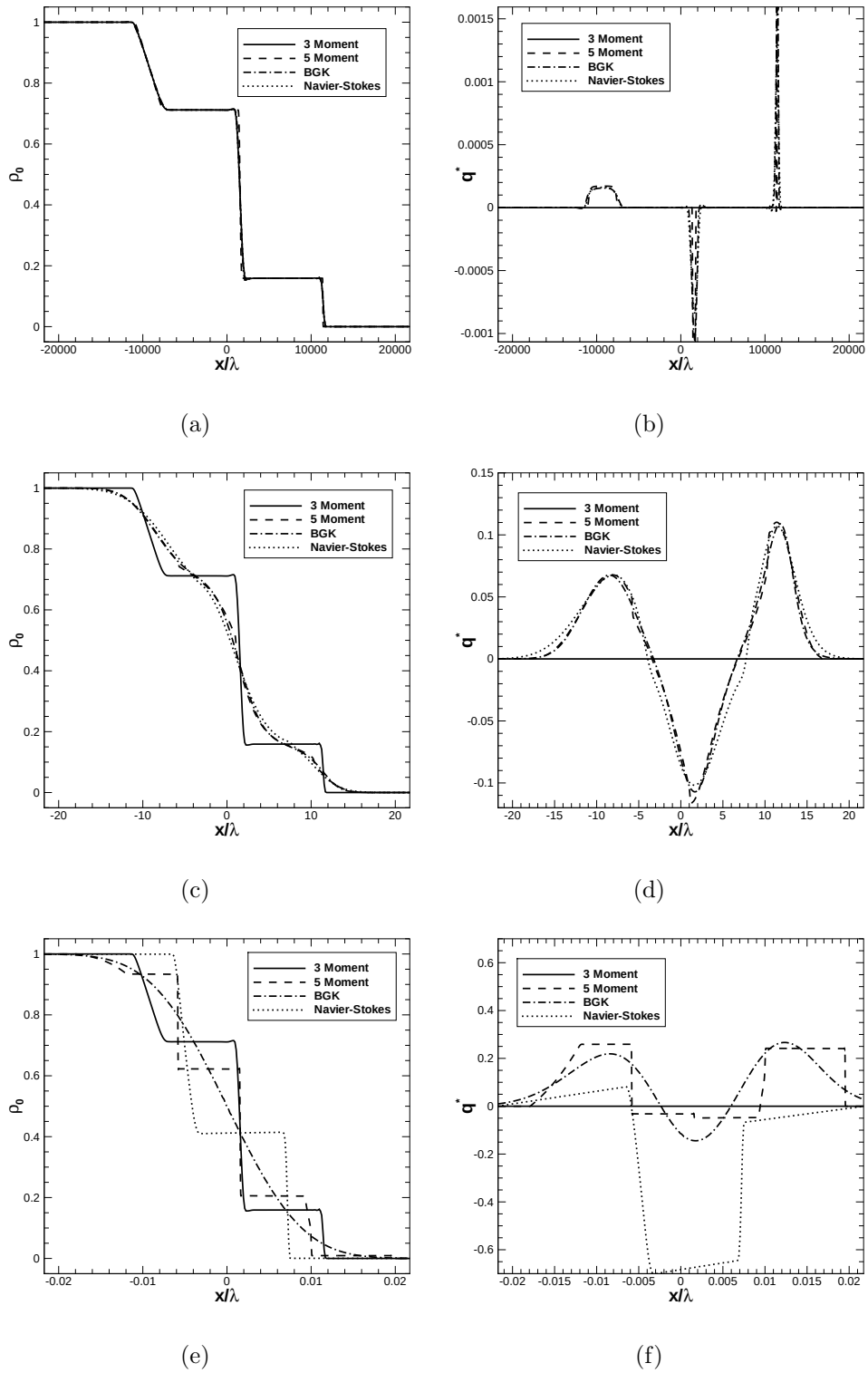

Figure 7.10: Predicted normalized density and heat flux for the Riemann initial-value problem as determined using a surface fit for the closing flux of the maximum-entropy 5-moment closure as compared to the equilibrium 3-moment closure, the kinetic equation, and the Navier-Stokes-like solutions for a range of Knudsen numbers: (a)–(b) Kn = 2.3×10^{-5}; (c)–(d) Kn = 2.3×10^{-2}; and (e)–(f) Kn = 23.

Chapter 8

Conclusions

This study has been concerned with the application of hyperbolic moment closures to viscous-gas flow prediction in and out of local thermodynamic equilibrium. Such non-equilibrium flows are common in many applications including micro-scale situations, highly rarefied flows and flows subjected to very strong gradients, such as those found in shock waves. It has been demonstrated that moment closures offer many advantages when compared to other techniques for gas flow prediction in these situations as well as in traditional continuum applications. Original contributions include:

- the construction of a two-dimensional Godunov-type finite-volume scheme for the solution of the Gaussian 10-moment model that allows for solution-directed adaptive mesh refinement and provides for efficient parallel solution using large-scale computational facilities,

- the first thorough exploration of the numerical solution of maxium-entropy moment closures for viscous gas-flow situations in and out of local thermodynamic-equilibrium for a large range of canonical flow problems,

- the implementation of a two-dimensional flow solver for the 10-moment method with a treatment for embedded possibly moving boundaries that are not aligned with the underlying computational mesh,

- the clear demonstration of moment closure's relative insensitivity to grid irregularities that result for the mesh-movement algorithm as compared to similar numerical solutions to the Navier-Stokes equations,

- the development of a novel set of regularized moment equations based on the Gaussian closure that provide a treatment for non-equilibrium heat transfer through the introduction of anisotropic thermal diffusion,
- the demonstration of the importance of heat-transfer for micro-scale flows through the numerical solution of the regularized 10-moment equations for a large set of flow problems,
- the development and numerical exploration of a set of one-dimensional higher-order hyperbolic moment equations with a treatment for heat transfer based on a realizable approximation to the maximum-entropy distribution,
- the development and numerical exploration of one-dimensional higher-order moment equations resulting from a curve fit for the closing flux of the true maximum-entropy closure.

The advantages that moment closures have can be divided into two types: mathematical advantages and modelling advantages. Mathematical advantages include properties of the continuous form of the moment equations, such as finite speeds of information propagation, and properties of discrete equations resulting from moment systems that make them more apt for numerical solution. Modelling advantages refers to the expanded range of physical validity that moment equations possess as compared to other fluid-dynamic equations.

In chapter 5, it was shown that the first-order nature of moment systems make them less susceptible to numerical difficulties when being solved on irregular meshes, such as those resulting from AMR or embedded-boundary treatments. A flow solver that makes use of a treatment for embedded, moving boundaries was constructed for the solution of the Gaussian, 10-moment equations. It was shown that the fact that the numerical solution of moment equations requires only the numerical evaluation of first derivatives leads to smooth solutions for fluid shear when the numerical solution of the Navier-Stokes equations leads to oscillations that are directly caused by irregularities in the numerical grid. Another mathematical advantage that was observed when seeking numerical solutions to both moment systems and the Navier-Stokes equations using explicit-time-marching techniques is a stability condition which is often less restrictive for the moment equations. Time-step restriction for purely hyperbolic systems is inversely proportional to the grid spacing whereas the restriction for the Navier-Stokes equations is proportional

to the inverse of the square of this distance; this is due to the nature of the elliptic terms present in the latter equations. The time-step-restriction advantage that the moment equations have becomes more and more obvious the higher the Knudsen number gets.

The Gaussian moment equations offer a hyperbolic treatment for compressible, viscous gas flow when there is no heat transfer and, as has been established in chapter 4, can be used reliably in situations when heat-transfer is not significant. Furthermore, highly scalable parallel and accurate solution of these moment equations are possible and the computational cost is not significantly more than performing a similar computation for solution of the Euler equations governing local equilibrium flow. Unfortunately for many applications, heat transfer plays an appreciable role. This is especially true for higher-Knudsen-number flows when heat-transfer can be significant even when temperature differences are very small. In chapter 6 a regularization technique for the 10-moment system was shown. This technique involves allowing the distribution function to deviate slightly from the Gaussian. Moment equations can then be derived either starting from the kinetic equation with appropriate collision operator or from the unmodified moment equations. This regularization results in the introduction of non-equilibrium heat-flux terms with and elliptic nature, thus the mathematical advantages furnished by purely hyperbolic equations is lost. In exchange for this loss of hyperbolicity, however, the modelling validity of the system is expanded through the introduction of the new terms. It was shown that, even for situations with small temperature variations, heat transfer plays an important role in many transition-regime flows. If any technique is going to provide reliable predictive capabilities in the transitions regime, it must therefore provide an accurate treatment for non-equilibrium heat-transfer.

Given the elegance and accuracy of the Gaussian closure to predict viscous, adiabatic, compressible flow, it would be most desirable if higher-order members of the Levermore hierarchy would provide a similarly straight-forward treatment for heat-conducting gas flows. As has been shown, this is unfortunately not the case. The lack of a closed-form expression for the moments of the maximum-entropy distribution function means that the closing flux cannot be expressed as a simple function of the moments in the solution vector. The result of this is an incredibly costly re-synchronization procedure to align the closure coefficients with the known moments that must be undertaken whenever a closing flux is needed during a computation. As was shown earlier, this is not the only impediment to the use of higher-order maximum-entropy moment systems. For all such closures of higher order than the Gaussian closure, there exist physically realistic moment

values for which the entropy-maximization problem cannot be solved. In these regions the entire mathematical framework of maximum-entropy moment closures breaks down. From a practical standpoint, it is not only the regions where the entropy-maximization problem does not have a mathematical solution that are an issue. It has been shown that even in regions where the solution technically exists numerical issue may prevent its solution. This is due to the fact that the closing flux can become arbitrarily large arbitrarily close to local equilibrium. Any practical solution to the issue of non-realizability must therefore not only address regions where the distribution function is mathematically non-realizable, but also regions where it cannot be realized numerically using finite-precision mathematics.

These impediments to the adoption of higher-order maximum-entropy moment closure were explored in chapter 7. As well, two novel possible solutions were proposed. It was shown that by making a small alteration to the underlying distribution function, a moment closure that is globally realizable can result. However, this alteration results in sacrificing universal hyperbolicity and regions where the eigenvalues of the flux Jacobian are not real are the result. It was shown that by carefully selection of the modification to the distribution, the region of hyperbolicity can be made large enough to encompass highly non-equilibrium effects while maintaining numerical realizability. Very good agreement between the new closure and high-resolution solution of the corresponding kinetic equation was demonstrated for a one-dimensional 5-moment system, even for high-Mach-number shock-structure calculations. The numerical solution of these closures remains expensive however. The modification that has provided realizability does not provide a closed-form expression for closing fluxes. These fluxes must therefore be determined through an expensive iterative procedure requiring many numerical integrations; this procedure would be prohibitively expensive for the general three-dimensional case.

A second method allowing the practical application of the one-dimensional 5-moment system is also shown. This technique is based on a surface-fit approximation to the closing flux in a non-dimensionalized parabolic space. It was found that this particular fit conveniently avoids the issues of non-realizability and provides a closed-form expression for the closing flux, therefore numerical calculations can be undertaken in orders of magnitude less time than the previous method. It is shown that solution quality of this surface-fit closure is equally good when compared to solution of the kinetic equation.

Neither of the proposed methods for the generation of practical higher-order moment systems can be obviously extended to the three-dimensional case. The accurate numerical

integration of distribution functions required for the first method would be prohibitively expensive in multiple dimensions. An extension to the surface-fit technique would require that a suitable mapping of the moment quantities could be found, after which the closing fluxes would have to be well approximated by simple expressions. This mapping is not obvious in general. The main idea that should be taken from this study into higher-order moment systems is that there do exist higher-order moment closures and techniques that can be used to obtain accurate solutions to highly non-equilibrium flow problems. Other higher-order moment closures that appear to offer a hyperbolic treatment for viscous, heat-conducting flows have been recently proposed [32], but the work is still preliminary. Further study is required in order to determine which moment equations will prove most fruitful.

8.1 Suggestions and Future Work

This study has clearly demonstrated the general applicability of the 10-moment model to viscous gas-flow prediction. Some mathematical advantages of moment closures, such as their reduced sensitivity to grid quality, has also been shown. However, there remain other issues to investigate. One obvious question is how the numerical solution of moment equations compares to the solution of the Navier-Stokes equations when fully implicit time marching schemes are used. The larger size of the solution vector for the moment-closure case will lead to a larger matrix on the left-hand side, however the first-order nature of the moment equations will afford higher sparsity. It would be interesting to explore which situation can be solved more efficiently.

The development of robust moment methods which allow for a hyperbolic treatment of non-equilibrium heat transfer for three-dimensional gases is also an open problem. The moment technique presented above that is based on a curve fit for the closing flux seems to be the a good starting point for future exploration as this is the only method that could remain affordable in multiple dimensions. For such a technique to work in three dimensions a suitable mapping of the maximum-entropy fluxes would have to be found that would allow them to be fit by similar simple functions. This mapping may not be obvious, however if it could be found, a useful set of hyperbolic moment equations for the prediction of viscous heat-conducting gases in and out of local equilibrium could be the result.

From this study, it would seem obvious that moment-closure techniques offer many

advantages over traditional methods. They offer the promise of partial differential equations that are accurate in a larger range of flow regimes than traditional equations and can often be numerically solved more quickly than particle-based methods. The first-order, hyperbolic, conservation-type equations resulting from moment closures are immediately solvable using the highly sophisticated numerical techniques which have been developed for the numerical solution of hyperbolic conservation laws. Even though moment methods have been studied for some time, this remains a very young field of research that is wide open for the exploration of many ideas. The path this field will take over the next years is entirely uncertain, however the promises offered should make the exploration more than worth the effort.

Erda: *Höre! Höre! Höre!*
Alles was ist, endet!

Richard Wagner – *Der Ring Des Nibelungen*

References

[1] O'Connor, L. Mems: Mircoelectromechanical systems. *Mechanical Engineering Journal*, 114(2):40–47, 1992.

[2] Meyyappan, M., editor. *Computational Modeling in Semiconductor Processing.* Artech House, Boston, 1995.

[3] Bird, G. A. *Molecular Gas Dynamics and the Direct Simulation of Gas Flows.* Clarendon Press, Oxford, 1994.

[4] Mieussens, L. Discrete velocity model and implicit scheme for the BGK equation of rarefied gas dynamics. *Mathematical Models and Methods in Applied Sciences*, 10(8):1121–1149, 2000.

[5] Fan, J. and Shen, C. Statistical simulation of low-speed rarefied gas flow. *Journal of Computational Physics*, 167:393–412, 2001.

[6] Sun, Q. and Boyd, I. D. A direct simulation method for subsonic, mircoscale gas flow. *Journal of Computational Physics*, 179:400–425, 2002.

[7] Grad, H. On the kinetic theory of rarefied gases. *Communications on Pure and Applied Mathematics*, 2:331–407, 1949.

[8] Levermore, C. D. Moment closure hierarchies for kinetic theories. *Journal of Statistical Physics*, 83:1021–1065, 1996.

[9] Müller, I. and Ruggeri, T. *Rational Extended Thermodynamics.* Springer-Verlag, New York, 1998.

[10] Struchtrup, H. *Macroscopic Transport Equations for Rarefied Gas Flows.* Springer-Verlag, Berlin, 2005.

[11] BROWN, S. L.; ROE, P. L.; and GROTH, C. P. T. Numerical solution of a 10-moment model for nonequilibrium gasdynamics. Paper 95-1677, AIAA, June 1995.

[12] BROWN, S. L. *Approximate Riemann Solvers for Moment Models of Dilute Gases*. Ph.D. thesis, University of Michigan, 1996.

[13] GODUNOV, S. K. Finite-difference method for numerical computations of discontinuous solutions of the equations of fluid dynamics. *Matematicheskii Sbornik*, 47:271–306, 1959.

[14] MCDONALD, J. G. and GROTH, C. P. T. Numerical modeling of micron-scale flows using the Gaussian moment closure. Paper 2005-5035, AIAA, June 2005.

[15] SACHDEV, J. S.; GROTH, C. P. T.; and GOTTLIEB, J. J. Parallel AMR scheme for turbulent multi-phase rocket motor core flows. Paper 2005-5334, AIAA, June 2005.

[16] SACHDEV, J. S. and GROTH, C. P. T. A mesh adjustment scheme for embedded boundaries. *Communications in Computational Physics*, 2(6):1095–1124, 2007.

[17] SACHDEV, J. S. *Parallel Solution-Adaptive Method for Predicting Solid Propellant Rocket Motor Core Flows*. Ph.D. thesis, University of Toronto, April 2007.

[18] MCDONALD, J. G.; SACHDEV, J. S.; and GROTH, C. P. T. Gaussian moment closure for the modelling of continuum and micron-scale flows with moving boundaries. In H. Deconinck and E. Dick, editors, *Proceedings of the Fourth International Conference on Computational Fluid Dynamics, ICCFD4, Ghent, Belgium, July 10–14, 2006*, pages 783–788. Springer-Verlag, Heidelberg, 2009.

[19] GOMBOSI, T. I. *Gaskinetic Theory*. Cambridge University Press, Cambridge, 1994.

[20] BURGERS, J. M. *Flow Equations for Composite Gases*. Academic Press, New York, 1969.

[21] STRUCHTRUP, H. and TORRILHON, M. Regularization of grad's 13 moment equations: Derivation and linear analysis. *Physics of Fluids*, 15:2668–2680, 2003.

[22] STRUCHTRUP, H. and TORRILHON, M. H theorem, regularization, and boundary conditions for the linearized 13 moment equations. *Physical Review Letters*, 99:014502, 2007.

[23] Torrilhon, M. and Struchtrup, H. Boundary conditions for regularized 13 moment equations for micro-channel-flows. *Journal of Computational Physics*, 227:1982–2011, 2008.

[24] Coirier, W. J. *An Adaptively-Refined, Cartesian, Cell-Based Scheme for the Euler and Navier-Stokes Equations*. Ph.D. thesis, University of Michigan, 1994.

[25] Coirier, W. J. and Powell, K. G. Solution-adaptive Cartesian cell approach for viscous and inviscid flows. *AIAA Journal*, 34(5):938–945, May 1996.

[26] McDonald, J. G. *Numerical Modeling of Micron-Scale Flows Using the Gaussian Moment Closure*. Master's thesis, University of Toronto, 2005.

[27] Barth, T. J. On discontinuous galerkin approximations of boltzmann moment systems with levermore closure. *Computer Methods in Applied Mechanics and Engineering*, 195:3311–3330, 2006.

[28] Junk, M. Domain of definition of Levermore's five-moment system. *Journal of Statistical Physics*, 93(5/6):1143–1167, 1998.

[29] Junk, M. Maximum entropy moment systems and Galilean invariance. *Continuum Mechanics and Thermodynamics*, 14:563–576, 2002.

[30] Schneider, J. Entropic approximation in kinetic theory. *Mathematical Modelling and Numerical Analysis*, 38(3):541–561, 2004.

[31] Hauck, C. D.; Levermore, C. D.; and Tits, A. L. Convex duality and entropy-based moment closures: Characterizing degenerate densities. *SIAM Journal on Control and Optimization*, 47(4):1977–2015, 2008.

[32] Torrilhon, M. Hyperbolic moment equations in kinetic gas theory based on multi-variate Pearson-iv-distributions. *Communications in Computational Physics*, 7(4):639–673, April 2010.

[33] Schunk, R. W. Transport equations for aeronomy. *Planetary and Space Science*, 23:437–485, 1975.

[34] Schunk, R. W. Mathematical structure of transport equations for multispecies flows. *Reviews of Geophysics and Space Physics*, 15(4):429–445, 1977.

[35] BARAKAT, A. R. and SCHUNK, R. W. Transport equations for multicomponent anisotropic space plasmas: A review. *Plasma Physics*, 24:389–418, 1982.

[36] BHATNAGAR, P. L.; GROSS, E. P.; and KROOK, M. A model for collision processes in gases. i. small amplitude processes in charged and neutral one-component systems. *Physical Review*, 94(3):511–525, 1954.

[37] BOLTZMANN, L. Weitere studien über das wärmegleichgewicht unter gasmolekülen. *Sitz. Math.-Naturwiss. Cl. Akad. Wiss. Wien*, 66:275–370, 1872.

[38] MÜLLER, I. *Thermodynamics*. Pitman Publishing, Boston, 1985.

[39] TALLEC, P. L. and PERLAT, J. P. Numerical analysis of Levermore's moment system. Technical Report 3124, INRIA Rocquencourt, 1997.

[40] DREYER, W. Maximization of the entropy in non-equilibrium. *Journal of Physics A: Mathematical and General*, 1987.

[41] GODUNOV, S. K. An interesting class of quasilinear systems. *Soviet Mathematics Doklady*, 2:947–949, 1961.

[42] FRIEDRICHS, K. O. and LAX, P. D. Systems of conservation laws with a convex extension. *ProcNAS*, 68:1686–1688, 1971.

[43] MAXWELL, J. C. On the dynamical theory of gases. *Philosophical Transactions of the Royal Society of London*, 157:49–88, 1867.

[44] HERTWECK, F. Allgemeine 13-momenten-näherung zur Fokker-Planck-gleichung eines plasmas. *Zeitschrift für Naturforschung*, 20a:1243–1255, 1965.

[45] ORAEVSKII, V.; CHODURA, R.; and FENEBERG, W. Hydrodynamic equations for plasmas in strong magnetic fields — i collisionless approximation. *Plasma Physics*, 10:819–828, 1968.

[46] HOLWAY, L. H. *Approximation Procedures for Kinetic Theory*. Ph.D. thesis, Harvard University, 1963.

[47] HOLWAY, L. H. Kinetic theory of shock structure using an ellipsoidal distribution function. In J. H. de Leeuw, editor, *Rarefied Gas Dynamics*, volume I, pages 193–215. Academic Press, New York, 1966.

[48] Holway, L. H. New statistical models for kinetic theory: Methods of construction. *Physics of Fluids*, 9(9):1658–1673, 1966.

[49] Holway, L. H. The effect of collisional models upon shock wave structure. In C. L. Brundin, editor, *Rarefied Gas Dynamics*, volume I, pages 759–784. Academic Press, New York, 1967.

[50] Hittinger, J. A. *Foundations for the Generalization of the Godunov Method to Hyperbolic Systems with Stiff Relaxation Source Terms*. Ph.D. thesis, University of Michigan, 2000.

[51] Harten, A. High resolution schemes for hyperbolic conservation laws. *Journal of Computational Physics*, 49:357–393, 1983.

[52] Einfeldt, B. On Godunov-type methods for gas dynamics. *SIAM Journal on Numerical Analysis*, 25:294–318, 1988.

[53] Roe, P. L. Approximate Riemann solvers, parameter vectors, and difference schemes. *Journal of Computational Physics*, 43:357–372, 1981.

[54] Khieu, L.; van Leer, B.; and Suzuki, Y. An analysis of a space-time discontinous-Galerkin method for moment equations and its solid-boundary treatment. Paper 2009–3874, AIAA, June 2009.

[55] Barth, T. J. Recent developments in high order k-exact reconstruction on unstructured meshes. Paper 93-0668, AIAA, January 1993.

[56] Venkatakrishnan, V. On the accuracy of limiters and convergence to steady state solutions. Paper 93-0880, AIAA, January 1993.

[57] Sachdev, J. S.; Groth, C. P. T.; and Gottlieb, J. J. A parallel solution-adaptive scheme for predicting multi-phase core flows in solid propellant rocket motors. *International Journal of Computational Fluid Dynamics*, 19(2):157–175, 2005.

[58] Berger, M. J. and Colella, P. Local adaptive mesh refinement for shock hydrodynamics. *Journal of Computational Physics*, 82:67–84, 1989.

[59] Berger, M. J. and Saltzman, J. S. AMR on the CM-2. *Applied Numerical Mathematics*, 14:239–253, 1994.

[60] AFTOSMIS, M. J.; BERGER, M. J.; and MELTON, J. E. Robust and efficient Cartesian mesh generation for component-based geometry. *AIAA Journal*, 36(6):952–960, 1998.

[61] QUIRK, J. J. *An Adaptive Grid Algorithm for Computational Shock Hydrodynamics*. Ph.D. thesis, Cranfield Institute of Technology, January 1991.

[62] QUIRK, J. J. and HANEBUTTE, U. R. A parallel adaptive mesh refinement algorithm. Report 93-63, ICASE, August 1993.

[63] DE ZEEUW, D. and POWELL, K. G. An adaptively refined Cartesian mesh solver for the Euler equations. *Journal of Computational Physics*, 104:56–68, 1993.

[64] GROTH, C. P. T.; DE ZEEUW, D. L.; POWELL, K. G.; GOMBOSI, T. I.; and STOUT, Q. F. A parallel solution-adaptive scheme for ideal magnetohydrodynamics. Paper 99-3273, AIAA, June 1999.

[65] DAVIS, R. L. and DANNENHOFFER, J. F. Decomposition and parallelization strategies for adaptive grid-embedding techniques. *International Journal of Computational Fluid Dynamics*, 1:79–93, 1993.

[66] SUN, M. and TAKAYAMA, K. Conservative smoothing on an adaptive quadrilateral grid. *Journal of Computational Physics*, 150:143–180, 1999.

[67] AFTOSMIS, M. J.; BERGER, M. J.; and MURMAN, S. M. Applications of space-filling curves to Cartesian methods for CFD. Paper 2004-1232, AIAA, January 2004.

[68] VINCENTI, W. G. and KRUGER, C. H. *Introduction to Physical Gas Dynamics*. R. E. Krieger Publishing, Huntington, NY, 1975.

[69] SCHLICHTING, H. *Boundary-Layer Theory*. McGraw-Hill, Toronto, 7th edition, 1979.

[70] SUN, Q. and BOYD, I. D. Drag on a flat plate in low-Reynolds-number gas flows. *AIAA Journal*, 42:1066–1072, 2004.

[71] COUSTEIX, J. and MAUSS, J. *Asymptotic Analysis and Boundary Layers*. Springer-Verlag, Berlin, 2007.

[72] Sobey, I. J. *Introduction to Interactive Boundary Layer Theory.* Oxford Applied and Engineering Mathematics. Oxford University Press, Oxford, 2000.

[73] Levermore, C. D. and Morokoff, W. J. The gaussian moment closure for gas dynamics. *SIAM Journal on Applied Mathematics*, 59(1):72–96, 1998.

[74] Coudeville, H.; Trepaud, P.; and Brun, E. Drag measurements in slip and transition flow. In *Proceedings of the Fourth International Symposium on Rarefied Gas Dynamics*. Academic Press, New York, 1965.

[75] Patterson, G. N. *Introduction to the Kinetic Theory of Gas Flows.* University of Toronto Press, Toronto, 1971.

[76] Allegre, J.; Raffin, M.; and Lengrand, J. C. Experimental flowfields around NACA0012 airfoils located in subsonic and supersonic rarefied air streams. In M. O. Bristeau; R. Glowinski; J. Periaux; and H. Viviand, editors, *Numerical Simulation of Compressible Navier-Stokes Flows*, volume 18 of *Notes on Numerical Fluid Dynamics*, pages 59–68. Fried. Vieweg and Sohn, Braunschweig, Germany, 1987.

[77] Suzuki, Y. and van Leer, B. Application of the 10-moment model to MEMS flows. Paper 2005-1398, AIAA, January 2005.

[78] Thomas, P. D. and Lombard, C. K. Geometric conservation laws and its application to flow computations on moving grids. *AIAA Journal*, 17(10):1030–1037, October 1979.

[79] Bayyuk, S. A.; Powell, K. G.; and van Leer, B. A simulation technique for 2-D unsteady inviscid flows around arbitrarily moving and deforming bodies of arbitrary geometry. Paper 93–3391, AIAA, January 1993.

[80] Murman, S. M.; Aftosmis, M. J.; and Berger, M. J. Implicit algorithms for moving boundaries in a 3-D cartesian method. Paper 03–1119, AIAA, January 2003.

[81] Osher, S. and Fedkiw, R. *Level Set Methods and Dynamic Implicit Surfaces*, volume 153 of *Applied Mathematical Sciences.* Springer, 2003.

[82] Sethian, J. A. *Level Set Methods and Fast Marching Methods.* Cambridge Monographs on Applied and Computational Mathematics. Cambridge University Press, 2nd edition, 1999.

[83] LANDON, R. H. Compendium of unsteady aerodynamic measurements. Advisory Report 702, NATO AGARD, August 1982.

[84] ANDRIES, P. and PERTHAME, B. The ES-BGK model equation with correct prandtl number. In T. J. Bartel and M. A. Gallis, editors, *Rarefied Gas Dynamics*, volume I, pages 30–36. American Institute of Physics, New York, 2001.

[85] KENNARD, E. H. *Kinetic Theory of Gases*. McGraw-Hill, New York, 1938.

[86] BARTH, T. J. Numerical methods for gasdynamic systems on unstructured meshes. In Kröner; M. Ohlberger; and C. Rohde, editors, *An Introduction to Recent Developments in Theory and Numerics for Conservation Laws: Proceedings of the International School*, volume 5. Springer-Verlag, Berlin, Freiburg, Germany, 1999.

[87] FELDMANN, S. and HEINIG, G. Vandermonde factorization and canonical representations of block Hankel matrices. *Linear Algebra and its Applications*, 241-243:247 – 278, 1996. ISSN 0024-3795. doi:DOI:10.1016/0024-3795(95)00501-3. Proceedings of the Fourth Conference of the International Linear Algebra Society.

[88] BOLEY, D.; LUK, F.; and VANDEVOORDE, D. Vandermonde factorization of a Hankel matrix. Paper, Workshop on Scientific Computing 97, Hong Kong, 1997.

[89] O'TOOLE, A. L. A method of determining the constants in the bimodal fourth degree exponential function. *Annals of Mathematical Statistics*, 4(2):79–93, May 1933.

[90] O'TOOLE, A. L. On the system of curves for which the method of moments is the best method of fitting. *Annals of Mathematical Statistics*, 4(1):1–29, February 1933.

[91] AROIAN, L. A. The fourth degree exponential distribution function. *Annals of Mathematical Statistics*, 19(4):589–592, December 1948.

[92] MATZ, A. W. Maximum likelihood parameter estimation for the quartic exponential distribution. *Technometrics*, 20(4):475–484, November 1978.

[93] HAMBURGER, H. L. Hermitian transformations of deficiency-index $(1, 1)$, Jacobian matrices, and undetermined moment problems. *American Journal of Mathematics*, 66:489–552, 1944.

[94] Reed, M. and Simon, B. *Methods of Modern Mathematical Physics, II: Fourier Analysis, Self-Adjointness*. Academic Press, New York, 1975.

[95] Au, J. D. *Lösung Nichtlinearer Problems in der Erweiterten Thermodynamik*. Ph.D. thesis, Technische Universität Berlin, 2001.

[96] Junk, M. Minimum relative entropy systems of the Boltzmann equation. Unpublished work.

[97] Harten, A.; Lax, P. D.; and van Leer, B. On upstream differencing and Godunov-type schemes for hyperbolic conservation laws. *SIAM Review*, 25(1):35–61, 1983.